

Damage and fracture
of ductile metals
under dynamic loading conditions

Steffen Gerke

Dissertation

Kontakt:

Steffen Gerke

steffen.gerke@unibw.de; steffen.gerke@tu-dortmund.de

Institut für Mechanik und Statik

Universität der Bundeswehr München

Werner-Heisenberg-Weg 39

85579 Neubiberg

www.unibw.de/baumechanik

Damage and fracture
of ductile metals
under dynamic loading conditions

Steffen Gerke

Vollständiger Abdruck der von der Fakultät für Bauingenieurwesen und Umweltwissenschaften der Universität der Bundeswehr München zur Erlangung des akademischen Grades eines

Doktor-Ingenieurs (Dr.-Ing.)

genehmigte Dissertation.

Gutachter:

1. Prof. Dr.-Ing. habil. Michael Brüinig
2. Prof. Dr.-Ing. habil. Dr. h. c. Holm Altenbach,
Otto-von-Guericke-Universität, Magdeburg

Die Dissertation wurde am 12. März 2013 bei der Universität der Bundeswehr München eingereicht und durch die Fakultät für Bauingenieurwesen und Umweltwissenschaften am 13. März 2013 angenommen. Die mündliche Prüfung fand am 14. Mai 2013 statt.

Kurzfassung

In dieser Arbeit wird das dynamische Verformungsverhalten duktiler Metalle, welches durch großes Verformungsvermögen vor dem Versagen gekennzeichnet ist, untersucht. In einem bestimmten Bereich sind die auftretenden Verzerrungen umkehrbar oder elastisch wobei bei Erreichen einer bestimmten Grenze zusätzliche größere bleibende oder plastische Verzerrungen auftreten. Bei weiterer Belastung beginnt ab einem Punkt, an dem schon größere plastische Verzerrungen vorliegen, eine Entfestigung des Materials, d.h. ein Schädigungsprozess, welcher schließlich zur Bildung eines Makrorisses führt. Das Verformungsverhalten des Materials ist hierbei abhängig vom Spannungszustand, von der Verzerrungsrate sowie von der vorliegenden Temperatur. Der besondere Fokus dieser Arbeit liegt auf der Modellierung und numerischen Simulation des Schädigungs- und Rissverhaltens duktiler Metalle.

Um das Materialverhalten in einer konsistenten Form beschreiben zu können, wird ein phänomenologisches Kontinuumschädigungs- und Rissmodell vorgestellt. Diese theoretischen Überlegungen werden als benutzerdefiniertes Materialmodell an das kommerzielle Finite-Element-Programm LsDyna angebunden, wodurch das entwickelte Modell für Simulationen zugänglich wird. Um das Materialverhalten unter kontrollierten Bedingungen untersuchen zu können, wurden verschiedene Experimente durchgeführt. Diese experimentellen Ergebnisse sowie aus der Literatur entnommene Daten wurden verwendet, um die zugehörigen Materialparameter des Schädigungs- und Rissmodells für eine Aluminiumlegierung sowie für den Edelstahl Inox 304L zu bestimmen.

Die zugehörigen numerischen Simulationen mit dem implementierten Kontinuumschädigungs- und Rissmodell zeigen gute Übereinstimmung mit den experimentellen Ergebnissen. Hierbei wurde besondere Aufmerksamkeit auf die Simulation von Versuchen in der Split-Hopkinson-Bar mit M-förmigen Probekörpern gelegt. Durch die erhaltenen numerischen Ergebnisse konnte das Verhalten dieses speziellen Versuchskörpers besser untersucht werden, was schließlich zu einer kritischen Beurteilung der Geometrie geführt hat. Zusätzlich wurden Scherver Versuchskörper numerisch untersucht und bewertet. Hierbei konnte aufgezeigt werden, dass eine zusätzliche Kerbe in Dickenrichtung das gewünschte Verhalten des Versuchskörpers signifikant verbessert.

In diesem Zusammenhang ist deutlich geworden, dass weitere experimentelle Untersuchungen mit Versuchskörpern, bei denen Schädigungs- und Rissverhalten unter verschiedenen Spannungszuständen auftritt, sinnvoll sind. Ebenfalls konnte aufgezeigt werden, dass numerische Untersuchungen zur inversen Bestimmung der Materialparameter im Schädigungs- und Rissbereich notwendig sind, da hier nur unzureichende experimentelle Ergebnisse vorliegen.

Die Ergebnisse dieser Arbeit erlauben ein wesentlich besseres Verständnis des Verformungs- und Versagensverhaltens von duktilen Metallen. Diese Erkenntnisse können bei verschiedenen Anwendungen, z.B. beim Entwurf von Leichtbaustrukturen sowie bei der Simulation von Aufprallversuchen in der Automobilindustrie und bei Hochgeschwindigkeitsproduktionsprozessen, verwendet werden. Dies führt zu einer höheren Auslastung des Materials und somit zu Ressourcen- und Kosteneinsparungen.

Abstract

This thesis covers the deformation behavior of ductile metals which is characterized through large strains before final failure occurs. Within a certain range, these strains are reversible or elastic, whereas onward additional major non-reversible or plastic strains occur. At a certain point, at which already significant plastic strains have been accumulated, additional deterioration of the material, i.e. a damage process, starts, resulting in a macro-crack that finally leads to the failure of the material. The deformation process usually depends on the stress state, the strain rate and the temperature of the material. In this work, special focus is given to the damage and failure process.

In order to describe the material behavior in a consistent way, a phenomenological continuum damage and fracture model has been developed. To make the model available for numerical simulations, the commercial finite element program LsDyna has been augmented by a user-defined material model subroutine. To determine the material behavior under controlled conditions, several experiments have been performed. The experimental results, as well as data from literature, have been used to identify the material parameters for the proposed continuum damage and fracture model for an aluminum alloy and for the stainless steel Inco 304L.

The executed numerical simulations with the implemented continuum damage and fracture model show a good correlation with the experimental data. Special focus has been given to the simulation of Split-Hopkinson-Bar experiments with M-Shape tension specimens. With these numerical studies, several aspects of the special specimen geometry could be extracted and analyzed, resulting in a critical evaluation of the specimen shape. In addition, shear specimens have been numerically studied and evaluated, while an additional notch in thickness direction has been introduced which results in the required behavior and therefore could be very useful for future research.

In this context, it became evident that further research should include additional experiments testing damage occurrence and evolution at different stress states. Furthermore, there is need for inverse numerical procedures in order to identify the parameters of the damage condition, damage law and fracture condition.

The results of this thesis improve significantly the understanding of the deformation and fracture behavior of ductile metals. These insights can be used in several applications such as the design of light weight structures and the simulation of car crashes or high speed machining processes, allowing a maximum utilization of the material, resulting in a more responsible and cost-efficient handling of resources.

Preface

This thesis was generated during work as scientific assistant at the Technische Universität Dortmund and at the Universität der Bundeswehr München.

First of all I would like to express my sincere thanks to Prof. Michael Brüning who inspired this work and who was always available for discussions. Besides the topic of this thesis he provided the access to many related subjects not least though the possibility to attend various scientific conferences. Furthermore he facilitated my relocation to Munich where I could support the built-up of the professorship under his guidance, including different lectures and tutorials. Here he always provided an excellent working atmosphere.

Furthermore I would like to thank Prof. Holm Altenbach to accept the review of this thesis as well as for the helpful discussions and Prof. Thomas Apel for accepting the chairmanship of the examining board.

At this point it is more than worthy of mention that all my colleagues at the Universität der Bundeswehr München as well as at the Technische Universität Dortmund always provided a good working atmosphere and supported my scientific advancement by many helpful discussions.

In addition I would like to thank the workgroups of Prof. Larissa Driemeier and Prof. Marcilio Alves at the University of São Paulo, Brazil (USP) where I could accompany the experimental work.

Furthermore it is worthy to mention that I had the possibility to accompany several student assistants during their first scientific steps: Sindern, Robin Czerny and Kevin Kuhnt.

Special thanks go to Katrin Schnettler Ruetz for proofreading this thesis.

Steffen Gerke
Munich, May 2013

Contents

1	Motivation	1
1.1	Ductile damage and fracture	1
1.2	Strain rate and temperature dependence	4
1.3	Scientific background	5
1.4	Scope and classification of this work	12
2	Continuum damage and fracture model	13
2.1	Kinematics	13
2.2	Thermodynamics	19
2.3	Constitutive equations	24
2.4	Numerical integration of constitutive rate equations	32
3	Numerical procedure	43
3.1	Finite Element procedure	43
3.2	Explicit time integration	46
3.3	LsDyna user materials	48
4	Experimental aspects	50
4.1	Strain rate	50
4.2	Temperature	55
4.3	Stress state	56
5	Identification of material parameters	59
6	Numerical examples	67
6.1	Finite element modeling	67
6.2	Reduced M-Shape	71
6.3	Split-Hopkinson-Bar tests: Rings	76
6.4	Split-Hopkinson-Bar tests: M-Shape	77
6.5	Split-Hopkinson-Bar tests: Shear specimen	89
7	Closure	100
7.1	Summary and conclusions	100
7.2	Perspective	102
	Bibliography	104

1 Motivation

The performance of structures and materials is expected to resist to higher loading and on the other hand the responsible handling of resources becomes more important. Thus a high utilization is necessary which requires a good knowledge of the elastic-plastic material characteristics and also of its damage and fracture behavior. Consequently the need of material models which can describe such complex material behavior is evident. Areas of application could be the design of light weight structures, the simulation of car crashes or high speed machining and penetration processes in operator protection.

The failure of structures is frequently caused by local material failure. Previous to this complete failure the material did undergo the progressive physical process of ongoing damage. Often this process takes place under elevated temperature or it develops with high velocity for instance at impact or collision processes. To be able to predict this damage and failure of materials it is necessary to describe the material behavior in such a way that it can be used in numerical simulations.

The form in which damage occurs depends on several parameters, among other the nature of the material, the type of loading and the temperature [100]. For example creep damage occurs at higher temperatures where the strains increase at almost constant stresses, brittle damage is characterized by very low plastic strains before the occurrence of deterioration of the material and fatigue damage appears under cyclic loading of the material, see [77, 42, 100] for a more detailed description. Furthermore ductile damage is characterized by the appearance of large plastic strains before the deterioration propagates, see Fig. 1.1. This thesis focusses on ductile damage and the resulting fracture.

In this thesis a phenomenological model to characterize the elastic and inelastic behavior of ductile metals under elevated temperatures and high strain rates is presented. Furthermore the material model was coded and implemented into a commercial software and consequently used for the numerical simulations of executed experiments.

1.1 Ductile damage and fracture

Before having a closer look at ductile damage in metals it is worthwhile to investigate briefly the physical nature of elastic, plastic and damage ma-

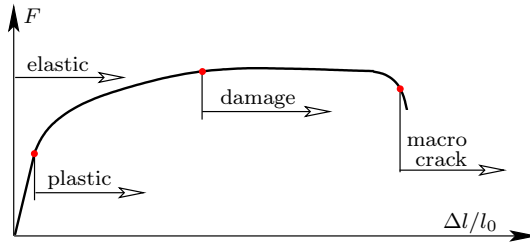


Figure 1.1: Typical experimental curve of ductile damage, indicating that the material behavior first is elastic, then elastic-plastic and in continuation elastic-plastic-damaged before finally macro cracks occur, here taken from an experiment with shear-like failure

terial behavior. Since the implemented continuum damage and fracture model is phenomenologically based, the main aspects are of interest. The reversible, i.e. the elastic material behavior, is directly related to the relative movement of atoms whereas plastic material behavior has its origin at slips on the crystal level. Due to this fact, it can be assumed that the elastic and the plastic material behavior can be reviewed independently. Damage material behavior is based on the debonding of grains and consequently it influences directly the elastic material but does not remarkably effect the plastic material characteristics. This brief introduction is based on [100] where a more detailed description can be found.

Fig. 1.1 displays a typical load-displacement curve of an experiment including ductile damage. Previous to damage evolution major plastic deformations occur. Fig. 1.2_a shows the initial distribution of pores in highly pure iron [12]. In metals with impurity particles these impurities can cause similar effects as a pore matrix [51, 15]. With ongoing deformation under a certain stress state the pores enlarge, new voids form (nucleation) and finally the coalescence of pores occurs whereas under a more shear-like stress state rather micro shear cracks appear to be a governing damage mechanism. Fig. 1.2_b illustrates such a pore pattern where big void coalescence took place mainly perpendicular to the loading direction. This state might be seen as the initiation of a macro crack. Further representations, including 3-dimensional views, can be found for instance in Maire et al. [112, 113], Landron et al. [91] and Toda et al. [157].

The transition from damage to macro crack is not easy to define; Chaboche mentioned values of approximately 1 mm of void diameter [41]. But

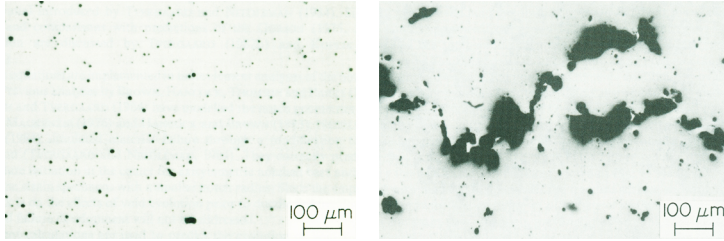


Figure 1.2: Initial distribution of pores with 1% porosity (left side) and failure pattern of a initially fully dense notched bar (right side), tensile loading in vertical direction, cut-outs taken from Becker et al. [12]

whereas the damage process evolves over a certain period, the macro crack propagates fast almost instantaneously. Fig. 1.3 illustrates an ongoing crack in ductile metal which was generated under controlled conditions. In Figs. 1.2_b and 1.3 one can notice, that the porosity around the forming crack increases but stays rather homogenous.

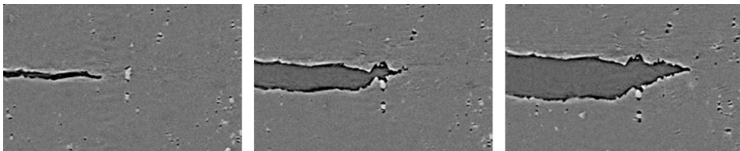


Figure 1.3: Virtual tomographic slices of growing crack-tip during tension test, cut-outs taken from Toda et al. [156]

Fig. 1.4 displays two examples of fracture surfaces, at the left a circular notched steel specimen and at the right a flat notched Inox 304L specimen. Both show a similar failure pattern, in the center resulting from typical void growth with dimples and on the surrounding a shear-like fracture.

Damage measurement is not an easy task. Several methods have been proposed which are either destructive or non-destructive for the specimen. Lemaitre [100] gives an overview and an evaluation of the different methods. As mentioned before damage has direct influence on the elastic behavior of the material and therefore one common possibility to measure ductile damage is the determination of the variation of the Young's modulus. But for the materials under examination in this thesis, due to mainly local occurrence of damage and the available testing facility,

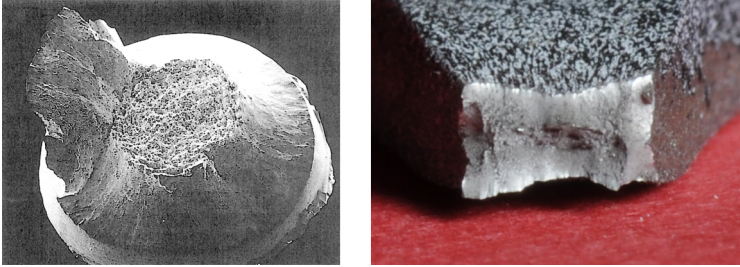


Figure 1.4: Fracture surfaces, left side: cup-and-cone fracture of steel, cut-out taken from 'An Atlas of Metal Damage' [51], right side: Fracture of notched stainless steel specimen

made it difficult to reveal this variation. Thus Brüning et al. [31] proposed the method of performing an elastic-plastic numerical simulation and defining the onset of damage where the experimental and obtained numerical load-engineering strain curves diverge. This method has been successfully used for aluminum alloy in [30].

1.2 Strain rate and temperature dependence

Ductile metals frequently show sensitivity to strain rate, i.e. the velocity at which the strain develops, and temperature. Generally, at higher strain rates the material response is stiffer and at higher temperatures the material response is softer. If these effects are not negligible for the investigated phenomena they have to be analyzed. Furthermore, part of the plastic work is converted to heating and consequently for fast deformation processes the increase of temperature can be significant whereas the discharge of heat can be neglected. Thus this process can be considered as adiabatic.

Fig. 1.5 displays stress-strain curves of a stainless steel taken at a strain rate of 8500 s^{-1} in a Split-Hopkinson-Bar experiment (details on the experimental setup are given later) at different temperatures, [60]. The material response is remarkable softer at the elevated temperatures of 500 K and 1000 K and stiffer at the lower temperature of 77 K whereas the room temperature of 296 K is taken as reference. The unstable behavior of the experimental curves is due to the experimental technique.

An example of the strain rate sensitivity of stainless steel is given in Fig. 1.6, [60]. The curve at low strain rate 0.001 s^{-1} was generated in a hydraulic testing machine in a compression test whereas the curves at

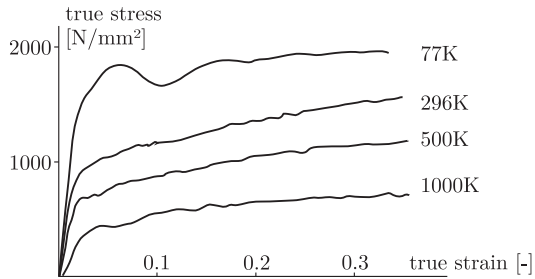


Figure 1.5: Temperature effects in stainless steel Nitronic-50 at a strain rate of 8500 s^{-1} ; graph reproduced from Guo and Nemat-Nasser [60]

higher strain rates have been taken in Split-Hopkinson-Bar experiments. At higher strain rates 3500 and 8000 s^{-1} the first material response is stiffer, but nevertheless the maximum strain is lower than at lower strain rates.

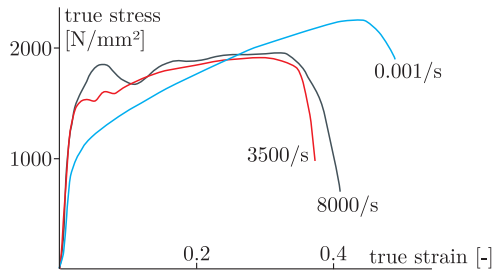


Figure 1.6: Strain rate effects in stainless steel Nitronic-50, graph reproduced from Guo and Nemat-Nasser [60]

1.3 Scientific background

The elastic or reversible deformations of ductile metals can be described by a hyperelastic material law which assumes the existence of an elastic potential function [52, 166, 134, 24]. Frequently the plastic material behavior is described by a yield condition and flow rule which only depend on the deviatoric stress state. In contrast Spitzig et al. [150, 147] have experimentally shown that also the hydrostatic stress state has remark-

able influence on the plastic behavior of ductile metals while Brünig [24] has shown remarkable influence of the hydrostatic stress state on the localization behavior of ductile solids. Due to this fact, within this thesis a Drucker-Prager type of yield condition [50] is used.

Having a closer look at ductile damage and following the review of Garrison and Moody [55], the observation of ductile damage was first reported by Henry [67] in 1855. In this paper, firstly a disquisition is made on the marble for the extension of the United States capitol which is followed by the descriptions of tension experiments with rods of lead. Here he observes:

[...] the interior fibres of a rod of this material may be entirely separated, while the outer surface presents no appearance of change.

Consequently, he describes the ongoing process of ductile damage and fracture. A further early paper containing a description of the phenomena of ductile damage and fracture was published by Ludwik [110] in 1927. This publication already includes a photo of a cross section clearly indicating the growth of micro voids and a macro crack.

The paper of Kachanov [75] published in 1958 can be seen as the starting point of damage mechanics, i.e. the phenomenological description of the damage process. This initial paper was translated from Russian to English and published in the *International Journal of Fracture* [78]. Here he states:

Although we discuss microcracking, the results can be interpreted in a more general way, in terms of development of damage.

Thus he clearly distinguished between microcracking, i.e. the beginning of fracture and ongoing deterioration of the material, i.e. damage. Kachanov [75] introduced damage as a scalar variable and created the idea of effective stress. Furthermore it can be mentioned that Rabotnov [136] modified the notation to which became frequently used today in damage mechanics.

Besides this phenomenological description of damage, a second branch of research developed which is based on micromechanical studies of pores in elastic-plastic material. The first pioneering works have been presented by McClintock [115] in 1968 and by Rice and Tracey [138] in 1969. McClintock [115] considered cylindrical voids with circular and elliptical lateral cut within an elastic-plastic non-hardening material subjected to tension with transverse stress. Here damage is defined by the change of diameter of the voids and a criterion for the coalescence of pores is introduced which is also based on the pore diameter. These first studies

show already a strong dependence of the stress state, namely triaxiality on void growth. Rice and Tracey [138] reviewed models of one spherical void in an elastically rigid, plastically incompressible material without or with linear hardening which were subjected to tensile stress superimposed with hydrostatic stress leading to an approximation for the void growth for different stress states.

Further micromechanical studies of an elastic-plastic material sample under plane strain conditions with periodic cylindrical voids have been realized by Needleman [126] in 1972. Due to the alignment of voids, the material behavior between voids could be reviewed giving a good indication of void interaction and consequently offering a first indication to void coalescence. In addition, Gurson [61] based his micromechanical considerations in 1977 on analytical investigations of a reference volume element with one single void. The material behavior was considered to be elastic-plastic whereas the influence of the void volume fraction as one single parameter was included to the yield criterion reducing the yield stress. Thus this model introduced by Gurson could predict void growth whereas terms for void nucleation and coalescence were added later by Tvergaard and Needleman [158, 161] although those required the introduction of additional material parameters. Due to the fact that damage is directly related to void volume fraction, the Gurson-Tvergaard-Needleman (GTN) model in this form provides acceptable results where void growth and nucleation are the major damage mechanisms, i.e. at high triaxialities. Today the GTN model is available in several commercial computer codes and is used and extended for ongoing investigations, see e.g. [106, 49, 114, 70]

Another frequently used model to predict fracture of ductile metals was introduced by Johnson and Cook [72, 73]. Based on an extensive series of experiments, considering various metals at different strain rates and temperatures, they first introduced a hardening law with a multiplicative decomposition of the strain rate and temperature effects. Especially the strain rate and temperature effects on the plastic material behavior were considered. Later they extended the model by introducing a variable as the sum of the increment of the equivalent plastic strain divided by the equivalent strain to fracture. This variable can be easily updated in each time step and thus leads to a simple numerical model. The equivalent strain to fracture is also multiplicatively decomposed reflecting strain rate and temperature effects. Thus the Johnson and Cook model does not consider damage in a physical sense. It predicts strain rate and temperature dependent behavior of the material and provides a fracture criterion based on accumulated equivalent plastic strains.

Motivated by the need of a phenomenological damage model for the simu-

lation of real structures but reflecting the mechanisms on the micro scale, Lemaitre [98, 99] picked up the ideas of Kachanov [75] and Rabotnov [136] described above and introduced a continuum damage model. He used a scalar damage variable which had direct influence on Young's modulus (see Fig. 1.7) and therefore is related to the concept of effective surface, i.e. damage is a surface related measure. Furthermore, the hypothesis of strain equivalence describes that the strain behavior of the damaged material is represented by that of an undamaged material, only replacing the stress by the effective stress. In continuation several authors, see e.g. [154, 43], picked up Lemaitre's ideas and modified the damage model for different applications, specially Bonora [20] found three different damage evolution trends which he adopted into his damage model. Later Lemaitre [102] extended the aforementioned model from the outlined isotropic damage to anisotropic, i.e. a tensorial, description and special focus on closure effects [48] was given. Furthermore, the damage model has been applied to many practical applications such as bulk metal forming [7] and deep drawing [130].

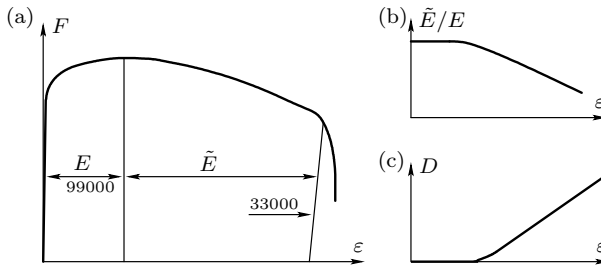


Figure 1.7: (a) Load strain curve of copper with unloading paths, (b) corresponding evolution of Young modulus ratio \tilde{E}/E , (c) corresponding evolution of damage D as described in Lemaitre's damage model, Figs. taken from [103] and [100].

In 1981 Murakami and Ohno [124] presented a model to analyze creep damage where damage is represented by a second order tensor which allows the reflection of anisotropic damage. Here in the kinematics, different configurations are introduced which are fictitiously undamaged or/and elastically unloaded [121]. The different configurations are related to each other by the elastic deformation gradient and different damage tensors. Furthermore, Murakami [121] generalized the ideas of Kachanov [75] and Rabotnov [136] with respect to net-stress to multiaxial states. Later Murakami et al. [123] studied experimentally the evolution of damage in elastic-plastic-damage materials in connection with the existence of a

damage surface.

Besides aforementioned approaches, several further damage models with different focus have been presented. For instance, Kachanov [76] introduced a tensorial quantity, allowing the description of anisotropic effects of damage on the elastic properties which was kinematically motivated by an undamaged and a damaged configuration. Krajcinovic and Fonseka [88, 89] proposed a model for the damage description in brittle materials which was extended to ductile materials by Krajcinovic [84]. Here damage is introduced as an axial vector and is motivated by a dissipation potential, i.e. two dissipative processes, plasticity and damage, are considered. The concept of effective stress is generalized by Chaboche [38, 39] where damage is represented by a non-symmetric fourth-order tensor. In contrast Betten [17, 18] generalizes Rabotnov's damage concept of net-stress to a second-order tensor representation, allowing the representation of anisotropic damage effects. Both Chaboche [39] and Betten [17] first focused on creep damage whereas Chow and Wang [45] concentrated on ductile damage. Chow and Wang [45] also extended the concept of effective stress to a tensorial representation which could represent the anisotropic effects but also proposing a simplified version for isotropic damage. Later Lu and Chow [109] presented an alternative formulation based on the concept of effective strain (hypothesis of stress equivalence) which was introduced by Cordebois and Sidoroff [46] and compared with the concept of effective stress (hypothesis of strain equivalence) by Simo and Ju [144]. Voyiadjis and Kattan [164, 165] extended the effective stress concept to a second order tensor representation of damage with special focus on small elastic strain and remarkably bigger inelastic strain, i.e. ductile damage. The model was applied in conjunction with a GTN-type yield function. Bruhns and Schiesse [36] presented a model for materials with large plastic deformations where damage is kinematically motivated by the introduction of different configurations. Furthermore, the model is characterized by a clear distinction between internal damage variables and variables characterizing the macroscopic damage whereas the failure of the material is characterized by a failure criterion. Steinmann and Carol [152] also introduced damage kinematically using a distinction between undamaged (microscopic) and damaged (macroscopic) configurations forcing strain energy equivalence. The configurations are related to each other by damage deformation gradients with corresponding metrics. The damage model presented by Brünig [25, 26] will be discussed in detail and extended in its temperature and strain rate dependence form [28] within this thesis. Lately Vignjevic et al. [163, 162] proposed a phenomenological damage model to predict the dynamic behavior of orthotropic metals by shock wave induced deforma-

tions. Here also the two dissipative processes of plasticity and damage are characterized by potentials but in contrast a multiplicative decomposition into an elastic, a plastic and a damage part is used.

Thus damage mechanics developed continuously after Kachanov's [75] first paper, whereas several new ideas have been presented at the end of the Seventies and the beginning of the Eighties of the last century. Meanwhile several reviews have been published, for instance Murakami [120] focussed on anisotropic damage in metals from an experimental and mathematical point of view; Krajcinovic [85] first compared and summarized the presented damage models and later focused on brittle damage [86]; Chaboche [40, 41, 42] reviewed the damage definitions and described the connection between damage and fracture; Tvergaard [159] put his main focus on void growth and coalescence, i.e. he described the process when discrete cavities develop firstly into micro cracks and finally into macro cracks whereas the same subject was picked up lately by Benzerga and Leblond [15]. Also several books were published on damage mechanics which give partly emphasis to selected subjects or are general overviews. For instance, Kachanov [77] focused on the mechanical description of damage with special focus on creep in connection with damage whereas Lemaitre [100] described in detail the physical nature of damage and the possibilities of damage measurement. Furthermore, Lemaitre and Desmorat [101] described in their extended publication anisotropic damage models. Krajcinovic [87] first focused on the internal structure of the material and its influence on the material behavior and then described micromechanical motivated models and phenomenological motivated models whereas Altenbach and Skrzypek [4] collected different contributions in connection with creep and damage. Recently Zang and Cai [171] presented an extensive overview on damage mechanics, while Murakami [122] gave a general introduction to damage and then focused on different applications whereas Saanouni [141] wrote about more practical applications in metal forming.

Currently great efforts are made to study the damage mechanisms at different stress states. Therefore specimens with different shapes have been designed to force damage occurrence and final fracture at different stress states. Generally accompanying numerical simulations are performed to estimate the stress state in the specimens' regions of interest. For instance Gao et al. [54] presents an extensive experimental program containing smooth as well as notched round bars, notched metal sheets and torsion specimen to analyze its ductile plastic and fracture behavior whereas Mohr and Henn [119] propose a new testing device and a new butterfly shaped specimen which can be tested at different angles which lead to different triaxialities at the location where cracking occurs.

The initiation of a macro crack is generally described through a fracture criterion. On the one hand, as mentioned before with respect to the Johnson and Cook [72, 73] material model, this fracture criterion does not necessarily depend on a prior damage process and Bao and Wierzbicki [10, 11] studied the influence of stress triaxiality on ductile fracture. On the other hand, the process of ductile damage comprises the process of ongoing deterioration of the material as it can be clearly seen by the change of the elastic material properties prior to fracture and thus the introduction of a damage measure is obviously necessary. And, continuing this idea, the damage measure can be used to define a fracture criterion, for instance the GTN-model depends on a critical void volume fraction, i.e. a measure with specific physical meaning, as fracture criterion, see [161, 159]. This explicit physical meaning is not always given, for instance Xue [170] extended the GTN-model to predict more precisely damage and failure under more shear-like stress conditions introducing a new internal variable for damage detached from the void volume fraction. Furthermore Nahshon and Hutchinson [125] picked up the ideas of Bao and Wierzbicki [10, 11] in order to extend the GTN-model to application with shear-like fracture, also taking into account the Lode parameter.

The subject of strain rate and temperature sensitivity has been widely discussed within the open literature. Focussing on stainless steel which is one of the materials considered in this thesis for examples: Hecker et al. [66] investigated the change of the microstructure at different strain rates in compression tests whereas Semiatin and Holbrook [142, 143] focussed on different strain rates using torsion tests. Furthermore Stout and Follansbee [153] analyzed tension and compression tests over a wide range of strain rates while Ishikawa and Tanimura [71] researched the effects of low temperatures. In the last years Nemat-Nasser and co-workers published several papers, e.g. [129, 128, 60], investigating the behavior of different (stainless) steels with a new technique in Split-Hopkinson-Bar for a wide range of temperatures.

Overall it can be seen that the damage and fracture process of ductile metals is still subject of current research. In this connection the need for experimental data allowing to study the damage and fracture behavior under different stress states, temperatures and elevated strain rates is evident, i.e. the design of new specimen geometries is of interest and the applicability of experimental techniques has to be evaluated. Furthermore, these experimental observations have to be transferred into a continuum damage and fracture model allowing to predict the complete deformation process until final fracture for different stress states, elevated temperatures and strain rates. In this connection a procedure is needed to identify all necessary model parameters. Finally, the continuum dam-

age and fracture model has to be implemented into a simulation software which can be used to predict the damage and failure behavior of components and structures.

1.4 Scope and classification of this work

The need of an efficient, phenomenological continuum damage and fracture model, which can be used for the prediction of damage and failure under different stress states, strain rates and temperatures, is evident for many industrial applications such as car crash simulations, high-speed machining and penetration processes. To fulfill this need, the following objectives are analyzed within this thesis:

- Presenting the continuum damage and fracture model introduced by Brünig [25, 26, 28] in its rate- and temperature-dependent form. In addition, the damage softening behavior is reviewed and a fracture criterion is added to describe the complete deformation process until final fracture occurs.
- Realizing the numerical implementation into the explicit Finite Element code LsDyna via a user-defined subroutine.
- Describing the necessary experiments to analyze the material behavior under different stress states, strain rates and temperatures. Presenting the results of the realized experiments in order to identify the material constants and discussing this process in detail for the stainless steel Inox 304L.
- Investigating the possibility to realize three-dimensional numerical simulations of Split-Hopkinson-Bar experiments and proposing a sufficiently precise model by acceptable numerical costs.
- Demonstrating the applicability of the coded model by realizing simulations of executed Split-Hopkinson-Bar experiments and comparing the numerical results with the experimental data.
- Evaluating the geometry of the so-called M-Shape specimen with respect to suitability for the extraction of material curves. Studying the geometry of a specimen with shear like failure and propose modifications.

This thesis is structured as follows: In Chap. 2 the continuum damage and fracture model is introduced while Chap. 3 illustrates the numerical implementation. In continuation, an experimental overview is given in Chap. 4 whereas in Chap. 5 the procedure to identify the material parameters is presented in detail for the stainless steel Inox 304L. Several numerical examples are given in Chap. 6 mainly concerning Split-Hopkinson-Bar experiments. Finally, Chap. 7 summarizes the main issues and extracted conclusions of this thesis and offers a perspective for future works.

2 Continuum damage and fracture model

2.1 Kinematics

The macroscopic phenomenological framework was presented by Brüning in [25, 26] for the description of large elastic-plastic-damage deformations of metals, including anisotropic damage and goes back for isotropic considerations to Lehmann [96, 97]. A representation of the kinematics is given in Fig. 2.1. The main ideas of this kinematic framework can be outlined as follows:

- Introduction of a damaged set and a fictitious undamaged set of configurations,
- Use of the metric transformation tensor \mathbf{Q} which is a mixed variant representation of the left Cauchy-Green-Tensor \mathbf{B} ,
- In both sets of configurations a fictitious stress free placement is taken into account,
- Damage tensors \mathbf{R} , $\overset{\circ}{\mathbf{R}}$, $\overset{*}{\mathbf{R}}$ relate the damaged and fictitious undamaged configurations to each other.

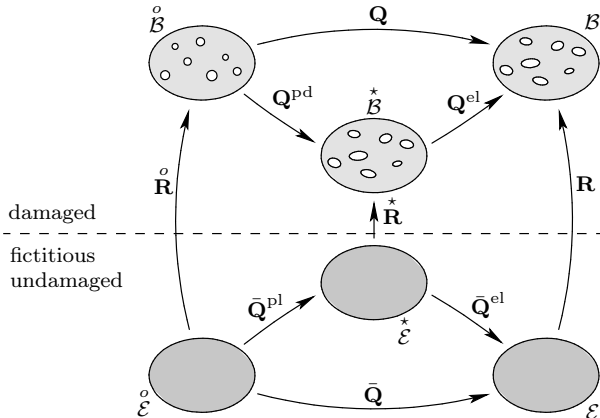


Figure 2.1: Configurations and metric transformation tensors

At this point it is important to notice that the used kinematic decomposition of the physical processes is different to the multiplicative decomposition of the deformation gradient into an elastic and an plastic part as proposed by Lee [92] and frequently used, see for instance [121, 169, 165]. As Lehmann [94] points out, Lee's approach leads to rotations on the intermediate configuration which need to be treated in a suitable way to obtain reasonable strain measures while the presented kinematics avoid this problem directly.

For further considerations all quantities are referred to the current placement \mathcal{B} . Furthermore it is assumed that the body can be considered as a classical continuum, although it shows micro defects, see [96, 137].

2.1.1 Damaged configurations

The base vectors $\overset{\circ}{\mathbf{g}}_i$ are related to the initial undeformed configuration $\overset{\circ}{\mathcal{B}}$ which might have an initial damage. Furthermore, the base vectors \mathbf{g}_i correspond to the elastically and plastically deformed as well as damaged configuration \mathcal{B} . By fictitiously removing the elastic deformations, the stress-free configuration $\overset{\star}{\mathcal{B}}$ with base vectors $\overset{\star}{\mathbf{g}}_i$ are stated. For these three configurations the associated metric coefficients are given by

$$\begin{aligned} \overset{\circ}{G}_{ij} &= \overset{\circ}{\mathbf{g}}_i \cdot \overset{\circ}{\mathbf{g}}_j & - & \text{initial,} \\ G_{ij} &= \mathbf{g}_i \cdot \mathbf{g}_j & - & \text{current, deformed and damaged,} \\ \overset{\star}{G}_{ij} &= \overset{\star}{\mathbf{g}}_i \cdot \overset{\star}{\mathbf{g}}_j & - & \text{inelastically deformed and damaged.} \end{aligned} \quad (2.1)$$

The complete deformation, i.e. elastic and inelastic, is represented by the metric transformation tensor

$$\mathbf{Q} = Q^i_{.j} \mathbf{g}_i \otimes \mathbf{g}^j = \overset{\circ}{G}^{ik} G_{kj} \mathbf{g}_i \otimes \mathbf{g}^j = \overset{\circ}{G}^{ij} \mathbf{g}_i \otimes \mathbf{g}_j = \mathbf{F}\mathbf{F}^T = \mathbf{B} \quad (2.2)$$

where it clearly can be seen that \mathbf{Q} is a mixed variant representation of the left Cauchy-Green-Tensor \mathbf{B} while \mathbf{F} is the deformation gradient. This formulation goes back to Lehmann [94, 95] and has been used by Brüning [25].

Analogically the elastic metric transformation tensor

$$\mathbf{Q}^{\text{el}} = \left(Q^{\text{el}}\right)^i_{.j} \mathbf{g}_i \otimes \mathbf{g}^j = \overset{\star}{G}^{ik} G_{kj} \mathbf{g}_i \otimes \mathbf{g}^j \quad (2.3)$$

and the inelastic metric transformation tensor

$$\mathbf{Q}^{\text{pd}} = \left(Q^{\text{pd}} \right)^i_{.j} \mathbf{g}_i \otimes \mathbf{g}^j = \overset{\circ}{G}^{ik} \overset{\star}{G}_{kj} \mathbf{g}_i \otimes \mathbf{g}^j, \quad (2.4)$$

characterizing plastic and damage related deformations, are introduced and directly transferred to the current configuration. In this representation it is evident that \mathbf{Q}^{el} is a symmetric tensor whereas \mathbf{Q}^{pd} is non-symmetric. Given these definitions, the outcome is the multiplicative decomposition of the metric transformation tensor

$$\mathbf{Q} = \mathbf{Q}^{\text{pd}} \mathbf{Q}^{\text{el}}. \quad (2.5)$$

Now the logarithmic Hencky strain tensor

$$\mathbf{A} = \frac{1}{2} \ln \mathbf{Q} = \frac{1}{2} \ln \left(Q^i_{.j} \right) \mathbf{g}_i \otimes \mathbf{g}^j = A^i_{.j} \mathbf{g}_i \otimes \mathbf{g}^j \quad (2.6)$$

and the elastic Hencky strain tensor

$$\mathbf{A}^{\text{el}} = \frac{1}{2} \ln \mathbf{Q}^{\text{el}} \quad (2.7)$$

can be defined, indicating that the elastic strains are kinematically independent from the inelastic deformations. Additionally, the non-symmetric objective Oldroyd rate of the metric transformation tensor

$$\dot{\mathbf{Q}} = \overset{\circ}{G}^{ik} \dot{G}_{kj} \mathbf{g}_i \otimes \mathbf{g}^j \quad (2.8)$$

and the symmetric strain rate

$$\dot{\mathbf{H}} = \frac{1}{2} \dot{G}^i_{.j} \mathbf{g}^i \otimes \mathbf{g}^j = \frac{1}{2} G^{ik} \dot{G}_{kj} \mathbf{g}_i \otimes \mathbf{g}^j \quad (2.9)$$

are defined. By straight forward manipulations it can be shown that

$$\dot{\mathbf{H}} = \frac{1}{2} \mathbf{Q}^{-1} \dot{\mathbf{Q}} \quad (2.10)$$

which leads by the use of Eq. (2.5) to the additive decomposition

$$\begin{aligned} \dot{\mathbf{H}} &= \frac{1}{2} \left(\mathbf{Q}^{\text{el}} \right)^{-1} \left(\mathbf{Q}^{\text{pd}} \right)^{-1} \left[\dot{\mathbf{Q}}^{\text{pd}} \mathbf{Q}^{\text{el}} + \mathbf{Q}^{\text{pd}} \dot{\mathbf{Q}}^{\text{el}} \right] \\ &= \frac{1}{2} \left(\mathbf{Q}^{\text{el}} \right)^{-1} \left(\mathbf{Q}^{\text{pd}} \right)^{-1} \dot{\mathbf{Q}}^{\text{pd}} \mathbf{Q}^{\text{el}} + \frac{1}{2} \left(\mathbf{Q}^{\text{el}} \right)^{-1} \dot{\mathbf{Q}}^{\text{el}} \\ &= \dot{\mathbf{H}}^{\text{pd}} + \dot{\mathbf{H}}^{\text{el}} \end{aligned} \quad (2.11)$$

defining the first part of the sum as the inelastic strain rate, $\dot{\mathbf{H}}^{\text{pd}}$, and

the second part as the elastic one, $\dot{\mathbf{H}}^{\text{el}}$.

2.1.2 Undamaged configurations

Corresponding to the damaged configurations fictitious undamaged configurations are introduced. In particular by fictitiously removing the initial damage of the initial configuration $\overset{\circ}{\mathcal{B}}$, this results in the initial, fictitious undamaged configuration $\overset{\circ}{\mathcal{E}}$ with base vectors $\overset{\circ}{\mathbf{e}}_i$. Furthermore, the current fictitious undamaged configuration \mathcal{E} with base vectors \mathbf{e}_i is obtained from the current placement \mathcal{B} ; finally the plastically deformed, but stress free configuration $\overset{*}{\mathcal{E}}$ with base vectors $\overset{*}{\mathbf{e}}_i$ corresponds to the intermediate configuration $\overset{*}{\mathcal{B}}$. To these placements the corresponding metric coefficients are

$$\begin{aligned} \overset{\circ}{E}_{ij} &= \overset{\circ}{\mathbf{e}}_i \cdot \overset{\circ}{\mathbf{e}}_j & - & \text{initial,} \\ E_{ij} &= \mathbf{e}_i \cdot \mathbf{e}_j & - & \text{current, elastically and plastically deformed,} \\ \overset{*}{E}_{ij} &= \overset{*}{\mathbf{e}}_i \cdot \overset{*}{\mathbf{e}}_j & - & \text{plastically deformed.} \end{aligned} \tag{2.12}$$

Analogically to the damaged configurations, metric transformation tensors between these configurations can be defined and directly transferred to the configuration \mathcal{E} with basis \mathbf{e}_i . Furthermore, with the use of the damage deformation gradient

$$\tilde{\mathbf{F}} = \mathbf{g}_i \otimes \mathbf{e}^i \tag{2.13}$$

these metric transformation tensors can be pushed forward to the current configuration \mathcal{B} with basis \mathbf{g}_i , see [26] for more details. So finally this results in the representations

$$\begin{aligned} \bar{\mathbf{Q}} &= \overset{\circ}{E}^{ik} E_{kj} \mathbf{g}_i \otimes \mathbf{g}^j \\ \bar{\mathbf{Q}}^{\text{el}} &= \overset{*}{E}^{ik} E_{kj} \mathbf{g}_i \otimes \mathbf{g}^j \\ \bar{\mathbf{Q}}^{\text{pl}} &= \overset{\circ}{E}^{ik} \overset{*}{E}_{kj} \mathbf{g}_i \otimes \mathbf{g}^j \end{aligned} \tag{2.14}$$

clearly indicating that these tensors are non-symmetric. That allows the multiplicative decomposition

$$\bar{\mathbf{Q}} = \bar{\mathbf{Q}}^{\text{pl}} \bar{\mathbf{Q}}^{\text{el}}. \tag{2.15}$$

This leads to the definition of the effective logarithmic strain tensor

$$\bar{\mathbf{A}} = \frac{1}{2} \ln \bar{\mathbf{Q}} \quad (2.16)$$

and to the effective logarithmic elastic strain tensor

$$\bar{\mathbf{A}}^{\text{el}} = \frac{1}{2} \ln \bar{\mathbf{Q}}^{\text{el}} \quad (2.17)$$

as well as to the effective strain rate

$$\begin{aligned} \dot{\bar{\mathbf{H}}} &= \frac{1}{2} \bar{\mathbf{Q}}^{-1} \dot{\bar{\mathbf{Q}}} \\ &= \frac{1}{2} (\bar{\mathbf{Q}}^{\text{el}})^{-1} (\bar{\mathbf{Q}}^{\text{pl}})^{-1} \dot{\bar{\mathbf{Q}}}^{\text{pl}} \bar{\mathbf{Q}}^{\text{el}} + \frac{1}{2} (\bar{\mathbf{Q}}^{\text{el}})^{-1} \dot{\bar{\mathbf{Q}}}^{\text{el}} \\ &= \dot{\bar{\mathbf{H}}}^{\text{pl}} + \dot{\bar{\mathbf{H}}}^{\text{el}} \end{aligned} \quad (2.18)$$

whereas the additional decomposition is introduced defining plastic strain rate tensor $\dot{\bar{\mathbf{H}}}^{\text{pl}}$ as the first part of the sum and the elastic strain rate tensor $\dot{\bar{\mathbf{H}}}^{\text{el}}$ as the second part of the sum.

2.1.3 Damage tensors

The kinematic relations between the damaged and undamaged configurations, i.e. the kinematics of damage, are characterized by the introduction of metric transformation tensors and the corresponding logarithmic strain measures. By considering the simultaneous motion of the real body and the corresponding fictitious undamaged one, the metric transformation tensors

$$\begin{aligned} \overset{\circ}{\mathbf{R}} &= \overset{\circ}{R}{}^i{}_j \mathbf{g}_i \otimes \mathbf{g}^j = \overset{\circ}{E}{}^{ik} \overset{\circ}{G}{}_{kj} \mathbf{g}_i \otimes \mathbf{g}^j \\ \mathbf{R} &= R{}^i{}_j \mathbf{g}_i \otimes \mathbf{g}^j = E{}^{ik} G{}_{kj} \mathbf{g}_i \otimes \mathbf{g}^j \\ \overset{*}{\mathbf{R}} &= \overset{*}{R}{}^i{}_j \mathbf{g}_i \otimes \mathbf{g}^j = \overset{*}{E}{}^{ik} \overset{*}{G}{}_{kj} \mathbf{g}_i \otimes \mathbf{g}^j \end{aligned} \quad (2.19)$$

are introduced which are directly transferred to the final configuration \mathcal{B} .

In detail, as shown in Fig. 2.1, the tensor $\overset{\circ}{\mathbf{R}}$ characterizes the generally known initial damage, as the tensor \mathbf{R} reflects the final damage between the final damaged configuration \mathcal{B} and the final, fictitious undamaged configuration \mathcal{E} . Finally the metric tensor $\overset{*}{\mathbf{R}}$ relates the elastically unloaded configurations $\overset{*}{\mathcal{B}}$ and $\overset{*}{\mathcal{E}}$ to each other. Following Murakami [121] and Brünig [25, 26], the definition of proper damage variables has to be realized on the elastically unloaded configurations, since the current

damage tensor \mathbf{R} also depends on the current deformation. Therefore, the damage tensor $\overset{\star}{\mathbf{R}}$ is used to define the appropriate damage measurement and the corresponding logarithmic damage strain tensor

$$\mathbf{A}^{\text{da}} = \frac{1}{2} \ln \overset{\star}{\mathbf{R}} \quad (2.20)$$

as well as the damage strain rate

$$\dot{\mathbf{H}}^{\text{da}} = \frac{1}{2} \overset{\star}{\mathbf{R}}^{-1} \dot{\overset{\star}{\mathbf{R}}} \quad (2.21)$$

can be defined.

2.1.4 Decomposition of deformation

With these definitions one can notice at Fig. 2.1 that the metric transformation tensor \mathbf{Q} can be multiplicatively decomposed

$$\mathbf{Q} = \overset{\circ}{\mathbf{R}}^{-1} \bar{\mathbf{Q}}^{\text{pl}} \overset{\star}{\mathbf{R}} \mathbf{Q}^{\text{el}}, \quad (2.22)$$

into parts reflecting the initial damage, the plastic deformation, the complete damage state and the elastic deformation. Starting out with Eq. (2.10) and using Eq. (2.22), after some manipulation as shown in Eqs. (2.23)

$$\begin{aligned} \dot{\mathbf{H}} &= \frac{1}{2} \mathbf{Q}^{-1} \dot{\mathbf{Q}} \\ &= \frac{1}{2} \left(\mathbf{Q}^{\text{el}} \right)^{-1} \overset{\star}{\mathbf{R}}^{-1} \left(\bar{\mathbf{Q}}^{\text{pl}} \right)^{-1} \overset{\circ}{\dot{\mathbf{R}}} \\ &\quad \overset{\circ}{\mathbf{R}}^{-1} \left[\dot{\bar{\mathbf{Q}}}^{\text{pl}} \overset{\star}{\mathbf{R}} \mathbf{Q}^{\text{el}} + \bar{\mathbf{Q}}^{\text{pl}} \dot{\overset{\star}{\mathbf{R}}} \mathbf{Q}^{\text{el}} + \bar{\mathbf{Q}}^{\text{pl}} \overset{\star}{\mathbf{R}} \dot{\mathbf{Q}}^{\text{el}} \right] \\ &= \frac{1}{2} \overset{\circ}{\mathbf{R}}^{-1} \left(\bar{\mathbf{Q}}^{\text{pl}} \right) \left(\bar{\mathbf{Q}}^{\text{pl}} \right) \dot{\bar{\mathbf{Q}}}^{\text{pl}} \bar{\mathbf{Q}}^{\text{el}} \overset{\circ}{\mathbf{R}} \\ &\quad + \frac{1}{2} \left(\mathbf{Q}^{\text{el}} \right)^{-1} \overset{\star}{\mathbf{R}}^{-1} \dot{\overset{\star}{\mathbf{R}}} \mathbf{Q}^{\text{el}} + \frac{1}{2} \left(\mathbf{Q}^{\text{el}} \right)^{-1} \dot{\mathbf{Q}}^{\text{el}} \\ &= \overset{\circ}{\mathbf{R}}^{-1} \dot{\bar{\mathbf{H}}}^{\text{pl}} \overset{\circ}{\mathbf{R}} + \left(\mathbf{Q}^{\text{el}} \right)^{-1} \dot{\mathbf{H}}^{\text{da}} \mathbf{Q}^{\text{el}} + \dot{\mathbf{H}}^{\text{el}} \end{aligned} \quad (2.23)$$

the result is a complete additive decomposition of the strain rate tensor into an effective plastic, a damage and an elastic part.

As frequently used in homogenization theories, it is assumed that the configurations $\overset{\star}{\mathcal{B}}$ and \mathcal{B} relate in the same way as the configurations $\overset{\star}{\mathcal{E}}$

and \mathcal{E} , see [26], means

$$\mathbf{Q}^{\text{el}} = \bar{\mathbf{Q}}^{\text{el}} \quad (2.24)$$

which leads to the equivalence of the elastic strain tensors

$$\mathbf{A}^{\text{el}} = \frac{1}{2} \ln \mathbf{Q}^{\text{el}} = \frac{1}{2} \ln \bar{\mathbf{Q}}^{\text{el}} = \bar{\mathbf{A}}^{\text{el}} \quad (2.25)$$

where Eqs. (2.7, 2.17) have been used and to the equivalence of the elastic strain rates

$$\dot{\mathbf{H}}^{\text{el}} = \frac{1}{2} \left(\mathbf{Q}^{\text{el}} \right)^{-1} \dot{\mathbf{Q}}^{\text{el}} = \dot{\bar{\mathbf{H}}}^{\text{el}}. \quad (2.26)$$

2.2 Thermodynamics

Based on the kinematics of damaged and effective undamaged configurations, the concepts of thermodynamics are applied. In this context the effective undamaged configurations are used to formulate the thermo-elastic-plastic constitutive equations, the anisotropically damaged configurations are used to formulate thermo-elastic-plastic-damaged constitutive behavior [28]. In this section, the thermodynamic principles are used to provide the necessary equations to be able to formulate the constitutive equations of the following section.

2.2.1 Undamaged configurations

This section covers the thermodynamics of elastic-plastic continua which are related in this context to the kinematics of the effective undamaged configurations. The subject has been discussed by Brünig and Driemeier [32], who realize simulations of Taylor impact tests considering elastic-plastic material behavior.

The rate of the effective specific mechanical work $\dot{\hat{w}}$ is additively decomposed into elastic and plastic parts, where Eq. (2.18) is used, and the corresponding work conjugate effective Kirchhoff stress tensor $\bar{\mathbf{T}} = \bar{T}_{.j}^i \mathbf{g}_i \otimes \mathbf{g}^j$ is introduced

$$\rho_o \dot{\hat{w}} = \rho_o \dot{\hat{w}}^{\text{el}} + \rho_o \dot{\hat{w}}^{\text{pl}} = \bar{\mathbf{T}} \cdot \dot{\bar{\mathbf{H}}} = \bar{\mathbf{T}} \cdot \dot{\bar{\mathbf{H}}}^{\text{el}} + \bar{\mathbf{T}} \cdot \dot{\bar{\mathbf{H}}}^{\text{pl}}. \quad (2.27)$$

Here ρ_o represents the mass density of the initial configuration, $\dot{\hat{w}}^{\text{el}}$ the elastic part of the effective specific mechanical work and $\dot{\hat{w}}^{\text{pl}}$ the plastic part of the effective specific mechanical work. Introducing the local formulation of the first law of thermodynamics, the rate of the effective

specific internal energy $\dot{\bar{u}}$ is represented as

$$\rho_o \dot{\bar{u}} = \bar{\mathbf{T}} \cdot \dot{\bar{\mathbf{H}}} - \text{div} \bar{\mathbf{q}} = \rho_o \dot{\bar{w}} - \text{div} \bar{\mathbf{q}} \quad (2.28)$$

where $\bar{\mathbf{q}}$ is the Kirchhoff heat flux vector. Besides that the effective Helmholtz free energy

$$\bar{\phi} = \bar{u} - \theta \bar{s} \quad (2.29)$$

is introduced by the Legendre transformation where θ represents the absolute temperature and its work conjugate variable \bar{s} is the effective specific entropy. The rate of the effective Helmholtz free energy can be derived to

$$\dot{\bar{\phi}} = \dot{\bar{u}} - \dot{\theta} \bar{s} - \theta \dot{\bar{s}}, \quad (2.30)$$

which can be rearranged and introduced into Eq. (2.28) leading to

$$\text{div} \bar{\mathbf{q}} = \rho_o \left(\dot{\bar{w}} - \dot{\bar{\phi}} - \dot{\theta} \bar{s} - \theta \dot{\bar{s}} \right). \quad (2.31)$$

Furthermore, the effective specific Helmholtz free energy is additively decomposed into a thermo-elastic part $\bar{\phi}^{\text{el}}$ and a thermo-plastic part $\bar{\phi}^{\text{pl}}$

$$\bar{\phi} \left(\mathbf{A}^{\text{el}}, \gamma, \theta \right) = \bar{\phi}^{\text{el}} \left(\mathbf{A}^{\text{el}}, \theta \right) + \bar{\phi}^{\text{pl}} \left(\gamma, \theta \right) \quad (2.32)$$

where γ denotes the scalar plastic internal variable, characterizing the plastic material behavior. By using this decomposition it is assumed that the elastic deformations are independent from the plastic variables whereas $\bar{\phi}^{\text{el}}$ can be recovered completely and $\bar{\phi}^{\text{pl}}$ corresponds to dissipative plastic processes [32]. In addition, the rate of Eq. (2.32) can be obtained to

$$\dot{\bar{\phi}} = \frac{\partial \bar{\phi}^{\text{el}}}{\partial \mathbf{A}^{\text{el}}} \cdot \dot{\mathbf{A}}^{\text{el}} + \frac{\partial \bar{\phi}^{\text{pl}}}{\partial \gamma} \dot{\gamma} + \frac{\partial \bar{\phi}}{\partial \theta} \dot{\theta}. \quad (2.33)$$

Furthermore the Clausius-Duhem-inequality or second law of thermodynamics can be written as

$$\rho_o \dot{\bar{s}} + \text{div} \left(\frac{\bar{\mathbf{q}}}{\theta} \right) \geq 0. \quad (2.34)$$

Within this thesis fast deformation processes are studied which can be assumed to be adiabatic, i.e. $\bar{\mathbf{q}} = \mathbf{0}$ as well as $\text{div} \bar{\mathbf{q}} = 0$ and thus Eq. (2.34) reduces to $\dot{\bar{s}} \geq 0$. This fact is considered in the following manipulations and the terms considering the heat flux $\bar{\mathbf{q}}$ are neglected.

Following Lehmann [96] and Brünig [26] one arrives with Eqs. (2.31, 2.27,

2.33) for adiabatic processes at the inequality

$$\left(\bar{\mathbf{T}} - \rho_o \frac{\partial \bar{\phi}^{\text{el}}}{\partial \mathbf{A}^{\text{el}}} \right) \cdot \dot{\mathbf{H}}^{\text{el}} - \rho_o \left(\bar{s} + \frac{\partial \bar{\phi}}{\partial \theta} \right) \dot{\theta} + \rho_o \dot{w}^{\text{pl}} - \rho_o \frac{\partial \bar{\phi}^{\text{pl}}}{\partial \gamma} \dot{\gamma} \geq 0. \quad (2.35)$$

By considering the hyperelastic constitutive law

$$\bar{\mathbf{T}} = \rho_o \frac{\partial \bar{\phi}^{\text{el}}}{\partial \mathbf{A}^{\text{el}}} \quad (2.36)$$

as well as the thermic constitutive law

$$\bar{s} = - \frac{\partial \bar{\phi}}{\partial \theta} \quad (2.37)$$

Eq. (2.35) reduces to

$$\rho_o \dot{w}^{\text{pl}} - \rho_o \frac{\partial \bar{\phi}^{\text{pl}}}{\partial \gamma} \dot{\gamma} = \bar{\mathbf{T}} \cdot \dot{\mathbf{H}}^{\text{pl}} - \rho_o \frac{\partial \bar{\phi}^{\text{pl}}}{\partial \gamma} \dot{\gamma} \geq 0 \quad (2.38)$$

which characterizes the internal dissipation [32] and is a restriction for the formulation of constitutive equations.

The evolution equation for the temperature is obtained by starting out with Eq. (2.31) and making use of the hyperelastic constitutive law (2.36) as well as the thermic constitutive law (2.37) to

$$c_F \dot{\theta} = \dot{\psi}^{\text{pl}} + \dot{\psi}^{\text{el}} \quad (2.39)$$

where the specific heat

$$c_F = -\rho_o \theta \frac{\partial^2 \bar{\phi}}{\partial \theta^2} \quad (2.40)$$

has been introduced. Furthermore in Eq. (2.39)

$$\dot{\psi}^{\text{pl}} = \bar{\mathbf{T}} \cdot \dot{\mathbf{H}}^{\text{pl}} - \rho_o \frac{\partial \bar{\phi}^{\text{pl}}}{\partial \gamma} \dot{\gamma} + \rho_o \theta \frac{\partial^2 \bar{\phi}^{\text{pl}}}{\partial \theta \partial \gamma} \dot{\gamma} \quad (2.41)$$

represents the plastic and

$$\dot{\psi}^{\text{el}} = \rho_o \theta \frac{\partial^2 \bar{\phi}^{\text{el}}}{\partial \theta \partial \mathbf{A}^{\text{el}}} \cdot \dot{\mathbf{A}}^{\text{el}} \quad (2.42)$$

the thermo-elastic contribution to heating. The task of plastic dissipation has been widely discussed in literature, see for instance [19, 140, 28] where also its rate and temperature dependence is discussed. The present proposal follows Rosakis et al. [140], where the fraction of plastic work

converted to heating

$$\xi = \frac{\dot{\psi}^{\text{pl}}}{\rho_o \dot{w}^{\text{pl}}} \quad (2.43)$$

is introduced [28], which leads to

$$\dot{\psi}^{\text{pl}} = \xi \rho_o \bar{w}^{\text{el}} = \xi \bar{\mathbf{T}} \cdot \dot{\mathbf{H}}^{\text{pl}}. \quad (2.44)$$

Furthermore, experiments realized by Mićunović et al. [116] can be taken into account which indicate that the increase in temperature due to elastic deformation is very small compared with that one due to the plastic dissipation. Thus this leads to the assumption that the elastic effects are negligible, therefore Eq. (2.39) reduces to

$$c_F = \xi \bar{\mathbf{T}} \cdot \dot{\mathbf{H}}^{\text{pl}}. \quad (2.45)$$

2.2.2 Damaged configurations

For the anisotropically damaged state the rate of the specific mechanical work \dot{w} is additively decomposed into an elastic part, a plastic part and a damage part. Furthermore the work conjugate Kirchhoff stress tensor $\mathbf{T} = T_{,j}^i \mathbf{g}_i \otimes \mathbf{g}^j$ is introduced and by the use of Eq. (2.23) one arrives at the final expression of

$$\begin{aligned} \rho_o \dot{w} &= \rho_o \dot{w}^{\text{el}} + \rho_o \dot{w}^{\text{pl}} + \rho_o \dot{w}^{\text{da}} \\ &= \mathbf{T} \cdot \dot{\mathbf{H}} = \mathbf{T} \cdot \left[\dot{\mathbf{H}}^{\text{el}} + \mathbf{R}^{-1} \dot{\mathbf{H}}^{\text{pl}} \mathbf{R} + \left(\mathbf{Q}^{\text{el}} \right)^{-1} \dot{\mathbf{H}}^{\text{da}} \mathbf{Q}^{\text{el}} \right]. \end{aligned} \quad (2.46)$$

Furthermore the rate of the specific internal energy is given by

$$\rho_o \dot{u} = \rho_o \dot{w} - \text{div} \mathbf{q} \quad (2.47)$$

where \mathbf{q} describes the Kirchhoff heat flux vector. Additionally, the specific Helmholtz free energy ϕ is introduced by the Legendre transformation to $\phi = u - \theta s$, whereas

$$\dot{\phi} = \dot{u} - \dot{\theta} s - \theta \dot{s} \quad (2.48)$$

represents its rate. Here s represents the specific entropy of the current damaged configuration. Furthermore, the Helmholtz free energy is additively decomposed into a thermo-elastic, a thermo-plastic and a thermo-damage part

$$\phi \left(\mathbf{A}^{\text{el}}, \mathbf{A}^{\text{da}}, \gamma, \mu, \theta \right) = \phi^{\text{el}} \left(\mathbf{A}^{\text{el}}, \mathbf{A}^{\text{da}}, \theta \right) + \phi^{\text{pl}} \left(\gamma, \theta \right) + \phi^{\text{da}} \left(\mu, \theta \right). \quad (2.49)$$

where μ represents the internal damage variable characterizing the current damage state. Here it can be noted that the thermo-elastic part ϕ^{el} depends on the elastic \mathbf{A}^{el} and damage strains \mathbf{A}^{da} clearly reflecting that damage influences the elastic behavior of the material which reflects the experimental observations. Furthermore, the thermo-plastic part ϕ^{pl} which reflects the plastic hardening is related to the internal plastic variable γ and the thermo-damage part ϕ^{da} which is due to damage processes is related to the internal damage variable μ . Thus it is assumed that the plastic and the damage behavior as well as the elastic and damage behavior are independent from each other, [100]. In addition all three parts depend on the temperature θ .

This leads to the representation of the rate of the Helmholtz free energy function

$$\dot{\phi} = \frac{\partial \phi^{\text{el}}}{\partial \mathbf{A}^{\text{el}}} \cdot \dot{\mathbf{A}}^{\text{el}} + \frac{\partial \phi^{\text{el}}}{\partial \mathbf{A}^{\text{da}}} \cdot \dot{\mathbf{A}}^{\text{da}} + \frac{\partial \phi^{\text{pl}}}{\partial \gamma} \dot{\gamma} + \frac{\partial \phi^{\text{da}}}{\partial \mu} \dot{\mu} + \frac{\partial \phi}{\partial \theta} \dot{\theta}. \quad (2.50)$$

For the damaged state the second law of thermodynamics related to the internal dissipative processes can be written as

$$\rho_o \dot{s} + \text{div} \left(\frac{\mathbf{q}}{\theta} \right) \geq 0. \quad (2.51)$$

In continuation with Eqs. (2.47, 2.48) and the identity

$$\text{div} \left(\frac{\mathbf{q}}{\theta} \right) = \frac{1}{\theta} \text{div} \mathbf{q} - \frac{1}{\theta^2} \mathbf{q} \cdot \text{grad } \theta \quad (2.52)$$

Eq. (2.51) can be rewritten to

$$\rho_o \left[\dot{w} - \dot{\phi} - \dot{\theta} s \right] - \frac{1}{\theta} \cdot \text{grad } \theta \geq 0. \quad (2.53)$$

Again considering only adiabatic processes, i.e. $\mathbf{q} = \mathbf{0}$, the second law of thermodynamics reduces to $\dot{s} \geq 0$ and Eq. (2.53) can be written as

$$\dot{w} - \dot{\phi} - \dot{\theta} s \geq 0. \quad (2.54)$$

Following Lehmann [96] and Brünig [26] as well as Eq (2.54) and making use of Eqs. (2.46) and (2.50) one arrives at

$$\begin{aligned} \left(\mathbf{T} - \rho_o \frac{\partial \phi^{\text{el}}}{\partial \mathbf{A}^{\text{el}}} \right) \cdot \dot{\mathbf{H}}^{\text{el}} - \rho_o \left(s + \frac{\partial \phi}{\partial \theta} \right) \dot{\theta} + \rho_o \dot{w}^{\text{pl}} - \rho_o \frac{\partial \phi^{\text{pl}}}{\partial \gamma} \dot{\gamma} \\ + \rho_o \dot{w}^{\text{da}} - \rho_o \frac{\partial \phi^{\text{el}}}{\partial \mathbf{A}^{\text{da}}} \cdot \dot{\mathbf{A}}^{\text{da}} - \rho_o \frac{\partial \phi^{\text{da}}}{\partial \mu} \dot{\mu} \geq 0. \end{aligned} \quad (2.55)$$

In addition the hyperelastic constitutive law

$$\mathbf{T} = \rho_o \frac{\partial \phi^{\text{el}}}{\partial \mathbf{A}^{\text{el}}} \quad (2.56)$$

as well as the thermic constitutive law

$$s = -\frac{\partial \phi}{\partial \theta} \quad (2.57)$$

are taken into account and the inequality Eq. (2.55) is split while assuming a stronger formulation one arrives at

$$\dot{w}^{\text{pl}} - \frac{\partial \phi^{\text{pl}}}{\partial \gamma} \dot{\gamma} \geq 0 \quad (2.58)$$

and

$$\tilde{\mathbf{T}} \cdot \dot{\mathbf{H}}^{\text{da}} - \rho_o \frac{\partial \phi^{\text{el}}}{\partial \mathbf{A}^{\text{da}}} \cdot \dot{\mathbf{A}}^{\text{da}} - \rho_o \dot{\phi}^{\text{da}} \geq 0 \quad (2.59)$$

describing the internal dissipation. Here it is important to point out that the plastic potential function of Eq. (2.58) is not needed in detail since the plastic strain rate $\dot{\mathbf{H}}^{\text{pl}}$ is based on the potential function $\bar{\phi}^{\text{pl}}$ which is related to the undamaged configuration and has to satisfy Eq. (2.38). But Eq. (2.59) is applied since ϕ^{el} and ϕ^{da} are considered and furthermore it expresses that the damage part of the deformation will be given by $\dot{\mathbf{H}}^{\text{da}}$ introduced in Eq. (2.21) while the corresponding work conjugate stress tensor is

$$\tilde{\mathbf{T}} = \mathbf{Q}^{\text{el}} \mathbf{T} (\mathbf{Q}^e)^{-1}. \quad (2.60)$$

2.3 Constitutive equations

2.3.1 Effective undamaged configurations

On the effective undamaged configurations a thermo-elastic-plastic material model is adapted [28]. The hyperelastic isotropic material behavior with temperature dependence is governed by the effective Helmholtz free energy function

$$\begin{aligned} \rho_o \bar{\phi}^{\text{el}}(\mathbf{A}^{\text{el}}, \theta) &= G \mathbf{A}^{\text{el}} \cdot \mathbf{A}^{\text{el}} + \frac{1}{2} \left(K - \frac{2}{3} G \right) \left(\text{tr} \mathbf{A}^{\text{el}} \right)^2 \\ &+ 3K \alpha_T (\theta - \theta_o) \text{tr} \mathbf{A}^{\text{el}} + \rho_o \bar{h}(\theta) \end{aligned} \quad (2.61)$$

where G represents the shear modulus and K the bulk modulus of the matrix material. Furthermore, α_T denotes for the coefficient of thermal expansion and \bar{h} is an explicit function of temperature. By differentiation to the corresponding strain measure, one obtains with Eq. (2.36) the work-conjugate effective Kirchhoff stress tensor

$$\bar{\mathbf{T}} = 2G\mathbf{A}^{\text{el}} + \left(K - \frac{2}{3}G\right) \text{tr}\mathbf{A}^{\text{el}}\mathbf{1} - 3K\alpha_T(\theta - \theta_o)\mathbf{1}. \quad (2.62)$$

The plasticity model is based on the experiments by Spitzig et al. [150, 147, 148] who studied the plastic behavior of different ductile metals and detected important influence of the hydrostatic pressure on the yield behavior. Thus a Drucker-Prager-type yield condition

$$f^{\text{pl}} = a\bar{I}_1 + \sqrt{\bar{J}_2} - c(\gamma, \dot{\gamma}, \theta) = 0 \quad (2.63)$$

is chosen, where a , the hydrostatic stress coefficient, depends on the stress state, but the fraction a/c based on experimental observations can be assumed to be constant. Furthermore, $\bar{I}_1 = \text{tr}\bar{\mathbf{T}}$ is the first invariant of the effective stress tensor, Eq. (2.62), and $\bar{J}_2 = \frac{1}{2}\text{dev}\bar{\mathbf{T}} \cdot \text{dev}\bar{\mathbf{T}}$ the second invariant of its deviator, whereas $c(\gamma, \dot{\gamma}, \theta)$ is the equivalent stress measure depending on the equivalent plastic strain γ , the equivalent plastic strain rate $\dot{\gamma}$ and the temperature θ . The rate- and temperature dependent plastic behavior is described by

$$c(\gamma, \dot{\gamma}, \theta) = \tilde{c}(\gamma) f_1(\dot{\gamma}) f_2(\theta) \quad (2.64)$$

which is a multiplicative decomposition, which is similar to the frequently applied Johnson–Cook [72, 73] material model and based on experimental data [28]. The rate-independent hardening behavior is characterized by the power law

$$\tilde{c}(\gamma) = \tilde{c}_o \left(\frac{H_o\gamma}{n\tilde{c}_o} + 1 \right)^n \quad (2.65)$$

where \tilde{c}_o represents the initial yield stress, H_o the hardening parameter and n the hardening exponent [26]. The fact that the material reacts stiffer with increasing strain rates is characterized by the strain rate hardening function

$$f_1(\dot{\gamma}) = 1 + d \left(\frac{\dot{\gamma} - \dot{\gamma}_o}{\dot{\gamma}_o} \right)^m \quad (2.66)$$

valid for $\dot{\gamma} > \dot{\gamma}_o$ where d and m are further material parameters and $\dot{\gamma}_o$ is the strain rate of the quasi-static reference test. The circumstances, that

with increasing temperature a softer material response has been observed in experiments with metals is characterized by the thermal softening function

$$f_2(\theta) = 1 - b \operatorname{sgn}\left(\frac{\theta - \theta_o}{\theta_m - \theta_o}\right) \left[\operatorname{abs}\left(\frac{\theta - \theta_o}{\theta_m - \theta_o}\right) \right]^q \quad (2.67)$$

where b and q are further material parameters, whereas θ_o represents the reference temperature and θ_m is the melting temperature [28]. Furthermore, Eq. (2.67) has the constraint $f_2 > 0$ which leads to

$$\theta < \left(\frac{1}{b}\right)^{1/q} \theta_m. \quad (2.68)$$

Since the partial derivatives of Eq. (2.64) are needed during numerical integration in Sec. 2.4.2, these are given here for completeness:

$$\frac{\partial c}{\partial \gamma} = f_1(\dot{\gamma}) f_2(\theta) H_o \left(\frac{H_o \gamma}{n \tilde{c}_o} + 1 \right)^{(n-1)}, \quad (2.69)$$

$$\frac{\partial c}{\partial \dot{\gamma}} = \tilde{c}(\gamma) f_2(\theta) \frac{m d}{\dot{\gamma}_o} \left(\frac{\dot{\gamma} - \dot{\gamma}_o}{\dot{\gamma}_o} \right)^{(m-1)} \quad (2.70)$$

and

$$\frac{\partial c}{\partial \theta} = -\tilde{c}(\gamma) f_1(\dot{\gamma}) \frac{b q}{\theta_m} \left(\frac{\theta - \theta_o}{\theta_m - \theta_o} \right)^{(q-1)}. \quad (2.71)$$

where the constraint of Eq. (2.68) has to be respected.

Based on the experiments by Spitzig et al. [149] who observed only marginal plastic volume increase the plastic potential function is chosen to be non-associated, i.e. neglecting the influence of \bar{I}_1 to

$$g^{\text{pl}}(\bar{\mathbf{T}}, \gamma, \theta) = \sqrt{\bar{J}_2} - c_o(\gamma, \theta) \quad \text{where} \quad c_o(\gamma, \theta) = \tilde{c}(\gamma) f_2(\theta) \quad (2.72)$$

is the temperature dependent scalar effective stress measure. This leads to the effective plastic strain rate

$$\dot{\mathbf{H}}^{\text{pl}} = \dot{\lambda} \frac{\partial g^{\text{pl}}}{\partial \bar{\mathbf{T}}} = \dot{\lambda} \frac{1}{2\sqrt{\bar{J}_2}} \operatorname{dev} \bar{\mathbf{T}} = \dot{\gamma} \frac{1}{\sqrt{2\bar{J}_2}} \operatorname{dev} \bar{\mathbf{T}} = \dot{\gamma} \bar{\mathbf{N}} \quad (2.73)$$

where $\dot{\lambda} = \sqrt{2}\dot{\gamma}$ is a non negative scalar factor and $\bar{\mathbf{N}}$ is the normalized deviatoric stress direction tensor.

2.3.2 Damaged configurations

Following the ideas of Hayakawa et al. [65] and Brüning [26] who assumed that the original material behaves isotropic and linear-elastic, see also Eq. (2.61) and consequently the thermo-elastic free energy function ϕ^{el} has to be quadratic in \mathbf{A}^{el} . Furthermore it can be expected that ϕ^{el} decreases as damage develops and thus it will be chosen linear in \mathbf{A}^{da} [65] which leads with the demand of completeness in its invariants to

$$\begin{aligned} \rho_o \phi^{\text{el}}(\mathbf{A}^{\text{el}}, \mathbf{A}^{\text{da}}, \theta) &= G \mathbf{A}^{\text{el}} \cdot \mathbf{A}^{\text{el}} + \frac{1}{2} \left(K - \frac{2}{3} G \right) \left(\text{tr} \mathbf{A}^{\text{el}} \right)^2 \\ &\quad + 3K \alpha_T (\theta - \theta_o) \text{tr} \mathbf{A}^{\text{el}} + \rho_o h(\theta) \\ &\quad + \eta_1 \text{tr} \mathbf{A}^{\text{da}} \left(\text{tr} \mathbf{A}^{\text{el}} \right)^2 + \eta_2 \text{tr} \mathbf{A}^{\text{da}} \mathbf{A}^{\text{el}} \cdot \mathbf{A}^{\text{el}} \\ &\quad + \eta_3 \text{tr} \mathbf{A}^{\text{el}} \mathbf{A}^{\text{da}} \cdot \mathbf{A}^{\text{el}} + \eta_4 \mathbf{A}^{\text{el}} \cdot \left(\mathbf{A}^{\text{el}} \mathbf{A}^{\text{da}} \right). \end{aligned} \quad (2.74)$$

Here η_1 to η_4 are further material parameters which are called due to nature elastic damage modulus whereas h is an explicit function of temperature. Having a closer look at Eq. (2.74), the representation with invariants can be easily noticed and furthermore, the first two terms reflect the pure elastic behavior whereas the third term describes the temperature influence on the material volume while the fourth term reflects pure temperature influence and the last four terms characterize the decrease of the elastic properties due to damage.

By differentiation to the corresponding strain measure, see Eq. (2.56), one obtains the associated Kirchhoff stress tensor

$$\begin{aligned} \mathbf{T} &= 2 \left(G + \eta_2 \text{tr} \mathbf{A}^{\text{da}} \right) \mathbf{A}^{\text{el}} - 3K \alpha_T (\theta - \theta_o) \mathbf{1} \\ &\quad + \left[\left(K - \frac{2}{3} G + 2\eta_1 \text{tr} \mathbf{A}^{\text{da}} \right) \text{tr} \mathbf{A}^{\text{el}} + \eta_3 \left(\mathbf{A}^{\text{da}} \cdot \mathbf{A}^{\text{el}} \right) \right] \mathbf{1} \\ &\quad + \eta_3 \text{tr} \mathbf{A}^{\text{el}} \mathbf{A}^{\text{da}} + \eta_4 \left(\mathbf{A}^{\text{el}} \mathbf{A}^{\text{da}} + \mathbf{A}^{\text{da}} \mathbf{A}^{\text{el}} \right) \end{aligned} \quad (2.75)$$

which is linear in \mathbf{A}^{el} and \mathbf{A}^{da} . In this expression one can notice nicely the influence of temperature on the volumetric part as well as the influence of damage on the elastic properties. Furthermore, it is important to realize that the stress tensor of the damaged configuration \mathbf{T} (Eq. (2.75)) and the effective stress tensor of the effective undamaged configuration $\bar{\mathbf{T}}$ (Eq. (2.62)) evolve from two different free energy functions which are related to two different configurations and thus no stress or strain equivalence is needed such as in the effective stress concept [99, 98].

Recent experimental observations have shown that the onset as well as

the evolution of damage depends besides the stress intensity mainly on the stress triaxiality

$$\eta = \sigma_m / \sigma_{\text{eq}} = \frac{I_1}{3\sqrt{3}J_2}, \quad (2.76)$$

where the commonly used alternative definition of Eq. (2.76) is given with σ_m being the mean normal stress and σ_{eq} being the von Mises equivalent stress. Bao and Wierzbicki [10] discussed the different mechanisms that lead to fracture and concluded that for high stress triaxialities the leading damage process is guided by void growth and that for negative stress triaxialities above a cut of value [11] below which no damage occurs, the leading damage mechanism are micro shear cracks. Between these two domains a zone occurs where both mechanisms play a role [10]. These ideas have been carried on and are illustrated in Fig. 2.2 as well as reflected in the damage condition (2.77), see [31, 30, 29].

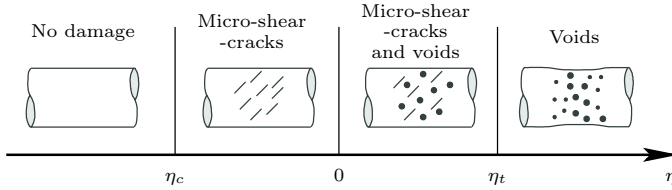


Figure 2.2: Different damage mechanisms depending on stress triaxiality η

Similar to the yield condition of Eq. (2.63), which characterizes the onset of plasticity, the rate and temperature dependent damage condition is introduced

$$f^{\text{da}} = \tilde{\alpha} I_1 + \tilde{\beta} \sqrt{J_2} - \tilde{\sigma}(\mu, \dot{\mu}, \theta) = 0 \quad (2.77)$$

which characterizes the onset of damage. Here $I_1 = \text{tr}\mathbf{T}$ is the first invariant of the stress tensor (Eq. (2.75)), $J_2 = \frac{1}{2} \text{dev}\mathbf{T} \cdot \text{dev}\mathbf{T}$ is the second deviatoric invariant and $\tilde{\sigma}(\mu, \dot{\mu}, \theta)$ is the equivalent damage stress measure, depending on the equivalent damage strain μ , the equivalent damage strain rate $\dot{\mu}$ and the absolute temperature θ . The above mentioned stress triaxiality dependence is reflected in the parameters

$$\tilde{\alpha} = \begin{cases} 0 & \text{for } \eta_c \leq \eta \leq 0 \\ 1/3 & \text{for } \eta > 0 \end{cases} \quad (2.78)$$

and

$$\tilde{\beta} = \begin{cases} 1 & \text{for } \eta_c \leq \eta \leq 0 \\ 1 - \frac{1}{\eta_t} \eta & \text{for } 0 < \eta < \eta_t \\ 0 & \text{for } \eta \geq \eta_t \end{cases} \quad (2.79)$$

which are chosen with respect to triaxiality [31, 57]. For instance, for negative triaxialities, i.e. $\eta < 0$ where micro shear cracks are the main damage mechanisms, the volumetric influence of I_1 is neglected and for high triaxialities, i.e. $\eta > \eta_t$ where void growth is the main damage mechanism, the deviatoric influence of $\sqrt{J_2}$ is neglected, see Fig. 2.2. For intermediate triaxialities, i.e. $0 < \eta < \eta_t$, both mechanisms are considered while a simple linear relation for $\tilde{\beta}$ between 0 and η_t has been used [30, 29].

The damage softening behavior is characterized by

$$\sigma(\mu, \dot{\mu}, \theta) = \tilde{\sigma}(\mu) f_3(\dot{\mu}) f_2(\theta) \quad (2.80)$$

using a multiplicative decomposition in analogy to the decomposition used for plastic hardening in Eq. (2.64) into a rate-independent $\tilde{\sigma}(\mu)$, a strain rate dependent $f_3(\dot{\mu})$ and a temperature dependent part $f_2(\theta)$. Here it should be noted that it is very difficult to obtain any information from experiments regarding the softening behavior and thus the analogy to the plastic behavior is chosen. In detail the rate-independent softening function is chosen to be quadratic in μ to

$$\tilde{\sigma}(\mu) = \frac{-\left(\tilde{H}_o \mu_e + \tilde{\sigma}_o\right)}{\mu_e^2} \mu^2 + \tilde{H}_o \mu + \tilde{\sigma}_o \quad (2.81)$$

and diagrammed in Fig. 2.3 where $\tilde{\sigma}_o$ represents the initial damage strength, μ_e the fictitious value where the damage softening relation reaches zero and \tilde{H}_o represents the slope of the static plastic hardening function (Eq. (2.65)) taken at the onset of damage [33]. By this choice the onset of damage is characterized by a smooth transition and evolves more steady than in the bilinear approach proposed in [26]. Furthermore, the damage strain rate behavior is characterized by

$$f_3(\dot{\mu}) = 1 + h \left(\frac{\dot{\mu} - \dot{\mu}_o}{\dot{\mu}_o} \right)^r \quad (2.82)$$

where $\dot{\mu}_o$ is the reference damage strain rate and h as well as r are further material parameters. Since the partial derivatives of Eq. (2.80) are needed during numerical integration in Sec. 2.4.2, these are given here for

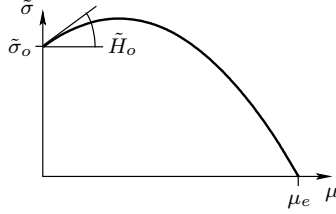


Figure 2.3: Damage softening law

completeness:

$$\frac{\partial \sigma}{\partial \mu} = \left(-2 \left(\frac{\partial \tilde{c}}{\partial \gamma} \mu_e + \tilde{\sigma}_o \right) \mu + \frac{\partial \tilde{c}}{\partial \gamma} \right) f_3(\dot{\mu}) f_2(\theta), \quad (2.83)$$

$$\frac{\partial \sigma}{\partial \dot{\mu}} = \tilde{\sigma}(\mu) f_2(\theta) \frac{hr}{\mu_o} \left(\frac{\dot{\mu} - \dot{\mu}_o}{\dot{\mu}_o} \right)^{(r-1)} \quad (2.84)$$

and

$$\frac{\partial \sigma}{\partial \theta} = -\tilde{\sigma}(\mu) f_3(\dot{\mu}) \frac{bq}{\theta_m} \left(\frac{\theta - \theta_o}{\theta_m} \right)^{(q-1)}. \quad (2.85)$$

In addition, the damage potential function is chosen to

$$g^{\text{da}}(\mathbf{T}, \mu, \theta) = \alpha I_1 + \beta \sqrt{J_2} - g_o(\mu, \theta) \quad (2.86)$$

where

$$g_o = \tilde{\sigma}(\mu) f_2(\theta) \quad (2.87)$$

is the temperature dependent scalar effective stress measure. This leads to the damage strain rate tensor

$$\dot{\mathbf{H}}^{\text{da}} = \dot{\mu} \frac{\partial g^{\text{da}}}{\partial \mathbf{T}} = \dot{\mu} \alpha \mathbf{1} + \dot{\mu} \beta \frac{1}{2\sqrt{J_2}} \text{dev} \mathbf{T} \quad (2.88)$$

where the first term is related to isotropic growth of voids, i.e. volumetric deformations, and the second term relates to the change of shape and orientation of micro-defects [26].

In this connection it is important to point out that it is not an easy task to characterize the onset of damage as well as the damage evolution and final fracture. This circumstance is mainly caused by the lack

of experimental data due to the fact that experiments, specially on the micro-scale, are difficult to realize and hence this subject is still subject of ongoing research. To overcome these difficulties mainly three approaches are currently followed up:

- The design of new experimental setups and special specimen geometries to study the process of ongoing damage and fracture at different stress states, see for instance [119, 31, 54, 53], while these experiments are frequently accompanied by numerical simulations.
- Micro experimental studies of ongoing damage and fracture by a X-ray tomography technique, see for instance [112, 156].
- Numerical micro-mechanical studies where the behavior of pores in an elastic-plastic material are studied while the results can be used to extract information for phenomenological continuum damage models. These studies may be seen in a tradition with the initial works of Gurson [61] and Needleman [126] while current publications for example, are [29, 160, 35].

Our ongoing studies focus on the one hand on micromechanical numerical studies [34, 35] and on the other hand on the experimental study of damage and the design of new specimens [31, 29] with damage occurrence at different stress states. This work-in-progress denotes the influence of the Lode parameter on damage initiation and evolution which might result into a modification of the damage condition and damage law while within this thesis a as far as possible confirmed state-of-the-art approach has been used. Special focus in the future might be given to the influence of strain rate and temperature on the damage initiation and evolution.

2.3.3 Fracture behavior

Moreover, the internal damage variable μ can be used to define a simple triaxiality dependent fracture criterion [29]. The corresponding fracture condition can be written in the form

$$f^{\text{cr}} = \mu - \mu_{\text{cr}} = 0 \quad (2.89)$$

where μ_{cr} is the triaxiality dependent critical equivalent damage strain:

$$\mu_{\text{cr}} = \begin{cases} \mu_f & \text{for } \eta > \eta_f \\ \frac{\mu_f - \mu_o}{\eta_f} \eta + \mu_o & \text{for } 0 \leq \eta \leq \eta_f \\ \mu_o & \text{for } \eta < 0. \end{cases} \quad (2.90)$$

The here introduced material parameters μ_f and μ_o represent the critical tension and compression values of the equivalent damage strain while η_f

is the fracture transmission triaxiality. The propagation of the macro crack is numerically realized through an element erosion technique.

2.4 Numerical integration of constitutive rate equations

The numerical integration of the constitutive rate equations is often realized by a radial return algorithm, see for instance [145, 47]. In contrast, Nemat-Nasser [127] presented a new algorithm which first assumes the complete deformation as plastic and then realizes an elastic corrector step. This algorithm was adopted by Brünig [23] and augmented for elastic-plastic-damaged solids [27].

In this section the numerical integration algorithm for the undamaged configurations and for the damaged configurations is presented. Thus the following three steps will be described in detail:

1. By the use of the plastic consistency condition $\dot{f}^{\text{pl}} = 0$ and the damage consistency condition $\dot{f}^{\text{da}} = 0$, constitutive scalar rate equations are developed.
2. The numerical integration algorithm including the inelastic predictor step and the elastic corrector step is presented.
3. By the use of the calculated equivalent strain increments, the total strain increment is split into a plastic and an elastic part or respectively into a plastic, a damage and an elastic part.

This section is based on Brünig [27] and Brünig and Gerke [33].

2.4.1 Scalar rate equations

Undamaged configurations

Starting out with the plastic consistency condition $\dot{f}^{\text{pl}} = 0$ and making use of

$$\dot{\bar{I}}_1 = \dot{\bar{\mathbf{T}}} \cdot \mathbf{1} \quad (2.91)$$

and

$$\left(\sqrt{\bar{J}_2} \right) \dot{} = \frac{1}{2\sqrt{\bar{J}_2}} \text{dev} \bar{\mathbf{T}} \cdot \dot{\bar{\mathbf{T}}} = \frac{1}{\sqrt{2}} \bar{\mathbf{N}} \cdot \dot{\bar{\mathbf{T}}} \quad (2.92)$$

one arrives at

$$\frac{1}{\sqrt{2}} \bar{\mathbf{N}} \cdot \dot{\bar{\mathbf{T}}} + a \mathbf{1} \cdot \dot{\bar{\mathbf{T}}} = \left(1 - \frac{a}{c} \bar{I}_1 \right) \dot{c} \quad (2.93)$$

where $\bar{\mathbf{N}}$ is the normalized deviatoric part of $\bar{\mathbf{T}}$. Considering Eq. (2.62) and introducing

$$\begin{aligned}\dot{\bar{\mathbf{T}}} &= \frac{\partial \bar{\mathbf{T}}}{\partial \mathbf{A}^{\text{el}}} \dot{\mathbf{H}}^{\text{el}} + \frac{\partial \bar{\mathbf{T}}}{\partial \theta} \dot{\theta} \\ &= 2G\dot{\mathbf{H}}^{\text{el}} + \left[\left(K - \frac{2}{3}G \right) \text{tr} \dot{\mathbf{H}}^{\text{el}} - 3K\alpha_T \dot{\theta} \right] \mathbf{1}\end{aligned}\quad (2.94)$$

and

$$\bar{\mathbf{N}} \cdot \dot{\bar{\mathbf{T}}} = 2G\bar{\mathbf{N}} \cdot \dot{\mathbf{H}}^{\text{el}} \quad (2.95)$$

as well as

$$\mathbf{1} \cdot \dot{\bar{\mathbf{T}}} = 3K\text{tr} \dot{\mathbf{H}}^{\text{el}} - 9K\alpha_T \dot{\theta} \quad (2.96)$$

Eq. (2.93) reads as follows

$$\sqrt{2}G\bar{\mathbf{N}} \cdot \dot{\mathbf{H}}^{\text{el}} + a \left(3K\text{tr} \dot{\mathbf{H}}^{\text{el}} - 9K\alpha_T \dot{\theta} \right) = \left(1 - \frac{a}{c} \bar{I}_1 \right) \dot{c}. \quad (2.97)$$

Furthermore, by the use of Eq. (2.18), remodeling Eq. (2.45) to

$$\dot{\theta} = \xi \frac{\sqrt{2\bar{J}_2}}{c_F} \dot{\gamma} \quad (2.98)$$

and using some straight forward manipulations, one finally arrives at the scalar rate equation

$$\dot{c} - \alpha_2 \dot{\gamma} = \alpha_1 \dot{c} \quad (2.99)$$

where the strain rate measure

$$\dot{c} = \dot{c}_{\text{iso}} + \frac{3aK}{\sqrt{2}G} \dot{c}_{\text{vol}} \quad (2.100)$$

is decomposed into an isochoric and an volumetric part:

$$\dot{c}_{\text{iso}} = \bar{\mathbf{N}} \cdot \dot{\mathbf{H}} \quad \text{and} \quad \dot{c}_{\text{vol}} = \text{tr} \dot{\mathbf{H}}. \quad (2.101)$$

Furthermore the abbreviations

$$\alpha_2 = 1 + \frac{9aK\alpha_T \xi \sqrt{\bar{J}_2}}{Gc_F} \quad (2.102)$$

and

$$\alpha_1 = \frac{1 - \frac{a}{c} \bar{I}_1}{\sqrt{2}G} \quad (2.103)$$

have been used.

Damaged configurations

Starting from the plastic consistency condition in form of Eq. (2.97) and making use of Eqs. (2.98, 2.23) as well as of the plastic evolution law Eq. (2.73) and the damage evolution law Eq. (2.88), one arrives at the first plastic scalar rate equation

$$\sqrt{2}G_1 (\dot{\epsilon}_1 + k_1 \dot{\gamma} - k_2 \dot{\mu}) = \dot{c} \quad (2.104)$$

which is related to the undamaged configuration. Here

$$G_1 = \frac{G}{1 - \frac{a}{c} \bar{I}_1} \quad (2.105)$$

represents a weighted shear modulus of the matrix material and

$$\dot{\epsilon}_1 = \frac{1}{\sqrt{2}G} \left(\sqrt{2}G\bar{\mathbf{N}} + 3aK\mathbf{1} \right) \cdot \dot{\mathbf{H}} \quad (2.106)$$

is the equivalent strain rate measure. Furthermore the notations

$$k_1 = \mathbf{R}\bar{\mathbf{N}}\mathbf{R}^{-1} \cdot \bar{\mathbf{N}} + \frac{9aK\alpha_T\xi\sqrt{\bar{J}_2}}{G_{cF}} \quad (2.107)$$

and

$$k_2 = \frac{1}{\sqrt{2}G} \mathbf{Q}^{\text{el}} \left(\sqrt{2}G\bar{\mathbf{N}} + 3aK\mathbf{1} \right) \left(\mathbf{Q}^{\text{el}} \right)^{-1} \cdot \left(\alpha\mathbf{1} + \frac{\tilde{\beta}}{\sqrt{2}}\tilde{\mathbf{N}} \right) \quad (2.108)$$

have been used to write the expression in a more compact way and $\tilde{\mathbf{N}}$ is the normalized deviatoric part of $\bar{\mathbf{T}}$. The damage consistency condition $\dot{j}^{\text{da}} = 0$ can be rewritten to

$$\tilde{\alpha} (\text{tr}\mathbf{T}) \cdot + \frac{1}{2} \tilde{\beta} (\text{dev}\mathbf{T} \cdot \text{dev}\mathbf{T}) \cdot - \dot{\sigma} = 0 \quad (2.109)$$

and with the use of $\text{dev}\mathbf{T} = \sqrt{2}\bar{J}_2\bar{\mathbf{N}}$ and $\text{tr}\mathbf{T} = \mathbf{1} \cdot \mathbf{T}$ one arrives at

$$\tilde{\alpha}\mathbf{1} \cdot \dot{\mathbf{T}} + \frac{\tilde{\beta}}{\sqrt{2}}\bar{\mathbf{N}} \cdot \dot{\mathbf{T}} = \dot{\sigma} \quad (2.110)$$

while with Eq. (2.75)

$$\begin{aligned}
\dot{\mathbf{T}} &= \frac{\partial \mathbf{T}}{\partial \mathbf{A}^{\text{el}}} \dot{\mathbf{H}}^{\text{el}} + \frac{\partial \mathbf{T}}{\partial \mathbf{A}^{\text{da}}} \dot{\mathbf{H}}^{\text{da}} + \frac{\partial \mathbf{T}}{\partial \theta} \dot{\theta} \\
&= 2 \left(G + \eta_2 \text{tr} \mathbf{A}^{\text{da}} \right) \dot{\mathbf{H}}^{\text{el}} + \left(K - \frac{2}{3} G + \eta_1 \text{tr} \dot{\mathbf{H}}^{\text{el}} \right) \mathbf{1} \\
&\quad + \eta_3 \mathbf{A}^{\text{da}} \cdot \dot{\mathbf{H}}^{\text{el}} + \eta_3 \text{tr} \dot{\mathbf{H}}^{\text{el}} \mathbf{A}^{\text{da}} + \eta_4 \left(\dot{\mathbf{H}}^{\text{el}} \mathbf{A}^{\text{da}} + \mathbf{A}^{\text{da}} \dot{\mathbf{H}}^{\text{el}} \right) \\
&\quad + 2\eta_2 \text{tr} \dot{\mathbf{H}}^{\text{da}} \mathbf{A}^{\text{el}} + \eta_1 \text{tr} \dot{\mathbf{H}}^{\text{da}} \text{tr} \mathbf{A}^{\text{el}} \mathbf{1} + \eta_3 \left(\dot{\mathbf{H}}^{\text{da}} \cdot \mathbf{A}^{\text{el}} \right) \mathbf{1} \\
&\quad + \eta_3 \text{tr} \mathbf{A}^{\text{el}} \dot{\mathbf{H}}^{\text{da}} + \eta_4 \left(\mathbf{A}^{\text{el}} \dot{\mathbf{H}}^{\text{da}} + \dot{\mathbf{H}}^{\text{da}} \mathbf{A}^{\text{el}} \right) + 3K \alpha_T \dot{\theta} \mathbf{1}
\end{aligned} \tag{2.111}$$

can be determined and the scalar products

$$\begin{aligned}
\mathbf{1} \cdot \dot{\mathbf{T}} &= \left[3K + (6\eta_1 + 2\eta_2 + \eta_3) \text{tr} \mathbf{A}^{\text{da}} \right] \text{tr} \dot{\mathbf{H}}^{\text{el}} \\
&\quad + (3\eta_3 + 2\eta_4) \mathbf{A}^{\text{da}} \cdot \dot{\mathbf{H}}^{\text{el}} \\
&\quad + (6\eta_1 + 2\eta_2 + \eta_3) \text{tr} \mathbf{A}^{\text{el}} \text{tr} \dot{\mathbf{H}}^{\text{da}} \\
&\quad + (3\eta_3 + 2\eta_4) \mathbf{A}^{\text{el}} \cdot \dot{\mathbf{H}}^{\text{da}} + 9K \alpha_T \dot{\theta}
\end{aligned} \tag{2.112}$$

and

$$\begin{aligned}
\mathbf{N} \cdot \dot{\mathbf{T}} &= 2 \left(G + \eta_2 \text{tr} \mathbf{A}^{\text{da}} \right) \mathbf{N} \cdot \dot{\mathbf{H}}^{\text{el}} + \eta_3 \left(\mathbf{N} \cdot \mathbf{A}^{\text{da}} \right) \text{tr} \dot{\mathbf{H}}^{\text{el}} \\
&\quad + \eta_4 \left(\mathbf{N} \mathbf{A}^{\text{da}} + \mathbf{A}^{\text{da}} \mathbf{N} \right) \cdot \dot{\mathbf{H}}^{\text{el}} + 2\eta_2 \left(\mathbf{N} \cdot \mathbf{A}^{\text{el}} \right) \text{tr} \dot{\mathbf{H}}^{\text{da}} \\
&\quad + \eta_3 \text{tr} \mathbf{A}^{\text{el}} \mathbf{N} \cdot \dot{\mathbf{H}}^{\text{da}} + \eta_4 \left(\mathbf{N} \mathbf{A}^{\text{el}} + \mathbf{A}^{\text{el}} \mathbf{N} \right) \cdot \dot{\mathbf{H}}^{\text{da}}
\end{aligned} \tag{2.113}$$

lead with Eqs. (2.23 ,2.45, 2.73, 2.88) and corresponding traces to

$$\sqrt{2} G_2 (\dot{\epsilon}_2 + k_3 \dot{\gamma} - k_4 \dot{\mu}) = \dot{\sigma} \tag{2.114}$$

being the second scalar-valued rate constitutive equation related to the damaged configuration. Here the shear modulus of the damaged material

$$G_2 = G + \eta_2 \text{tr} \mathbf{A}^{\text{da}} \tag{2.115}$$

and the second equivalent strain rate measure

$$\dot{\epsilon}_2 = \frac{1}{\sqrt{2} G_2} \mathbf{C}_1 \cdot \dot{\mathbf{H}} \tag{2.116}$$

have been used. Furthermore the factors

$$k_3 = \frac{1}{\sqrt{2}G_2} \left(\mathbf{R}\mathbf{C}_1\mathbf{R}^{-1} \cdot \tilde{\mathbf{N}} + 9K\alpha_T\xi \frac{\sqrt{2\tilde{J}_2}}{c_F} \right) \quad (2.117)$$

and

$$k_4 = \frac{1}{\sqrt{2}G_2} \left[\mathbf{Q}^{\text{el}}\mathbf{C}_1 \left(\mathbf{Q}^{\text{el}} \right)^{-1} - \mathbf{C}_2 \right] \cdot \left[\alpha\mathbf{1} + \frac{\beta}{\sqrt{2}}\tilde{\mathbf{N}} \right] \quad (2.118)$$

make the expression easier to read, whereas the abbreviations

$$\begin{aligned} \mathbf{C}_1 = & \sqrt{2}\tilde{\beta}G_2\mathbf{N} + \left(3K_2 + \frac{\tilde{\beta}}{\sqrt{2}}\eta_3\mathbf{N} \cdot \mathbf{A}^{\text{da}} \right) \mathbf{1} \\ & + \frac{\tilde{\beta}}{\sqrt{2}}\eta_4 \left(\mathbf{N}\mathbf{A}^{\text{da}} + \mathbf{A}^{\text{da}}\mathbf{N} \right) + (3\eta_3 + \eta_4) \mathbf{A}^{\text{da}} \end{aligned} \quad (2.119)$$

and

$$\begin{aligned} \mathbf{C}_2 = & \frac{\tilde{\beta}}{\sqrt{2}}\eta_3\text{tr}\mathbf{A}^{\text{el}}\mathbf{N} \\ & + \left[\frac{\tilde{\beta}}{\sqrt{2}}2\eta_2\mathbf{N} \cdot \mathbf{A}^{\text{el}} + (6\eta_1 + 2\eta_2 + \eta_3) \text{tr}\mathbf{A}^{\text{el}} \right] \mathbf{1} \\ & + \frac{\tilde{\beta}}{\sqrt{2}}\eta_4 \left(\mathbf{N}\mathbf{A}^{\text{el}} + \mathbf{A}^{\text{el}}\mathbf{N} \right) + (3\eta_3 + 2\eta_4) \mathbf{A}^{\text{el}} \end{aligned} \quad (2.120)$$

have been used where the bulk modulus of the damaged material

$$K_2 = K + \left(2\eta_1 + \frac{2}{3}\eta_2 + \frac{1}{3}\eta_3 \right) \text{tr}\mathbf{A}^{\text{da}} \quad (2.121)$$

has been introduced.

2.4.2 Numerical integration

The inelastic predictor, elastic corrector integration algorithm starts in the case of elastic-plastic material behavior from the scalar valued rate equation described in Eq. (2.99) and in case of elastic-plastic-damaged material behavior from Eqs. (2.104, 2.114). These scalar valued rate equations now describe the complete material behavior including rate and temperature dependence, as well as anisotropic damage. The stress and deformation history is generated by straightforward one step midpoint integration of the scalar rate equations. Fig. 2.4 gives an overview of the notation used within this section noting that in difference to Sec. 3.2 the

notation $\Delta t^{n+1/2} = \Delta t$ has been used.

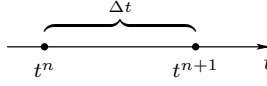


Figure 2.4: Notation of integration algorithm

Undamaged configurations

The numerical integration of Eq. (2.99) over the time interval $t_n \leq \hat{t} \leq t_{n+1}$ with $t_{n+1} = t_n + \Delta t$ results in

$$\alpha_1 (c_{n+1} - c_n) = \Delta \varepsilon - \alpha_2 \Delta \gamma. \quad (2.122)$$

For the plastic predictor step the whole deformation is assumed to be plastic

$$\Delta \gamma_{\text{pr}} = \frac{1}{\alpha_2} \Delta \varepsilon \quad (2.123)$$

which allows to calculate the temperature increase and the predictor temperature to

$$\Delta \theta_{\text{pr}} = \xi \frac{\sqrt{2\bar{J}_2}}{c_F} \Delta \gamma_{\text{pr}} \quad \text{and} \quad \theta_{\text{pr}} = \theta_n + \Delta \theta_{\text{pr}} \quad (2.124)$$

as well as predictor strain rate and the predictor strain to

$$\dot{\gamma}_{\text{pr}} = \frac{\Delta \gamma_{\text{pr}}}{\Delta t} \quad \text{and} \quad \gamma_{\text{pr}} = \gamma_n + \Delta \gamma_{\text{pr}}. \quad (2.125)$$

Now with equivalent stress – equivalent plastic strain relation of Eq. (2.64) the equivalent stress can be evaluated at $c_{\text{pr}}(\gamma_{\text{pr}}, \dot{\gamma}_{\text{pr}}, \theta_{\text{pr}})$ to complete the predictor step. Obviously in Eq. (2.123) the equivalent plastic strain has been overestimated and the error has to be corrected by an elastic corrector step

$$\Delta_{\text{er}} c = c_{\text{pr}} - c_{n+1} = c_{\text{pr}} - c_n - \frac{\alpha_2}{\alpha_1} \dot{\gamma}_{\text{er}} \Delta t. \quad (2.126)$$

With the assumptions for the constitutive relation

$$\Delta_{\text{er}} c = \frac{\partial c}{\partial \gamma} \Delta_{\text{er}} \gamma + \frac{\partial c}{\partial \theta} \xi \frac{\sqrt{\bar{J}_2}}{c_F} \Delta_{\text{er}} \gamma + \frac{\partial c}{\partial \dot{\gamma}} \dot{\gamma}_{\text{er}} \quad (2.127)$$

where the partial derivatives of the plastic hardening law Eqs. (2.69, 2.70, 2.71) are used and for

$$\dot{\gamma}_{\text{er}} = \frac{\Delta_{\text{er}}\gamma}{\Delta t} \quad (2.128)$$

one arrives at

$$\Delta_{\text{er}}\gamma = \frac{c_{\text{pr}} - c_n}{\frac{\alpha_2}{\alpha_1} + \frac{\partial c}{\partial \gamma} + \frac{\partial c}{\partial \theta} \xi \frac{\sqrt{J_2}}{c_F} + \frac{1}{\Delta t} \frac{\partial c}{\partial \dot{\gamma}}} \quad (2.129)$$

where the partial derivatives are evaluated at the predictor location. To complete the iteration step

$$\Delta\gamma = \Delta\gamma_{\text{pr}} - \Delta_{\text{er}}\gamma \quad \text{and} \quad \gamma_{n+1} = \gamma_n + \Delta\gamma \quad (2.130)$$

are calculated, which allows the determination of

$$\Delta\theta = \Delta\theta_{\text{pr}} - \xi \frac{\sqrt{2J_2}}{c_F} \Delta_{\text{er}}\gamma \quad \text{and} \quad \theta_{n+1} = \theta_n + \Delta\theta \quad (2.131)$$

as well as

$$\dot{\gamma}_{n+1} = \frac{\Delta\gamma}{\Delta t}. \quad (2.132)$$

With these values the plastic hardening function Eq. (2.64) can be evaluated at $c_{n+1}(\gamma_{n+1}, \dot{\gamma}_{n+1}, \theta_{n+1})$ and thus the new equivalent stress is determined.

Damaged configurations

Analogical to integration algorithm for elastic-plastic material behavior the integration of the scalar rate equations (2.104) and (2.114) leads to

$$\begin{aligned} \Delta c &= c_{n+1} - c_n = \sqrt{2}G_1 (\Delta\varepsilon_1 - k_1\Delta\gamma - k_2\Delta\mu) \quad \text{and} \\ \Delta\sigma &= \sigma_{n+1} - \sigma_n = \sqrt{2}G_2 (\Delta\varepsilon_2 - k_3\Delta\gamma - k_4\Delta\mu). \end{aligned} \quad (2.133)$$

Now assuming in the predictor step all the deformation as inelastic, the terms in parentheses lead to the system of equations

$$\begin{bmatrix} k_1 & k_2 \\ k_3 & k_4 \end{bmatrix} \begin{bmatrix} \Delta\gamma_{\text{pr}} \\ \Delta\mu_{\text{pr}} \end{bmatrix} = \begin{bmatrix} \Delta\varepsilon_1 \\ \Delta\varepsilon_2 \end{bmatrix} \quad (2.134)$$

which can be written in more compact way to

$$\mathbf{k}\Delta\gamma_{\text{pr}} = \boldsymbol{\varepsilon} \quad (2.135)$$

and the inversion

$$\Delta\gamma_{\text{pr}} = \mathbf{k}^{-1} \boldsymbol{\varepsilon} \quad (2.136)$$

results in the predictor equivalent strain increments $\Delta\gamma_{\text{pr}}$ and $\Delta\mu_{\text{pr}}$. Consequently the equivalent predictor strains

$$\gamma_{\text{pr}} = \gamma_n + \Delta\gamma_{\text{pr}} \quad \text{and} \quad \mu_{\text{pr}} = \mu_n + \Delta\mu_{\text{pr}} \quad (2.137)$$

as well as the predictor strain rates

$$\dot{\gamma}_{\text{pr}} = \frac{\Delta\gamma_{\text{pr}}}{\Delta t} \quad \text{and} \quad \dot{\mu}_{\text{pr}} = \frac{\Delta\mu_{\text{pr}}}{\Delta t} \quad (2.138)$$

and the predictor temperature

$$\Delta\theta_{\text{pr}} = \xi \frac{\sqrt{J_2}}{c_F} \Delta\gamma_{\text{pr}} \quad \text{and} \quad \theta_{\text{pr}} = \theta_n + \Delta\theta_{\text{pr}} \quad (2.139)$$

are calculated what allow the evaluation of equivalent stress – equivalent inelastic strain relations of Eq. (2.64) at c_{pr} ($\gamma_{\text{pr}}, \dot{\gamma}_{\text{pr}}, \theta_{\text{pr}}$) and of Eq. (2.80) at σ_{pr} ($\mu_{\text{pr}}, \dot{\mu}_{\text{pr}}, \theta_{\text{pr}}$) to complete the predictor step.

Since all deformation was assumed inelastic, this leads to an overestimation of the equivalent inelastic strains as well as of the corresponding equivalent stresses which will be corrected in the following corrector step. For the effective equivalent stress this leads to

$$\Delta_{\text{er}}c = c_{\text{pr}} - c_{n+1} = c_{\text{pr}} - c_n - \Delta c \quad (2.140)$$

while the error can be estimated by the constitutive relation to

$$\Delta_{\text{er}}c \cong \left(\frac{\partial c}{\partial \gamma} + \frac{1}{\Delta t} \frac{\partial c}{\partial \dot{\gamma}} + \frac{\partial c}{\partial \theta} \xi \frac{\sqrt{2J_2}}{c_F} \right) \Delta_{\text{er}}\gamma = \partial_{\gamma}c \Delta_{\text{er}}\gamma \quad (2.141)$$

which leads with Eq. (2.133₁) to the effective stress increment

$$\Delta c = \sqrt{2}G_1 (k_1 \Delta_{\text{er}}\gamma + k_2 \Delta_{\text{er}}\mu) = c_{\text{pr}} - c_n - \partial_{\gamma}c \Delta_{\text{er}}\gamma. \quad (2.142)$$

In the same manner the error in the equivalent damage stress can be calculated to

$$\Delta_{\text{er}}\sigma = \sigma_{\text{pr}} - \sigma_{n+1} = \sigma_{\text{pr}} - \sigma_n - \Delta c \quad (2.143)$$

and with the constitutive relation Eq. (2.80) the error can be estimated

to

$$\begin{aligned}\Delta_{\text{er}}\sigma &\cong \left(\frac{\partial\sigma}{\partial\mu} + \frac{1}{\Delta t} \frac{\partial\sigma}{\partial\dot{\mu}} \right) \Delta_{\text{er}}\mu + \frac{\partial\sigma}{\partial\theta} \xi \frac{\sqrt{2\bar{J}_2}}{c_F} \Delta_{\text{er}}\gamma \\ &= \partial_{\mu}\sigma \Delta_{\text{er}}\mu + \partial_{\dot{\mu}}\sigma \Delta_{\text{er}}\mu + \partial_{\theta}\sigma \Delta_{\text{er}}\gamma\end{aligned}\quad (2.144)$$

where the partial derivatives of the equivalent damage stress – equivalent strain relation presented in Eqs. (2.83, 2.84, 2.85) have been used. With the use of Eq. (2.133₂) one arrives at

$$\begin{aligned}\Delta\sigma &= \sqrt{2}G_2 (k_3\Delta_{\text{er}}\gamma + k_4\Delta_{\text{er}}\mu) \\ &= \sigma_{\text{pr}} - \sigma_n - \partial_{\mu}\sigma \Delta_{\text{er}}\mu + \partial_{\dot{\mu}}\sigma \Delta_{\text{er}}\mu.\end{aligned}\quad (2.145)$$

Now with Eqs. (2.142) and (2.145) the following system of equations

$$\begin{bmatrix} \sqrt{2}G_1k_1 + \partial_{\gamma}c & \sqrt{2}G_1k_2 \\ \sqrt{2}G_2k_3 + \partial_{\dot{\gamma}}\sigma & \sqrt{2}G_2k_4 + \partial_{\mu}\sigma \end{bmatrix} \begin{bmatrix} \Delta_{\text{er}}\gamma \\ \Delta_{\text{er}}\mu \end{bmatrix} = \begin{bmatrix} c_{\text{pr}} + c_n \\ \sigma_{\text{pr}} + \sigma_n \end{bmatrix}\quad (2.146)$$

can be assembled and used to calculate $\Delta_{\text{er}}\gamma$ and $\Delta_{\text{er}}\mu$. This system of equations can be written in a more compact form to

$$\mathbf{a}\Delta_{\text{er}}\boldsymbol{\gamma} = \Delta\mathbf{c}_{\text{pr}}.\quad (2.147)$$

By its inversion the error in the equivalent strain increments, combined in the vector $\Delta_{\text{er}}\boldsymbol{\gamma}$, can be calculated as

$$\Delta_{\text{er}}\boldsymbol{\gamma} = \mathbf{a}^{-1}\Delta\mathbf{c}_{\text{pr}}\quad (2.148)$$

and finally the equivalent strain increments are obtained

$$\Delta\boldsymbol{\gamma} = \Delta\boldsymbol{\gamma}_{\text{pr}} - \Delta_{\text{er}}\boldsymbol{\gamma}.\quad (2.149)$$

To complete the iteration, the updated equivalent strains

$$\gamma_{n+1} = \gamma_n + \Delta\gamma \quad \text{and} \quad \mu_{n+1} = \mu_n + \Delta\mu\quad (2.150)$$

as well as the current temperature

$$\Delta\theta = \Delta\theta_{\text{pr}} - \xi \frac{\sqrt{2\bar{J}_2}}{c_F} \Delta_{\text{er}}\gamma \quad \text{and} \quad \theta_{n+1} = \theta_n + \Delta\theta\quad (2.151)$$

can be computed. To be able to evaluate the plastic hardening law given in Eq. (2.64) at $c_{n+1}(\gamma_{n+1}, \dot{\gamma}_{n+1}, \theta_{n+1})$ and the damage softening law given in Eq. (2.80) at $\sigma_{n+1}(\mu_{n+1}, \dot{\mu}_{n+1}, \theta_{n+1})$, the current equivalent

strain rates are calculated to

$$\dot{\gamma}_{n+1} = \frac{\Delta\gamma}{\Delta t} \quad \text{and} \quad \dot{\mu}_{n+1} = \frac{\Delta\mu}{\Delta t}. \quad (2.152)$$

2.4.3 Tensorial quantities

Undamaged configurations

After the equivalent plastic and damage strains have been determined, the corresponding tensorial quantities have to be derived. Therefore, the plastic flow rule of Eq. (2.73) can be written in the form

$$\Delta\bar{\mathbf{H}}^{\text{pl}} = \Delta\gamma\bar{\mathbf{N}}_m = \text{dev}\Delta\bar{\mathbf{H}}^{\text{pl}} \quad (2.153)$$

with the effective normalized deviatoric midpoint stress

$$\bar{\mathbf{N}}_m = \frac{1}{2} [\bar{\mathbf{N}}_n + \bar{\mathbf{N}}_{n+1}] \quad (2.154)$$

whereas $\bar{\mathbf{N}}_{n+1}$ is currently unknown. Thus starting out from the normalized deviatoric stress tensors at t_n and t_{n+1}

$$\bar{\mathbf{N}}_n = \frac{1}{\sqrt{2\bar{J}_{2,n}}} \text{dev}\bar{\mathbf{T}}_n \quad \text{and} \quad \bar{\mathbf{N}}_{n+1} = \frac{1}{\sqrt{2\bar{J}_{2,n+1}}} \text{dev}\bar{\mathbf{T}}_{n+1} \quad (2.155)$$

as well as its difference

$$\begin{aligned} \text{dev}\Delta\bar{\mathbf{T}} &= \text{dev}\bar{\mathbf{T}}_{n+1} - \text{dev}\bar{\mathbf{T}}_n \\ &= 2G\text{dev}\Delta\bar{\mathbf{H}}^{\text{el}} = 2G \left(\text{dev}\Delta\mathbf{H} - \Delta\bar{\mathbf{H}}^{\text{pl}} \right) \end{aligned} \quad (2.156)$$

one arrives after some manipulations at

$$\bar{\mathbf{N}}_{n+1} = \frac{2G\text{dev}\Delta\mathbf{H} + \left(\sqrt{2\bar{J}_{2,n}} - 2G\Delta\gamma \right) \bar{\mathbf{N}}_n}{\sqrt{2\bar{J}_{2,n+1}} + G\Delta\gamma} \quad (2.157)$$

where the numerator contains only known quantities and thus can be evaluated whereas the tensor is normalized in the common way.

Damaged configurations

Starting out with Eqs. (2.153, 2.154) as well as with the damage evolution law described in Eq. (2.88) in the form

$$\Delta\mathbf{H}^{\text{da}} = \Delta\mu \left(\alpha\mathbf{1} + \frac{\beta}{\sqrt{2}} \mathbf{N}_m \right) \quad (2.158)$$

and

$$\operatorname{dev}\Delta\mathbf{H}^{\text{da}} = \Delta\mu \frac{\beta}{\sqrt{2}} \mathbf{N}_m \quad (2.159)$$

where

$$\mathbf{N}_m = \frac{1}{2} (\mathbf{N}_n + \mathbf{N}_{n+1}) \quad (2.160)$$

is the deviatoric midpoint normalized stress and furthermore taking into account the deviatoric stress increment

$$\operatorname{dev}\Delta\mathbf{T} = \operatorname{dev}\mathbf{T}_{n+1} - \operatorname{dev}\mathbf{T}_n = 2G\operatorname{dev}\Delta\mathbf{H}^{\text{el}} \quad (2.161)$$

as well as

$$\operatorname{dev}\bar{\mathbf{T}} = \sqrt{2\bar{J}_2}\bar{\mathbf{N}} = \sqrt{2}c \left(1 - \frac{a}{c}\bar{I}_1\right) \bar{\mathbf{N}} = \sqrt{2}\tilde{c}\bar{\mathbf{N}} \quad (2.162)$$

one arrives after some manipulations at

$$\begin{aligned} \sqrt{2}\tilde{c}_{n+1}\bar{\mathbf{N}}_{n+1} - \sqrt{2}\tilde{c}_n\bar{\mathbf{N}}_n &= 2G \left[\operatorname{dev}\Delta\mathbf{H} \right. \\ &\left. - \frac{1}{2}\Delta\gamma (\bar{\mathbf{N}}_{n+1} + \bar{\mathbf{N}}_n) - \frac{\beta}{2\sqrt{2}}\Delta\mu (\mathbf{N}_{n+1} + \mathbf{N}_n) \right], \end{aligned} \quad (2.163)$$

where \tilde{c}_{n+1} , $\bar{\mathbf{N}}_{n+1}$ and \mathbf{N}_{n+1} are currently unknown. To solve this under-determined situation, two assumptions are made: At the point of first occurrence of damage, already large plastic deformations have been developed and therefore a high level of saturation is reached. Due to this fact, the stress direction on the undamaged configuration changes marginally, meaning $\bar{\mathbf{N}}_{n+1} \simeq \bar{\mathbf{N}}_n \simeq \bar{\mathbf{N}}_m$. With this assumption the first term of Eq. (2.163) reads as $\sqrt{2}(\tilde{c}_{n+1} - \tilde{c}_n)\bar{\mathbf{N}}_n$ which results to be very small and therefore is set to 0. Herewith one arrives at the equation for the determination of the new stress direction on the damaged configuration

$$\mathbf{N}_{n+1} = \frac{2\operatorname{dev}\Delta\mathbf{H} + 2\Delta\gamma\bar{\mathbf{N}}_n - \frac{\beta}{\sqrt{2}\Delta\mu}\mathbf{N}_n}{\frac{\beta}{\sqrt{2}\Delta\mu}} \quad (2.164)$$

whereas only the numerator determinates the direction and is only computed and the tensor is normalized in the common way. With these assumptions, a robust numerical algorithm has been found to solve the under-determined situation.

3 Numerical procedure

In this thesis the Finite Element Method (FEM) has been used as a numerical technique to solve the stated problems. All simulations have been realized with the commercial FE-software LsDyna where the material model presented in chap. 2 was subjoined as user-defined material model. Considering this Sec. 3.1 gives a brief summary of the main ideas of the FEM with restrictions to the techniques used for the simulations within this thesis, based on [62, 169, 13]. Due to the fact that LsDyna uses explicit time integration, Sec. 3.2 deals with this subject, reflecting the principal thoughts of the central difference method. Finally Sec. 3.3 illuminates the connection in between the theory of Chap. 2 and the commercial FE-code LsDyna.

3.1 Finite Element procedure

Starting out, the momentum equation is stated

$$\operatorname{div} \left(\frac{1}{J} \mathbf{T} \right) + \rho \mathbf{b}^* = \rho \ddot{\mathbf{u}} \quad \text{in } \mathcal{B} \quad (3.1)$$

where $J = \det \mathbf{F}$ is the Jacobian, $\ddot{\mathbf{u}}$ is the acceleration vector and \mathbf{b}^* the vector of body force density and the boundary conditions

$$\frac{1}{J} \mathbf{n} \mathbf{T} = \mathbf{t}^*(t) \quad \text{on } \partial \mathcal{B}_{\mathbf{T}}, \quad (3.2)$$

$$\mathbf{u}(\overset{\circ}{\mathbf{x}}, t) = \mathbf{u}^*(\overset{\circ}{\mathbf{x}}, t) \quad \text{on } \partial \mathcal{B}_{\mathbf{u}} \quad \text{and} \quad (3.3)$$

$$(\mathbf{T}^+ - \mathbf{T}^-) \mathbf{n} = \mathbf{0} \quad \text{on } \partial \mathcal{B}_{\text{cont.}} \quad (3.4)$$

are stated. Eq. (3.2) reflects the natural or traction boundary conditions. Here \mathbf{n} is the unit outward normal vector on the boundary $\partial \mathcal{B}$ of the domain \mathcal{B} and \mathbf{t}^* is the stress vector on the part of the boundary $\partial \mathcal{B}_{\mathbf{T}}$. Next Eq. (3.3) describes the geometric or displacement boundary conditions, where \mathbf{u}^* are the known displacements on the boundary $\partial \mathcal{B}_{\mathbf{u}}$ and $\overset{\circ}{\mathbf{x}}$ is the position vector with respect to the initial configuration while Eq. (3.4) states the contact discontinuity where \mathbf{T}^+ and \mathbf{T}^- represent the stresses on both sides of the interior boundary $\partial \mathcal{B}_{\text{cont.}}$. To complete

the description of the problem, the initial conditions

$$\mathbf{u}(\overset{\circ}{\mathbf{x}}, t = 0) = \overset{\circ}{\mathbf{u}} \quad (3.5)$$

and

$$\dot{\mathbf{u}}(\overset{\circ}{\mathbf{x}}, t = 0) = \overset{\circ}{\mathbf{v}} \quad (3.6)$$

are quoted whereas Eq. (3.5) describes that the displacements $\overset{\circ}{\mathbf{u}}$ are known and Eq. (3.6) describes that the velocities $\overset{\circ}{\mathbf{v}}$ at time $t = 0$ are known.

Further integration of Eqs. (3.1, 3.2, 3.4) over the domain or accordingly its boundary, summation and multiplication with a trial function $\delta \mathbf{u}$ which satisfies the boundary conditions stated in Eq. (3.3) leads with the use of the divergence theorem to the weak form of the equilibrium

$$\delta \pi = \int_{\mathcal{B}} \frac{1}{J} \mathbf{T} \cdot \text{grad}^T \delta \mathbf{u} \, dv - \int_{\mathcal{B}} \rho (\mathbf{b}^* - \ddot{\mathbf{u}}) \cdot \delta \mathbf{u} \, dv - \int_{\partial \mathcal{B}_\sigma} \mathbf{t}^* \cdot \delta \mathbf{u} \, da = 0 \quad (3.7)$$

which is the fundamental equation of the finite element method. Through this approach it can be clearly seen that equilibrium Eq. (3.1) as well as the natural Eq. (3.2) and contact Eq. (3.4) boundary conditions are only fulfilled in a weak i.e. integral sense, whereas the displacement boundary condition Eq. (3.3) is met in its strong form since it is not part of the variational principle.

Furthermore, the domain \mathcal{B} is approximated by the unification of ne elements with an element domain \mathcal{B}_e

$$\mathcal{B} \simeq \bigcup^{ne} \mathcal{B}_e \quad (3.8)$$

and the continuous displacement vector \mathbf{u} is approximated by the use of shape functions N_i in natural coordinates $\hat{\xi}$, $\hat{\eta}$ and $\hat{\zeta}$, which are written in a more compact way as $\hat{\boldsymbol{\xi}}$, and the discrete nodal displacements \mathbf{u}_i

$$\mathbf{u}(\overset{\circ}{\mathbf{x}}, t) \simeq \mathbf{u}_e(\overset{\circ}{\mathbf{x}}(\hat{\boldsymbol{\xi}}), t) = \sum_{j=1}^8 N_j(\hat{\boldsymbol{\xi}}) \mathbf{u}_j(t). \quad (3.9)$$

Since in this thesis only 8-node-hexahedron elements are used the sum of Eq. (3.9) is directly written in the corresponding form and the shape functions can be written in the following form

$$N_i(\hat{\boldsymbol{\xi}}) = \frac{1}{8} (1 \pm \hat{\xi})(1 \pm \hat{\eta})(1 \pm \hat{\zeta}). \quad (3.10)$$

To arrive at the matrix notation of Eq. (3.7) the virtual displacements $\delta \mathbf{u}$ are factored out and, since the term is an arbitrarily trial function, the remainder has to vanish. Furthermore, the shape functions are arranged in the matrix \mathbf{N} and a matrix \mathbf{B} is introduced containing derivatives of the shape functions with respect to the physical coordinates which are calculated by the use of the inverse of the Jacobian matrix \mathbf{J} . So

$$\sum^{ne} \left[\int_{\mathcal{B}_e} \rho \mathbf{N}^T \mathbf{N} \mathbf{a} \, dv + \int_{\mathcal{B}_e} \mathbf{B}^T \boldsymbol{\sigma} \, dv - \int_{\mathcal{B}_e} \rho \mathbf{N}^T \mathbf{b} \, dv - \int_{\partial \mathcal{B}_{\sigma,e}} \mathbf{N}^T \mathbf{t} \, da \right] = \mathbf{0} \quad (3.11)$$

can be specified where \mathbf{a} contains the nodal accelerations, $\boldsymbol{\sigma}$ the stresses, \mathbf{b} the body loads and \mathbf{t} the surface loads. Finally to obtain a diagonal (lumped) mass matrix, the rows of the first term of Eq. (3.11) are summed, see [62]. This can be written in a more compact form as

$$\mathbf{M} \ddot{\mathbf{u}} + \mathbf{K} \mathbf{u} = \mathbf{f}^{\text{ext}} \quad \text{or} \quad \mathbf{M} \mathbf{a} + \mathbf{f}^{\text{int}} = \mathbf{f}^{\text{ext}} \quad (3.12)$$

where the first and second term of Eq. (3.12) represent the first and second term of Eq. (3.11) and the external loads and the body loads are combined in \mathbf{f}^{ext} . This form is frequently called semi-discrete due to the fact that it has been discretized in space but not yet in time, [13] what is discussed in Sec. 3.2.

The evaluation of the integrals over the element volume is realized by a Gaussian quadrature, for example the integration of an arbitrary function g is transferred to the natural coordinates of the element by the use of the shape functions (isoparametric concept) where the numerical integration is carried out

$$\int_{\hat{\mathcal{B}}_e} g \, dv \simeq \sum_{j=1}^n w_j \det \mathbf{J}(\hat{\boldsymbol{\xi}}_j) g(\hat{\boldsymbol{\xi}}_j) . \quad (3.13)$$

Here n is the number of integration points, w_j is the weighting factor and $\hat{\boldsymbol{\xi}}_j$ the location of each integration point. For the elements used within this thesis a one-point integration is carried out, i.e. $n = 1$, $w_1 = 8$ and $\hat{\boldsymbol{\xi}}_1 = (0, 0, 0)$. This so called reduced integration has on the one hand the advantage of computational efficiency but on the other hand the disadvantage of zero energy (hourglass) modes which need to be controlled, see [62] for further details.

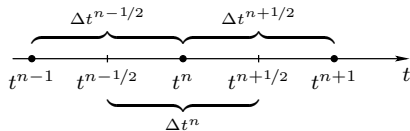


Figure 3.1: Notation used to explain time integration scheme; dots mark time steps, dashes mark midpoint steps

3.2 Explicit time integration

The choice of the time integration scheme mainly depends on the posed problem; generally it is distinguished between implicit and explicit methods, [169]. Implicit methods lead to the solution of a nonlinear equation system within every time step but have the possibility of relatively big time steps whereas explicit methods do not need to solve an equation system but have a limited time step size to keep the algorithm stable. Within this thesis fast processes are considered which include wave propagation and thus the explicit FE-code LsDyna has been chosen.

Since LsDyna uses the central difference method for time integration, a brief description is given here which is mainly based on [13]. It is assumed that the displacements \mathbf{u} , the velocities \mathbf{v} as well as the accelerations \mathbf{a} are known up to t^n , whereas the special situation at the start of the calculation is not considered, i.e. it is not reviewed how to get the algorithm started, for further details see [168]. With the notation explained in Fig. 3.1 the velocities $\mathbf{v}^{n+1/2}$ at time $t^{n+1/2}$ can be calculated as

$$\mathbf{v}^{n+1/2} = \frac{\mathbf{u}^{n+1} - \mathbf{u}^n}{\Delta t^{n+1/2}} \Leftrightarrow \mathbf{u}^{n+1} = \mathbf{u}^n + \Delta t^{n+1/2} \mathbf{v}^{n+1/2} \quad (3.14)$$

where the second term is rearranged to an integration expression. In the same manner the accelerations \mathbf{a}^n at time t^n and the corresponding integration expression can be written as

$$\mathbf{a}^n = \frac{\mathbf{v}^{n+1/2} - \mathbf{v}^{n-1/2}}{\Delta t^n} \Leftrightarrow \mathbf{v}^{n+1/2} = \mathbf{v}^{n-1/2} + \Delta t^n \mathbf{a}^n. \quad (3.15)$$

Now by the use of Eq. (3.12_b) and the notation $\mathbf{f} = \mathbf{f}^{\text{ext}} - \mathbf{f}^{\text{int}}$ Eq. (3.15_b) can be written as

$$\mathbf{v}^{n+1/2} = \mathbf{v}^{n-1/2} + \Delta t^n \mathbf{M}^{-1} \mathbf{f}^n \quad (3.16)$$

and directly be used to calculate $\mathbf{v}^{n+1/2}$, \mathbf{u}^{n+1} can be determined with Eq. (3.14_b). In continuation the external forces $\mathbf{f}^{\text{ext},n+1}$ are calculated and a loop over the elements is executed in which the internal force vector $\mathbf{f}_e^{\text{int},n+1}$ is calculated by the use of the constitutive equations. Thus after

1. Time update: $t^{n+1} = t^n + \Delta t^{n+1/2}$ and $t^{n+1/2} = t^n + 1/2\Delta t^{n+1/2}$
2. Calculation of midpoint velocities $\mathbf{v}^{n+1/2}$, Eq. (3.15_b)
3. Enforce velocity boundary conditions
4. Calculate displacements \mathbf{u}^{n+1} , Eq. (3.14_b)
5. Calculate external forces $\mathbf{f}^{\text{ext},n+1}$
6. Loop over elements
 - a) Extract nodal displacements and velocities
 - b) Loop over integration points
 - i. Calculate deformation gradient \mathbf{F} and strains $\boldsymbol{\varepsilon}$ at t^{n+1}
 - ii. Compute stresses $\boldsymbol{\sigma}^{n+1}$ by constitutive equation
 - iii. Calculate internal force vector per element $\mathbf{f}_e^{\text{int},n+1}$
 - c) Calculate external nodal forces $\mathbf{f}_e^{\text{ext},n+1}$
 - d) Compute element force vector $\mathbf{f}_e^{n+1} = \mathbf{f}_e^{\text{ext},n+1} - \mathbf{f}_e^{\text{int},n+1}$
 - e) Calculate new critical time step size of element
 - f) Subjoin \mathbf{f}_e^{n+1} to global \mathbf{f}^{n+1}
7. Determine new global time step size
8. Compute \mathbf{a}^{n+1} , Eq. (3.17)
9. Calculate velocities \mathbf{v}^{n+1} , Eq. (3.18) and check energy balance

Box 3.1: Flowchart of ongoing explicit time integration, based on [13]

the loop the new force vector \mathbf{f}^{n+1} can be assembled and Eq. (3.12) can be used to calculate

$$\mathbf{a}^{n+1} = \mathbf{M}^{-1} \mathbf{f}^{n+1}. \quad (3.17)$$

In order to be able to check the energy balance at the time steps the velocities are needed here and not only at the midpoints. Therefore, they are calculated by

$$\mathbf{v}^{n+1} = \mathbf{v}^{n+1/2} + \frac{1}{2} \Delta t^{n+1/2} \mathbf{a}^{n+1}. \quad (3.18)$$

A complete overview of one time step of an ongoing explicit time integration is given in Box 3.1.

As mentioned above, the time step of explicit methods is limited to keep the method stable. For the here used central difference method the time step is bounded by the highest frequency of any element, i.e. the 'smallest' element purports the time step size, see [62, 168]. To include any nonlinearities, LsDyna reduces this calculated time step by the factor 0.9 (default value) to

$$\Delta t = 0.9 \Delta t_{\min} = 0.9 \min_{ne} \left(\frac{l_e}{c_{\text{long}}} \right) \quad (3.19)$$

for 3-dimensional brick elements. Here l_e is the element length and c_{long} is the longitudinal or dilatational sound speed in continuous media defined through

$$l_e = \frac{V_e}{A_{e,\text{max}}} \quad \text{and} \quad c_{\text{long}} = \sqrt{\frac{K + 4/3G}{\rho}} \quad (3.20)$$

where V_e is the element volume and $A_{e,\text{max}}$ is the maximum lateral element surface.

3.3 LsDyna user materials

The LsDyna keyword user's manual [108] gives a relatively brief description of how to implement a material model. Besides the technical requirements such as the correct version of Fortran compiler and development tools, coding abilities are needed. This implementation was realized under Windows using the Intel Fortran Compiler and Microsoft Visual Studio whereas coding was done in Fortran77.

When the user-material subroutine is called, LsDyna provides several input parameters, amongst others the element type which is set to *solid* for 8-node solid elements and the current time as well as the time step size. Furthermore the current strain increment, the Cauchy stresses of the previous time step and the deformation gradient are available. If element erosion is used, an element failure flag can be provided and thus element erosion can be controlled from the user-material subroutine. In addition the material constants array is passed directly from the input deck and the history variables of the previous time step are passed on while its number has to be defined in the input deck.

To adopt the theory presented in Chap. 2 to LsDyna, a closer look at the input parameters to the user subroutine is necessary. LsDyna provides the coefficients F_{ij} of the deformation gradient with respect to an orthonormal basis of the initial configuration $\overset{\circ}{\mathcal{B}}$ which comprises that the metric coefficients $\overset{\circ}{G}^{ik} = I^{ik}$ are given while I^{ik} is the unity matrix. With the transposed coefficients F_{ki}^T of the deformation gradient, the coefficients of the metric can be calculated to $G_{kj} = F_{ki}^T F_{ij}$ which finally leads to the coefficients of the metric transformation tensor \mathbf{Q} posed in Eq. (2.1)

$$Q_{.j}^i = \overset{\circ}{G}^{ik} G_{kj} = I^{ik} G_{kj} \quad (3.21)$$

and thus is related to the kinematics presented in Sec. 2.1. In addition, it can be noted that the contravariant coefficients G^{jl} of the metric can

be obtained by inversion of the covariant coefficients G_{kj} . Furthermore, LsDyna provides the coefficients of the strain increment

$$\Delta D_{kl} = \Delta t^{n+1/2} D_{kl} \quad (3.22)$$

with respect to the orthonormal basis of the initial configuration. By the multiplication

$$F_{kl}^T \Delta D_{lm} F_{mj} = \frac{1}{2} \Delta G_{kj} \quad (3.23)$$

the coefficients of $1/2 \dot{G}_{kj}$ stated in Eq. (2.9) are obtained but integrated over the time increment. Finally this leads to the mixed-variant representation of the total strain increment

$$\Delta H_{.j}^i = \frac{1}{2} G^{ik} \Delta G_{kj} \quad (3.24)$$

as needed to calculate the elastic strain increment from this total strain increment and thus all necessary data is made available to the user-material subroutine.

After fulfilling all necessary operations within the subroutine, the data has to be prepared for output, mainly the stresses have to be transferred to Cauchy stresses with respect to a cartesian basis. By multiplying the internally used mixed-variant coefficients $T_{.k}^i$ with the contra-variant metric coefficients G^{kj} the coefficients S^{ij} of the second Piola-Kirchhoff stress tensor

$$S^{ij} = T_{.k}^i G^{kj} \quad (3.25)$$

are calculated. These can be transferred to the components of the Cauchy stress tensor by

$$\sigma_{ij} = \frac{1}{J} F_{ik} S^{kl} F_{lj}^T. \quad (3.26)$$

Furthermore, all history variables have to be updated what includes coefficients of: the stress tensor $\bar{\mathbf{T}}$ of the undamaged configuration, the stress tensor \mathbf{T} of the damaged configuration, the elastic transformation tensor \mathbf{Q}^{el} , the plastic transformation tensor $\bar{\mathbf{Q}}^{\text{pl}}$ as well as the damage tensor \mathbf{R}^* . Furthermore, as scalar variables are stored the yield c and the damage stress σ , the plastic γ and damage μ internal variable, the temperature as well as a plasticity and a damage flag.

4 Experimental aspects

This chapter gives an overview of the experiments generally used to determine the characteristics of ductile metals. Here the focus lies on the experiments used for the determination of the material properties of the aluminum alloy and the stainless steel considered within this thesis, while further hints are given to other experimental setups. Since the material behavior has to be characterized at different strain rates, temperatures and stress states, the subdivision of this chapter reflects these aspects.

4.1 Strain rate

On the one hand ductile metals frequently show differences in their behavior depending on the strain rate of the deformation process and on the other hand certain experimental facilities can only cover a restricted period of machine velocities which results in limited strain rates. Consequently, different experimental setups and specimen shapes have to be used to obtain results at a wide range of strain rates. Fig. 4.1 gives a schematic overview of the most commonly used experiments to characterize the behavior of ductile metals and a reference point of the strain rate they can cover.

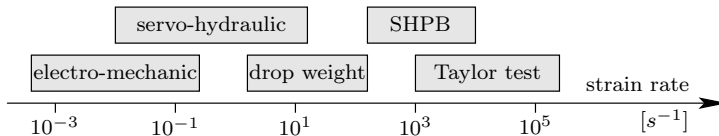


Figure 4.1: Typical strain rates of experiments [135]

Electro-mechanic testing machines (Fig. 4.2) which are well-established and standardized, are used to perform experiments at low strain rates where the machine velocity is limited to approx. 100 mm/min . At tension tests the deformation of the specimen is generally measured within a region by a strain gauge leading with the applied force to the standard load-strain curve. Furthermore, the lateral contraction can be measured with an additional instrument and thus the Poisson's ratio can be determined. Used for compression tests, i.e. upsetting tests, generally the machine displacement and the applied load are measured.

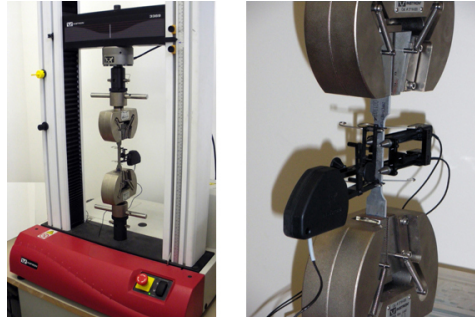


Figure 4.2: Electro-mechanic testing machine and measuring instruments at GMSIE lab, University of São Paulo (USP), Brazil

Servo-hydraulic machines, see for example Fig. 4.3, can be used in a more general way than electro-mechanical machines. For instance they can be used for cyclic tests as they are common for fatigue testing and they can be equipped to perform simultaneous rotary motions and therefore be used for tension-torsion testing. If the machine is equipped for special high speed tensile testing, it can reach machine velocities up to 1 m/s , also depending on the cross-section area of the specimen. Since generally relatively small specimens are used and the machine velocity is rather high, it is difficult to use strain gauges - as it is done in electro-mechanical machines and thus the machine displacement is recorded. Additional information can be retrieved by the use of digital image correlation (DIC). Here at first the contour deformation of notched specimens were monitored [59]. To date the surface area of the specimen is painted with a black and white pattern, Fig. 4.4, and during the experiment photos are taken which can be evaluated by a computer software and thus the deformation, i.e. the strains, of the specimen surface can be determined in two directions [111].

Another possibility to characterize the material behavior at medium strain rates, around 10^2 s^{-1} , is to perform experiments on drop machines [68]. During the experiment, a weight, equipped with a striker and guided by rails, is dropped from a certain height and impacts the reviewed component or specimen. Mainly two types of testing devices are distinguished: Massive drop towers with a height up to 20m and drop weights up to 200 kg and smaller drop darts with a height up to 5 m and drop weights up to 10 kg [135]. The main purpose of drop towers is component testing, whereas drop darts can be used for tests characterizing the material properties. Previous to the experiment a good estimation of the impact

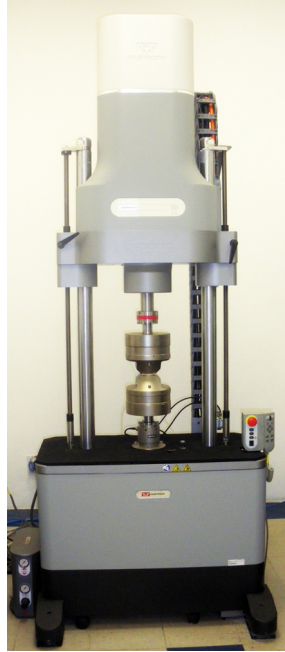


Figure 4.3: Servo-hydraulic machine at GMSIE lab, University of São Paulo (USP), Brazil

velocity can be made knowing the drop height, which leads in combination with the known weight to an estimation of the impact energy. By the installation of light barriers, the precise impact velocity can be determined, disregarding friction effects during the drop. Furthermore, by the use of a high speed camera the velocity evolution during the impact can be estimated by correlating between images to displacement. Further experimental results can be achieved by accelerometers, load cells and displacement/velocity transducers [135]. Drop machines are normally used to test two-dimensional specimens, i.e. plates, or laminar components but occasionally beams are tested [63, 5, 107]. In general, the load conditions of drop mass experiments are more complex, combined tension and bending, and the results, although a big variety can be provided, are rather defective [44].

The Split-Hopkinson-Pressure-Bar (SHPB) experiment is a standard test for the characterization of the material properties at high strain rates.

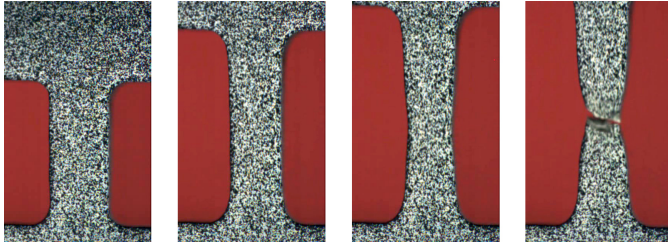


Figure 4.4: Series of specimen prepared for digital image correlation at GMSIE lab, University of São Paulo (USP), Brazil

The basic experimental setup goes back to Kolsky [82] who modified the experimental setups developed by John and Bertram Hopkinson, see [44]. Currently, the experimental setup for compression tests is largely established but the processing of the experimental data is still subject of discussion, see e.g. [135].

Fig. 4.5 gives a schematic sketch of the standard experimental setup used for compression tests, whereas Fig. 4.6 shows an in situ setup. The striker bar impacts the input bar with a certain velocity causing a nearly rectangular compression pulse. The generated compression wave propagates through the input bar while reaching the specimen which is clamped between input and output bar. The incident wave is partly reflected at the end of the input bar and partly transmitted through the specimen, which is deformed, to the output bar where it propagates. Finally the wave is passed on to the catcher bar and thus passes away from the actual experiment. The bars are generally made of material which behaves linear-elastic with a high yield strength so that the deformation within the bars remains elastic. The input and output bar are equipped with strain gauges which allow the measurement of the strain evolution over time within the bars.

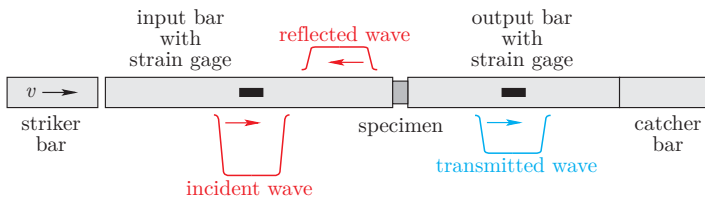


Figure 4.5: Schematic setup of Split-Hopkinson-Bar experiment



Figure 4.6: In situ experimental setup of Split-Hopkinson-Bar at GM-SIE lab, University of São Paulo (USP), Brazil; front: pressure bar with gas gun

To process the information of the Split-Hopkinson-Bar experiment, i.e. the stress-strain-curve of the specimen, generally a one-dimensional wave theory is used. Furthermore, it is assumed that the specimen is in a static equilibrium and the stresses on both ends coincide whereas this state is reached rather quickly for short specimens. Now the stresses can be obtained from the static equilibrium, while the strains of the incident, reflected and the transmitted wave are recorded within the bars, Young's modulus of the input and output bar and the cross section of the bars and of the specimen. In addition, the strains are obtained by integrating the strain rate which is known from the velocities of the bar ends, calculated from the strain time history of the bars, and the specimen length. For a detailed description of the procedure see [44]. Additional information about the progress of the experiment is gained by the use of a high speed camera.

Some additional remarks concerning the experiment can be made: The wave length is directly related to the striker length. If the striker and the input bar are of the same material, the wave length is twice the striker length. Besides, the stress or strain amplitude can be modified by the velocity of the striker and the strain rate is influenced by the geometry of the specimen and the amplitude of the stress wave. The evaluation of the experimental data is still subject of discussion, the main subjects being the dispersion of the wave and the strain recording by the strain gauges [44]. Furthermore the effects of bar misalignment on the experimental data is currently discussed, [81].

Furthermore, the Taylor test [155] where a small rod of metal impacts either a rigid wall (asymmetric) or - to minimize friction effects - another small rod of material (symmetric), can be used to reach strain rates up

to 10^5 s^{-1} in certain parts of the specimen. The impact velocity and the impact force of the specimen can be measured and in addition the experiment can be monitored by a high speed camera. Thus the Taylor test can not directly be used to identify the material parameters of a material but can be used in an inverse numerical technique by comparing numerical results with experimental data, see for example [74, 83].

At this point it is important to notice that while plastic deformations take place, the main part of the dissipated energy is converted to heating. Thus experimentally it is difficult to study only the effects of different strain rates since always heating does occur. Theoretically, two limit cases are of special interest: Firstly the process is sufficiently slow, heat can discharge and the temperature can be considered constant and the process can be considered as isothermal. Secondly, if the process is fast enough, the discharged heat is negligible and therefore the process can be considered as adiabatic.

4.2 Temperature

Ductile metals are characterized through softer behavior at elevated temperatures and through stiffer behavior at lower temperatures. This effect can be reviewed independently from the effects of strain rate by performing experiments at very low strain rates so that the process can be considered isothermal. Fig. 4.7 displays a standard environmental chamber which can be easily included in the experimental setup with an electro-mechanic testing machine. These standard cooling or heating chambers cover, depending on the design, temperatures in the range from -80°C to 600°C .



Figure 4.7: Environmental chamber at GMSIE lab, University of São Paulo (USP), Brazil

Besides these standard temperature chambers, several special solutions are reported. For instance Byun et al. [37] as well as Park et al. [132] used cooling devices with nitrogen which reached temperatures of -150°C and -200°C respectively whereas both studies consider stainless steel Inox 304L.

Although additional temperature increase, which is difficult to measure, occurs during Split-Hopkinson-Bar experiments, several experimental setups have been proposed to study the material behavior at high temperatures. Lennon and Ramesh [104] propose a method where the specimen is heated by an infra-red spot-heater, arriving to temperatures up to 800°C whereas Lee and Lin [93] used an in-situ induction coil to reach temperatures up to 1100°C . Lately Kajberg and Sundin [80] proposed a method also using an induction coil to extract material behavior during the production process reaching temperatures up to 1100°C and minimizing the heat transfer to the bars by bringing them into contact only very shortly before the experiment. Furthermore, Split-Hopkinson-Bar experiments can be performed at low temperatures; for instance Berkovic et al. [16] realized experiments with different ductile metals at temperatures down to -150°C by cooling the specimen down with liquid nitrogen before execution of the experiment.

4.3 Stress state

In addition, the material behaves different depending on the stress state and therefore, to characterize the material behavior entirely it needs to be tested under different and well defined stress states. Due to this fact, different specimen geometries are developed and currently great efforts are made to study the damage and fracture behavior under different loading conditions. It is not an easy task to estimate the stress state, i.e. the triaxiality and the Lode parameter, of the specimen part of interest previous to the experiment by theoretical considerations. And even after the execution the stress state is not directly accessible due to high plastic deformations, necking phenomena, rotations of part of the specimen or even dynamic effects such as wave propagation. To overcome this deficit, frequently numerical simulations of the experiments are performed which provide theoretical estimates of the stress state.

The standard material curves of the investigated materials are obtained by the use of the so-called dog-bone shaped specimen in a tension test. Depending on the design of the raw material, rod or sheet, it has a rectangular or circular cross section, see for instance Fig. 4.8. This type of specimen is characterized through a nearly uniform stress state in the central part of the specimen during the first range of the experiment. In

the zone of uniform stresses the elongation is measured by a strain gauge which leads with the measured load to the load-strain curve. Otherwise, compression or upsetting tests are used to characterize the material behavior under compression [9, 106]. Generally, it is very difficult to create pure compression stress state due to friction effects in the contact zone between specimen and machine, while buckling effects limit the length of the specimen.



Figure 4.8: Tension specimen dog-bone shaped, Inox 304L

Furthermore, notched tension specimens (Fig. 4.9) are designed to reach higher triaxialities within the notched region - the triaxiality increases with decreasing notch radius. Generally, the plastic deformations are concentrated within the notched part, but the strains are measured by a strain gauge including part of the un-notched specimen which leads to a smearing effect. Several authors have recently used notched tension specimens to study the damage and fracture behavior at elevated triaxialities, see for instance [21, 9, 54, 106, 30, 114]. In addition thicker metal sheets can be notched in thickness direction which can be seen as plane strain conditions [9].



Figure 4.9: Tension specimens, series with different notch radius 1.25, 2.5, 5.0, 10.0, 30.0 mm, Inox 304L

The design of specimens with a more shear-like failure at lower triaxialities, is not an easy task. Due to the ductility of the material, the

specimens show big rotations in the region where shear fracture is expected, which leads to a combined shear-tension-failure see for instance Fig. 4.10. Thus a notch in thickness direction is introduced to concentrate the deformations mainly in the shear region and therefore improving the behavior [31]. Focussing on the material behavior under shear load conditions, it can be tested with the Arcan specimen [8] which has been adapted lately for various stress states with a special testing device as butterfly-shaped specimen [119, 9, 114]. In addition torsion tests or combined torsion-tension tests can be performed [54].



Figure 4.10: Fractured shear specimen, aluminum thickness 3.19 mm

The standard specimen for Split-Hopkinson-Bar tests is a relatively thin disc which is tested under compression. In this context it has been proposed to use thin rings to reduce the effects of friction [6]. But, especially for material characterization of damage and fracture behavior, it is valuable to have results of tension tests available. Tension experiments can be performed with a modified experimental setup, in an indirect way or by the use of a special specimen shape. The experimental setup can be modified in such a way that a tension wave is generated in the input bar, see for instance [90, 172, 69], while then a relatively short tension specimen is used. Using an indirect form, a compression pulse is generated which is transferred to the output bar which is in direct contact where due to reflection on the free end a tension pulse is generated [64]. Further attempts were made by Mohr and Gary [117, 118], who designed a special specimen shape where the compression wave is converted to a tension wave within the specimen. Additional experiments with a specimen which fractures in a shear mode have been presented by Singh et al. [146]. The specimens proposed by Mohr and Gary [117, 118] as well as by Singh et al. [146] are reviewed in detail in Chap. 6.

5 Identification of material parameters

The determination of material constants and parameters of the continuum damage and fracture model as introduced Chap. 2 is crucial for its successful application. Especially it is difficult to identify the micromechanically motivated parameters of the damage condition, the damage rule and the parameters of the fracture criterion, due to the lack of experimental techniques on the micro scale. One possibility to overcome this deficit are micromechanical numerical studies, see for instance [30, 29] and [34, 35].

This chapter gives a detailed description of the determination of the material constants and parameters of stainless steel Inox 304L or X2CrNi18-9. Steel of this category is characterized through high ductility, i.e. high strains before fracture occurs as well as sensitivity to temperature effects and strain rate effects [132, 37]. Since these materials can be used in a extensive range of temperatures they are commonly used in several industrial applications such as liquid gas storages [132, 131] and heat exchangers [131].

With decreasing temperature, mainly lower than room temperature, Inox 304L shows increasing secondary phase transformation induced plasticity, see [133, 132, 37] whereas this effect is intensified with decreasing strain rate. The applications reviewed within this thesis are focused on temperatures above room temperature and on medium to high strain rates. Therefore, the effects of secondary hardening are not considered within this work.

Several material constants of Inox 304L are well known and therefore taken from literature. The initial density is chosen in accordance with [167] to $\rho_o = 7.9 \cdot 10^{-9} \text{ t/mm}^3$ and the coefficient of thermal expansion in accordance with [105, 167] to $\alpha_T = 17 \cdot 10^{-6} \text{ K}^{-1}$. In [105] a melting range of $1398 - 1420 \text{ }^\circ\text{C}$ is defined and thus leading to a melting temperature of $\theta_m = 1683 \text{ K}$. Furthermore, the volume specific heat capacity c_F , introduced in Eq. (2.40), can be calculated by multiplying the initial density ρ_o with the mass specific heat capacity c_m to

$$\begin{aligned} c_F &= \rho_o c_m \\ &= 7.9 \cdot 10^{-9} \text{ t/mm}^3 \cdot 4.5 \cdot 10^8 \text{ (N mm)/(t K)} \\ &= 3.555 \text{ N/(mm}^2 \text{ K)}. \end{aligned} \tag{5.1}$$

Here the value of the mass specific heat capacity is taken by averaging the

values given in [105] and [167]. The fraction of plastic work rate converted to heating ξ , see Eq. (2.43), is still subject of discussion in literature [140, 14, 32]. Especially a wide range of values for different materials and their dependencies on strain rate and strain state are discussed. For the present study $\xi = 0.8$ is chosen as a standard value.

The reference temperature at which the regular experiments have been performed in Brazil is room temperature, i.e. 25 °C leading to the reference temperature $\theta_o = 298$ K. The quasi-static reference experiment was realized with a machine velocity of 0.5 mm/min. The reduced part of the corresponding tension specimen has a length of 60 mm which leads to the reference plastic strain rate of

$$\dot{\gamma}_o = \sqrt{\frac{2}{3}} \frac{0.5}{60 \cdot 60} = 1.13 \cdot 10^{-4} \text{ s}^{-1}. \quad (5.2)$$

The determination of the damage reference strain rate is not possible with the available experimental data, therefore the value is adopted along with the reference plastic strain rate but neglecting the factor of $\sqrt{2/3}$ which leads to $\dot{\mu}_o = 1.39 \text{ s}^{-1}$.

Several data-sheets, e.g. [1, 2, 3], give information regarding the Poisson's ratio of Inox 304L with values from 0.27 to 0.3, consequently leading to the choice of $\nu = 0.29$. In combination with the experimentally determined Young's modulus $E = 190 \cdot 10^3 \text{ N/mm}^2$ and following [151] the shear modulus

$$\begin{aligned} G &= \frac{E}{2(1 + \nu)} = \frac{190000}{2(1 + 0.29)} \\ &= 73.64 \cdot 10^3 \text{ N/mm}^2 \end{aligned} \quad (5.3)$$

as well as the bulk modulus

$$\begin{aligned} K &= \frac{E}{3(1 - 2\nu)} = \frac{190000}{3(1 - 2 \cdot 0.29)} \\ &= 150.8 \cdot 10^3 \text{ N/mm}^2 \end{aligned} \quad (5.4)$$

can be calculated.

Stout and Follansbee [153] published experimental data of Inox 304L including results of quasi-static tension and compression tests of rod bars. This experimental data is used to determine the pressure coefficient a/c . Following the procedure described by Spitzig et al. [149, 150, 147], the coefficient was evaluated at different points of the experimental curve, see Fig. 5.1, and then chosen to $a/c = 55 \cdot 10^{-6} \text{ mm}^2/\text{N}$. Thus Spitzig et al.'s observation [147] could be confirmed that the pressure coefficient is constant, while the detected value is about 2.5 times bigger than the one

observed for different iron-based materials [147].

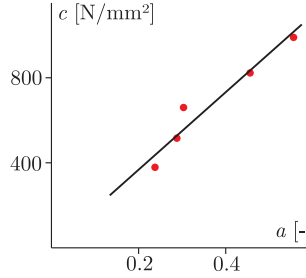


Figure 5.1: Determination of pressure coefficient, data points taken from [153], linear fit with $a/c = 55 \cdot 10^{-6} \text{ mm}^2/\text{N}$

With the constant pressure coefficient a/c and remodeling Eq. (2.63) to

$$c = \frac{\sqrt{J_2}}{1 - \frac{a}{c} \bar{I}_1} \quad (5.5)$$

the experimental curve can be shifted, i.e. the true stress T_{11} of a tension experiment has to be multiplied by the factor $(1 - a/cT)^{-1}$ which reflects the influence of \bar{I}_1 . Fig. 5.2 displays two experimental curves of experiments with two different machine velocities. As mentioned before, the effect of secondary hardening, as indicated in the experimental curve with machine velocity of $0.5 \text{ mm}/\text{min}$, is not considered within this thesis. The theoretical curve shown in Fig. 5.2 is the corresponding curve fit with respect to Eq. (2.65) hence for the non-rate and non-temperature dependence case where the initial static yield stress $\tilde{\sigma}_0 = 380 \text{ N}/\text{mm}^2$, the hardening parameter $H_o = 2800 \text{ N}/\text{mm}^2$ and hardening exponent $n = 0.6$ are chosen.

To determine the parameters introduced in Eq. (2.67), which describe the temperature dependence of the plastic hardening behavior, tension tests at 200°C have been performed. Fig. 5.3 displays experimental results of experiments at room temperature as well as at 200°C whereas the experimental curve is displayed until secondary hardening effects appear at room temperature. The corresponding parameters of Eq. (2.67) have been identified $b = 4.0$ and $q = 1.4$.

Furthermore, experiments at different strain rates have been performed to determine the material parameters of Eq. (2.66). The velocities of the electro-mechanic testing machine reach from $0.5 \text{ mm}/\text{min}$ to $500 \text{ mm}/\text{min}$ what leads to plastic strain rates of $\dot{\gamma} = 1.13 \cdot 10^{-4}$ to 10^{-1} s^{-1} . First

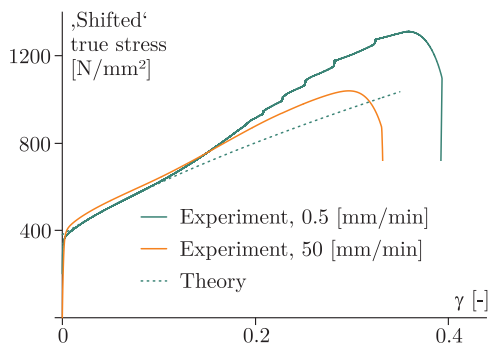


Figure 5.2: Determination of plastic hardening parameters; curve with machine velocity of 0.5 mm/min indicates slight secondary hardening due to very low strain rate

experiments on a servohydraulic testing machine have been performed which had a plastic strain rate of $\dot{\gamma} = 12.2 \text{ s}^{-1}$ and tests in the Split-Hopkinson-Bar having a plastic strain rate of $\dot{\gamma} = 1900 \text{ s}^{-1}$. It is important to notice that experiments at high strain rates generally show remarkable temperature increase, i.e. in general, strain rate effects can not be reviewed independently from temperature effects. As mentioned before, it is difficult to obtain the temperature evolution of a specimen during the experiments, specially since heat flux takes place. To overcome these difficulties, within this thesis the assumptions are made that the rate effects can be reviewed independently from temperature effects and that due to extremely fast processes the thermal process can be considered as adiabatic. Fig. 5.4 displays the experimental curves and the corresponding numerical fit with parameters $d = 0.025$ and $m = 0.195$. In addition, it can be noted that currently there is no experimental information to determine the parameters of Eq. (2.82) which characterizes the damage strain rate dependence. One possibility to overcome this lack of information might be a detailed micromechanical study of pore cluster under different strain rates, hence the corresponding parameters are chosen to be $h = 0.025$ and $r = 0.195$.

The material parameters $\eta_1 \dots \eta_4$ introduced in Eq. (2.74) describe the influence of damage on the elastic properties which can be clearly seen in Eq. (2.75). Spitzig et al. [148] analyzed the change of the elastic properties E , G , K and ν vs. porosity at specimens made from iron compacts. These experimental results have been used by Brünig [26] to

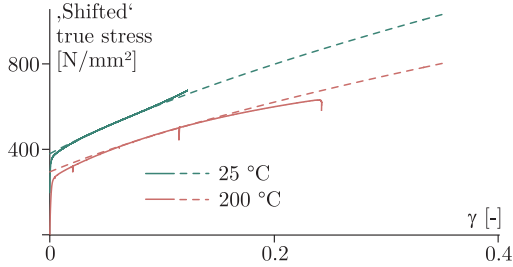


Figure 5.3: Determination of plastic temperature dependence parameter, continuous lines experimental data and dotted lines corresponding theoretical fit

determine the following parameters for the isotropic case

$$\begin{aligned} \eta_1 &= -117.5 \cdot 10^3 \text{ N/mm}^2, & \eta_2 &= -95.0 \cdot 10^3 \text{ N/mm}^2, \\ \eta_3 &= -190.0 \cdot 10^3 \text{ N/mm}^2, & \eta_4 &= -255.0 \cdot 10^3 \text{ N/mm}^2. \end{aligned} \quad (5.6)$$

For the Inco 304L steel under consideration, currently no such experiments are available and therefore, the parameters determined by Brünig [26] are used. In the future it will be possible to use a procedure based on numerical simulations on the micro scale in order to avoid the rather costly experimental procedure, which in addition might be difficult to realize for several materials.

Fig. 2.2 illustrates the different damage mechanisms with respect to triaxiality. In accordance with [31] the corresponding transmission parameters are chosen to $\eta_c = -1/3$ and $\eta_t = 1/\sqrt{3}$. Furthermore the fracture condition given in Eqs. (2.89, 2.90) is triaxiality dependent and the transmission parameter is chosen in accordance with Brünig and Gerke [33] to $\eta_f = \eta_t$.

To study the damage and fracture process experimentally is a very difficult task, since all processes take place at a micro level. Therefore, the identification of material parameters of the damage softening law as stated in Eq. 2.81 and of the fracture condition presented in Eq. 2.89 based on experimental data is currently not possible. To overcome this deficit the following inverse procedure is proposed: Firstly the parameters of the damage softening law are identified by simulations without temperature and strain rate dependence so that reasonable damage evolution occurs. Secondly the fracture condition parameters are calibrated to achieve reasonable fracture behavior under different stress states. Finally, the identified parameters are confirmed by performing simulations including rate and temperature dependence and comparing the results

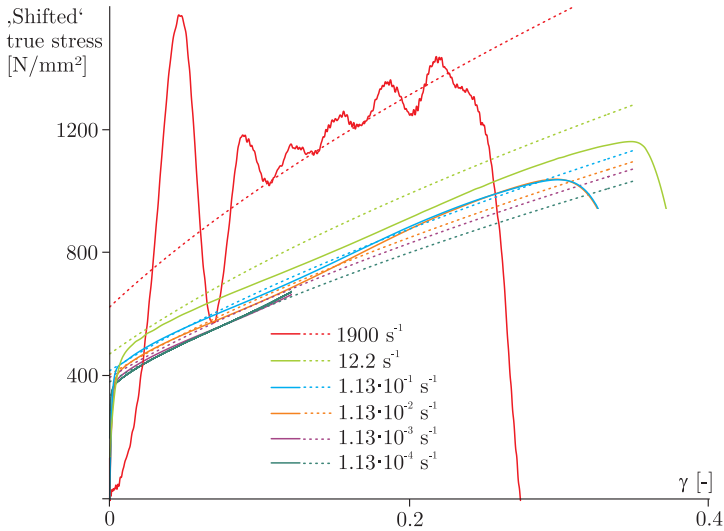


Figure 5.4: Determination of plastic strain rate dependence parameter, continuous lines experimental data and dotted lines corresponding theoretical fit

with experimental data. This procedure was used to identify the material parameters of Inox 304L to $\mu_e = 1.0$, $\mu_o = 0.05$ and $\mu_f = 0.1$ and results of the corresponding simulations are given in Chap. 6.1.

All material constants and parameters discussed above in detail are summarized in Tab. 5.1 and Tab. 5.2. In addition the material characteristics of the aluminum alloy have been listed. These have been discussed in detail in [31, 30, 29, 33].

At this point it is important to notice that both materials show significant differences in its behavior:

- The stainless steel Inox 304L is characterized through extremely high ductility, whereas the aluminum alloy shows moderate ductile behavior.
- Inox 304L shows a remarkable bigger influence in its behavior with respect to strain rate and temperature than the alluminum alloy.

Table 5.1: Summary of material constants and elastic-plastic parameters

Symbol	Unit	Description	Value aluminum 6.35 mm	Value Inox 304L
ρ_o	t/mm ³	Initial density	$2.7 \cdot 10^{-9}$	$7.9 \cdot 10^{-9}$
c_F	N/(mm ² K)	Volume specific heat capacity	2.4021	3.555
α_T	K ⁻¹	Coefficient of thermal expansion	10^{-5}	$17 \cdot 10^{-6}$
θ_m	K	Melting temperature	775	1680
θ_o	K	Experimental reference temperature	293	298
ξ	[-]	Fraction of plastic work rate converted to heating	0.7 – 0.8	0.8
G	N/mm ²	Shear modulus	$28.8 \cdot 10^3$	$73.64 \cdot 10^3$
K	N/mm ²	Bulk modulus	$62.5 \cdot 10^3$	$150.8 \cdot 10^3$
$\dot{\gamma}_o$	s ⁻¹	Reference plastic strain rate	$8.17 \cdot 10^{-4}$	$1.13 \cdot 10^{-4}$
a/c	mm ² /N	Pressure coefficient	$180 \cdot 10^{-6}$	$55 \cdot 10^{-6}$
$\tilde{\sigma}_o$	N/mm ²	Initial static yield stress	250	380
H_o	N/mm ²	Hardening parameter	3125	2800
n	[-]	Hardening exponent	0.135	0.6
d	[-]	Plastic strain rate parameter	0.595	0.025
m	[-]	Plastic strain rate exponent	$6.53 \cdot 10^{-6}$	0.195
b	[-]	Plastic temperature parameter	3.85	4
q	[-]	Plastic temperature exponent	1.9	1.4

Table 5.2: Summary of damage and fracture material parameters

Symbol	Unit	Description	Value aluminum 6.35 mm	Value Inox 304L
f_o	$[-]$	Initial porosity	0.0	0.0
$\tilde{\sigma}_o$	N/mm^2	Initial static damage stress	370	1000
$\dot{\mu}_o$	s^{-1}	Reference damage strain rate	10^{-3}	$1.39 \cdot 10^{-4}$
h	$[-]$	Damage strain rate parameter	0.595	0.025
r	$[-]$	Damage strain rate exponent	$6.53 \cdot 10^{-6}$	0.195
η_1	N/mm^2	Elastic damage modulus 1	$-30 \cdot 10^3$	$-117.5 \cdot 10^3$
η_2	N/mm^2	Elastic damage modulus 2	$-20 \cdot 10^3$	$-95 \cdot 10^3$
η_3	N/mm^2	Elastic damage modulus 3	$-25 \cdot 10^3$	$-190 \cdot 10^3$
η_4	N/mm^2	Elastic damage modulus 4	$-20 \cdot 10^3$	$-255 \cdot 10^3$
η_c	$[-]$	Damage cut of triaxiality	$-1/3$	$-1/3$
η_t	$[-]$	Damage mode triaxiality	$1/\sqrt{3}$	$1/\sqrt{3}$
μ_e	$[-]$	Damage law parameter	0.2	1.0
η_f	$[-]$	Fracture transmission triaxiality	$1/\sqrt{3}$	$1/\sqrt{3}$
μ_f	$[-]$	Fracture; critical damage tension	0.16	0.10
μ_o	$[-]$	Fracture; critical damage shear	0.02	0.05

6 Numerical examples

All numerical simulations presented in this chapter have been performed with the commercial finite element program LsDyna which was augmented by an user-defined material subroutine. Most of the meshing has been realized with Ansys Classic by use of the Ansys parametric design language (APDL) which allows the parametrization of the finite element model. For further preprocessing LsPrePost and Altair HyperMesh have been used while the postprocessing has been carried out with LsPrePost and Altair HyperView. Additional graphic processing has been realized with standard office software such as Microsoft Excel, CorelDraw for vector plots and Photoshop for pixel data.

6.1 Finite element modeling

This section covers several aspects concerning the finite element modeling of Split-Hopkinson-Bar experiments. One important aspect of the experimental setup is that a rather small specimen is located between comparatively long bars. Furthermore, to achieve sufficiently accurate results, especially regarding developing damage and fracture, a rather fine mesh has to be used in these parts of the model, but for computational efficiency these fine meshes can not be used for the complete model, which leads to mesh refinement issues. During these numerical studies it is important to keep the real experimental setup in mind. All Split-Hopkinson-Bar experiments reviewed in this work were realized at GMSIE lab at the University of São Paulo (USP). The bars are supported by Teflon sliding contact bearing allowing an almost frictionless movement of the bars that is not considered in the finite element modeling. The striker bar is accelerated by a gas gun but currently there is no possibility to measure the striker velocity before impact. All bars have a diameter of 25.0 mm whereas the striker has a length from 300 or 500 mm and the input and output bars have a length of 1400 mm for aluminum and 2007 mm for steel. Both, input and output bar, are equipped with one strain gauge on the surface at their centers in longitudinal direction.

The numerically predicted strains within the bars have to be compared with those reported by the strain gauges in the corresponding experiment and thus have to be extracted from the numerical simulation. The bars are made of a material with high yield stress and so their behavior during the

experiment is elastic, which leads to the choice of an elastic material law for the numerical simulations while in this case, *Mat_Elastic* in LsDyna was chosen. The strain in bar length direction has been extracted by reporting the stress of one solid element at the strain gauge location on the outside of the bar and then calculating the strain by the use of the linear elastic material law.

In this context, the discretization of the bars is of special interest where a choice of a sufficiently fine mesh at acceptable numerical cost has to be performed. Hence a study with different meshes has been realized and the obtained results as well as the computational costs are reported. To this purpose a steel striker of 300 mm impacts an input steel bar of 2007 mm with an velocity of 20 m/s while the strains at the strain gauge location of the bar are compared. Tab. 6.1 gives an overview of the approximated element sizes, the total of elements and the cpu time as well as the relative cpu time referred to the later chosen mesh. Comparing the results in Fig. 6.1, one can notice that a coarser mesh filters the high dispersion frequencies, but still the meshes with element size 1.0/1.0, 2.0/2.0 and 2.0/10.0 show comparable results while the very coarse mesh is out of scope. In this situation it is important to notice that the length of the strain gauge plays an important role with respect to the reported strains while longer strain gauges smoothen the curve or filter high frequencies [79]. Thus it is assumed that the mesh 2.0/10.0, see Fig. 6.2, provides sufficiently accurate results by relatively low computational cost so that this mesh will be used for all simulations. Actually, the mesh is coarsen in length direction in two steps, finally reaching an aspect ratio of 1:5 which leads to a total element number of 3,456 for the striker and of 21,248 for the input bar.

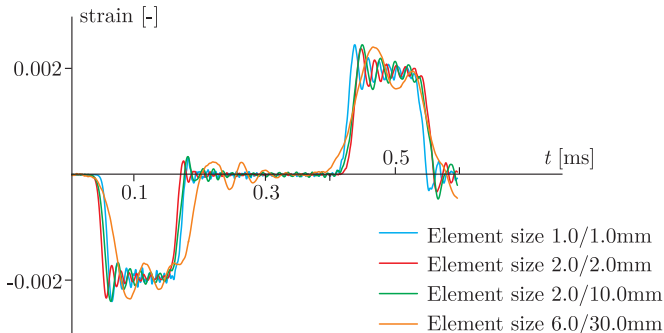
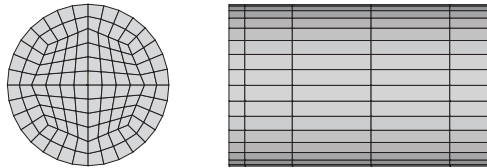


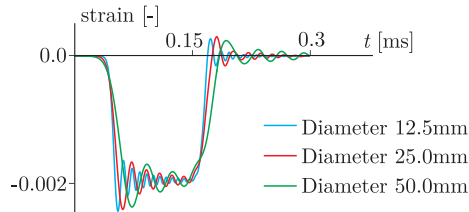
Figure 6.1: Strains of input bar with respect to different mesh sizes

Table 6.1: Tested mesh size bars

Approx. element size cross section [mm]	Approx. element size length direction [mm]	Total elements	cpu time [s]	Relative cpu time
1.0	1.0	962,048	9,523	89
2.0	2.0	120,320	594	5.6
2.0	10.0	24,704	107	1.0
6.0	30.0	624	2	0.02

**Figure 6.2:** Mesh of bars; left: cross-sectional area, right: mesh coarsening in longitudinal direction

Generally, the results of Split-Hopkinson-Bar experiments are evaluated applying a one-dimensional wave theory [44]. Dispersion effects, i.e. the effects of wave propagation in thickness direction on the longitudinal wave, are known to be more significant with increasing bar diameter. Here this effect is reviewed by a numerical study including half and double bar diameter. Fig. 6.3 displays the results for a bar length of 2007 mm impacted by a 300 mm striker with 20 m/s . Here it can be noticed that the dispersion effects due to bar diameter can be numerically predicted. From an experimental point of view it is important to notice that similar dispersion effects in an experiment can be reported only if a very good bar alignment is achieved and thus these effects can be seen as a measure for the quality of the bar alignment.

**Figure 6.3:** Strains of input bar with respect to different diameter

Evaluating the experimental results of Split-Hopkinson-Bar experiments it is assumed that the specimen is in static equilibrium which is almost instantaneously reached whereas generally thin disc specimens are used. This assumption is numerically reviewed by the choice of a specimen that is 5 mm thick and has a diameter of 15 mm; Fig. 6.4 displays the meshed specimen. The input and output bars were modeled in steel and the input bar was impacted by a striker of 300 mm with a velocity of 20 m/s whereas the disc was modeled with the material parameters of Inox 304L. Fig. 6.5 shows the forces between input bar and specimen as well as between specimen and output bar, as reported during the simulation. In this case the static equilibrium is reached almost instantaneously, only during the period of almost constant stresses slight differences can be noticed which could have their origin in dispersion effects of the specimen itself.

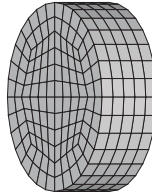


Figure 6.4: Mesh of disc specimen, total of 640 elements

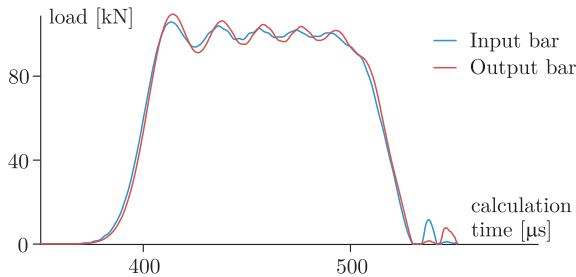


Figure 6.5: Forces during deformation process of a disc specimen

Furthermore, the strains of the steel input bar of 2007 mm length and of the aluminum output bar of 1400 mm length are displayed in Fig. 6.6. The simulation results of this commonly used experiment show remarkable decrease of the amplitude between incoming and reflected wave of the input bar as well as a major wave caused in the output bar.

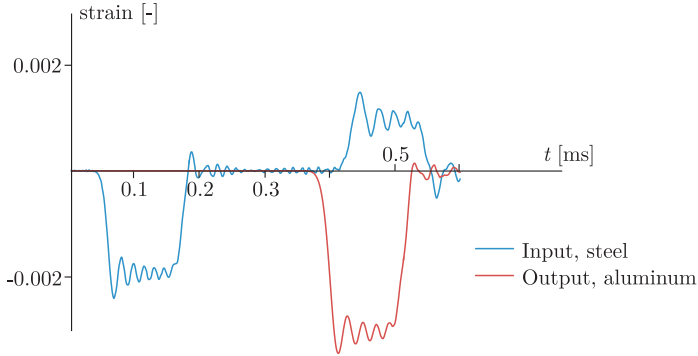


Figure 6.6: Strains of input and output bar, disc specimen

6.2 Reduced M-Shape

Mohr and Gary [117, 118] proposed a new M-Shaped specimen, Fig. 6.7_a, which can be used in a Split-Hopkinson-Pressure-Bar apparatus to perform tensile experiments. This specimen is especially designed to transform compressive loading conditions into tensile loading in its critical part. Mohr and Gary [117, 118] identified their static material parameters using a specimen of 3.5 mm thickness. Then they performed dynamic experiments with thicknesses being a multiple of 3.5 mm. To study the pure tension behavior of the central part of the specimen, numerical studies were realized with this part, indicated in Fig. 6.7_a in red, whereas the dimensions are given in the three central drawings of Fig. 6.7.

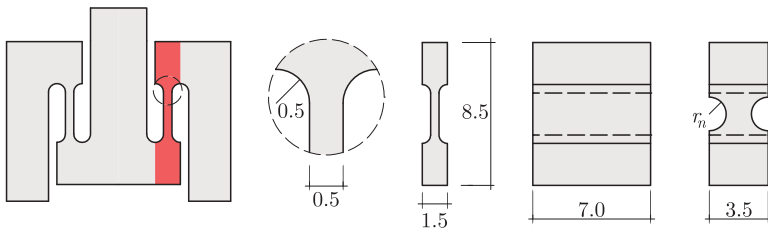


Figure 6.7: M-Shape specimen by Mohr and Gary [118], reduced (in red) and notched for numerical studies; all measures in [mm]

Fig. 6.8 gives an impression of the mesh of the reduced M-Shape specimen although the illustrated mesh is coarser than the one used for the

simulations with a total of 246,528 elements where the thin part of the specimen has 12 elements over the width and 72 elements in thickness. Following the ideas of Børvik et al. [22] who used for similar studies a dynamic surface impulse which is related to those occurring in Split-Hopkinson-Bar experiments, here a tension pulse as shown in Fig. 6.9 on the face surface has been applied while the other end is fixed. Here it is important to notice that these relatively simple boundary conditions do not reflect any bending phenomena occurring in the complete specimen and the applied impulse is smoother than the one expected in this part of the complete specimen. These numerical studies have been performed for the aluminum alloy using the corresponding material parameter given in Tabs. 5.1 and 5.2.

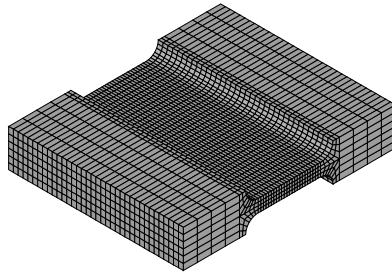


Figure 6.8: Mesh of reduced M-Shape

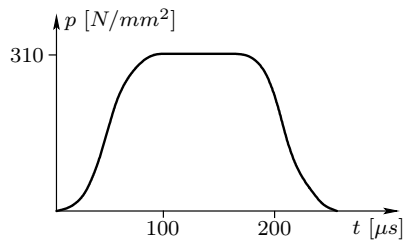


Figure 6.9: Applied pressure for numerical studies of reduced M-Shape specimen

With the presented material model, the complete deformation process, i.e. elastic, elastic-plastic, elastic-plastic-damaged and finally fracture behavior, can be described. Fig. 6.10 shows the evolution of the internal

damage variable μ for rate and temperature dependent material behavior. Firstly, damage evolves at the complete thinner part of the specimen over a quite long period of time, forming maxima at the center as well as on the edge close to the thicker part of the specimen, Fig. 6.10_b. It can be seen, fracture firstly occurs almost simultaneously and evolves from the center horizontally towards the outside and from the edge horizontally towards the center. This causes major shear behavior with low positive triaxialities between the advancing cracks where the internal damage variable already reaches a remarkable value of approximately 4%. In combination with the triaxiality dependence of the fracture criterion, this leads to the shown shear fracture while Fig. 6.11 gives a detailed impression of the fracture surface.

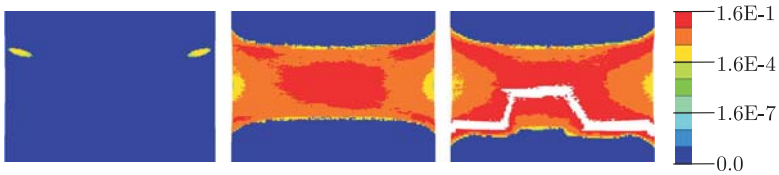


Figure 6.10: Evolution of internal damage variable μ and fracture process, pre-study with thickness 7.0 mm

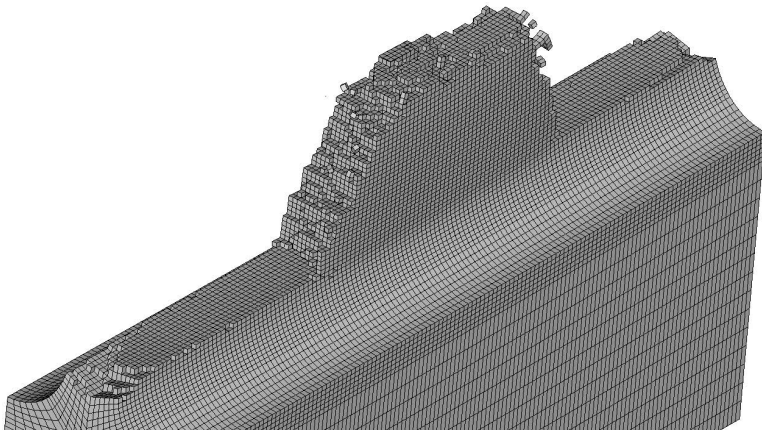


Figure 6.11: Fracture surface of un-notched aluminum specimen, pre-study with thickness 7.0 mm

Motivated by Hopperstad et al. [69] and the corresponding numerical simulations by Børvik et al. [22] who performed high-speed tension experiments with specimens with different notch radii using a special Split-Hopkinson-Bar setup, a series of numerical studies with differently notched flat specimens is carried out. In this context, the systematic of Mohr and Gary [117, 118] is maintained and a specimen width of 3.5 mm is used whereas different notch radii $r_n = 0.25, 0.5, 0.75, 1.0$ mm are tested, see last drawing of Fig. 6.7, maintaining the central part of the specimen at a constant width of 1.75 mm. Furthermore, Fig. 6.12 illustrates the mesh of $1/8^{\text{th}}$ of the specimen whereas all simulations were performed without symmetry conditions.

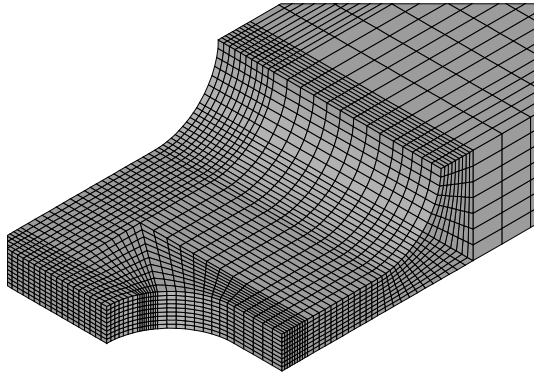


Figure 6.12: Mesh of reduced M-Shape with notch

In Fig. 6.13, a remarkable concentration of damage can be observed near the notch tips of small radius whereas large damage zones are characteristic for larger notch radii. The final fracture line is straight and, compared with that one of the un-notched specimen (Fig 6.11), completely different. Thus different failure modes are numerically predicted which allow the analysis of various stress triaxialities. Hence, a series of experiments with variously notched specimens could give new insights in damage and failure mechanisms at different triaxialities under dynamic loading conditions.

At this point it is important to notice that the central part of the M-Shape specimen has certain restrictions to its geometry which have to be reflected in the design of a notched specimen. The length of the central part has to be kept as short as possible in order to reduce the distance the incoming wave has to cover. Consequently the width of a notched specimen is restricted, especially if different notch radii ought to be used

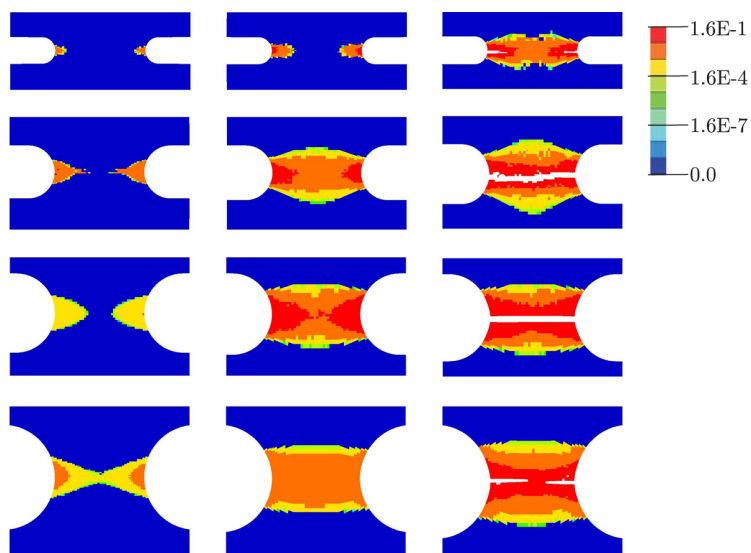


Figure 6.13: Evolution of internal damage variable μ and fracture of reduced M-Shape with notch, time between images $3.5 \mu\text{s}$

and thus the amplitude of the transmitted wave to the output bar is limited. Therefore, it has to be reviewed in detail if this wave can be evaluated from an experimental point of view.

6.3 Split-Hopkinson-Bar tests: Rings

Currently ring-shaped specimens are more frequently used, for instance Alves et al. [6] emphasizes the advantages of ring specimens due to the reduced influence of friction which allows the reduction of lubricants. This leads to advantages especially for experiments performed at low and high temperatures. In addition, specimens can be easily fabricated if the raw structures are thin walled tubes or sheets.

In this context, aluminum rings with an outer diameter of 20.0 mm, wall thickness of 1.0 mm and height of 6.35 mm have been tested, noting that the geometric relations do not fulfill the requirements proposed by Alves et al. [6] to extract material curves, i.e. the specimens are slimmer and warpage can occur.

Fig. 6.14 gives an impression of the deformation behavior during the Split-Hopkinson-Bar experiment while aluminum bars with a length of 1400 mm have been used. The pictures were taken by a high speed camera with 15000 fps (frames per second) and give an impression of the deformation behavior during the 1st wave passage. The specimen shows displacements at its center in radial direction which lead to remarkable tension on its outside. In the 3rd slide first signs of fracture can be seen in this region and in the 4th slide remarkable fracture is visible. Furthermore remarkable temperature increase occurred which did not allow to touch the specimen directly after the experiment noting that almost the whole specimen undergoes major plastic deformations which lead to this remarkable temperature increase.

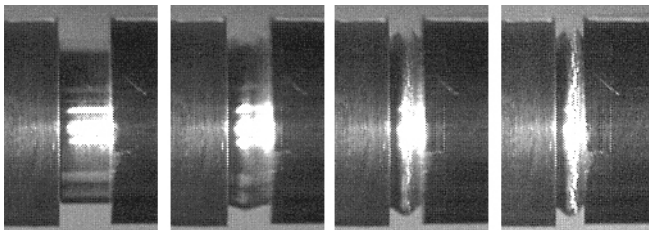


Figure 6.14: Deformation of aluminum rings during Split-Hopkinson-Bar experiment; time between images $66.6 \mu\text{s}$

Fig. 6.15 displays the mesh used for the numerical study. Here it can be noticed that 12 elements have been used in wall thickness direction which can reflect the bending in this direction. Furthermore, the friction coefficient between the bars and the specimen is set to 0.01 which leads to very similar results compared with the experimental behavior.

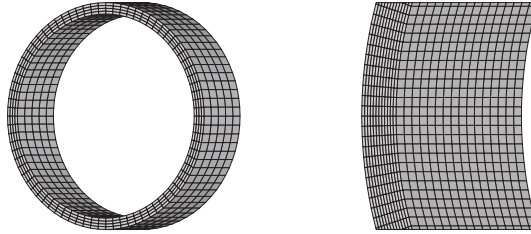


Figure 6.15: Mesh of ring specimen, left: complete specimen with coarser mesh for illustration purposes; right: cut-out; total of 46,080 elements

To study the first part of the deformation process, elastic-plastic simulations with rate and temperature dependence are realized, see also [58, 56]. These simulation can not cover the last part of the deformation process, but they give an insight into the first elastic-plastic part of the deformation process. Fig. 6.16 displays the temperature increase during this deformation process whereas for these simulations the rate of plastic work converted to heating is set to $\xi = 0.7$. In this part of the deformation process large plastic deformations, and thus heating, take place in the contact zones of the specimen with the bars as well as in the inner part of the center where compression is predominant. On the outside of the central part first a compression dominated stress state takes place at the beginning, which changes with ongoing bending to a biaxial tension state.

6.4 Split-Hopkinson-Bar tests: M-Shape

The geometry of the M-Shaped specimen presented by Mohr and Gary [117, 118] has to be adopted depending on the ductility, i.e. the strain to fracture and the diameter of the bars. Fig. 6.17 gives a detailed sketch of the geometries used for the aluminum alloy and the stainless steel Inox 304L which have been developed and tested at GMSIE lab, University of São Paulo (USP), Brazil. Furthermore, Fig. 6.18 gives an impression of the specimen (Inox 304L) before and after the experiment.

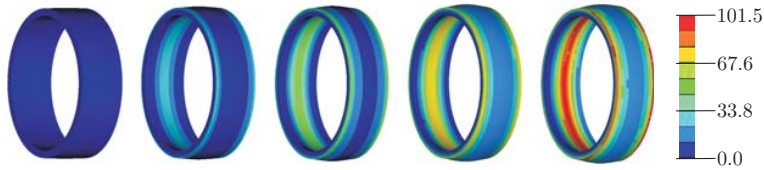


Figure 6.16: Simulation of temperature increase of aluminum rings during Split-Hopkinson-Bar experiment, time between images $4 \mu\text{s}$

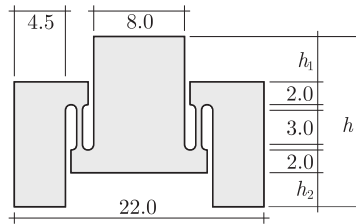


Figure 6.17: Geometry of M-Shape specimen; all measures in [mm]; for aluminum alloy $h = 11.0 \text{ mm}$, $h_1 = 2.0 \text{ mm}$, $h_2 = 1.0 \text{ mm}$ and thickness 6.35 mm ; for Inox 304L $h = 15.0 \text{ mm}$, $h_1 = 4.0 \text{ mm}$, $h_2 = 3.0 \text{ mm}$ and thickness 3.0 mm ; all inner radii 0.5 mm ; width of tension part 0.5 mm

The specimen is located in such a way that the middle part is in contact with the input bar and the divided part is in contact with the output bar. Used in this form, i.e. without any support, the divided part of the specimen will move during the experiment towards the outside of the bars and significant bending will occur also causing problems in the contact zone with the output bar. To avoid these difficulties, Mohr and Gary [117, 118] proposed the use of spacers between the central part and output side and a further support of the divided part. This was realized in the used experimental setup through two L-shaped spacers and a cap with a rectangular slot for the specimen as base support on the side of the output bar. Although the shape of these additional parts is optimized to simplify the execution of the experiment, it is still difficult to locate all parts properly before the experiment is performed.

Fig. 6.19 gives an impression of the deformation behavior of an Inox 304L specimen during the experiment. On the 1st picture the specimen is still at rest whereas in the 2nd the deformation is progressing. In

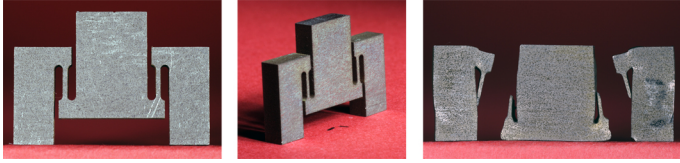


Figure 6.18: M-Shape specimen Inco 304L, before and after experiment

the next picture it is more likely that fracture already occurred and in the 4th picture the specimen is clearly fractured in both tension parts. It can be nicely observed that both sides of the specimen deform first uniformly although final fracture is more likely not to occur at the same time. The spacers and the cap avoid major bending in the thin tension part but its occurrence is not completely prevented. The major inelastic deformations that can be seen in Fig. 6.18c are not generated in the first wave transmission, they develop in subsequent wave transmissions when the specimen occurs to be clamped between input and output bar. However in this context only the first wave propagation is considered since it reflects the material response until fracture of the thin part.

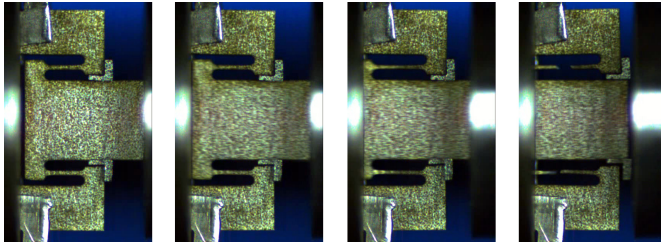


Figure 6.19: Deformation and fracture of Inco 304L M-Shape specimen during Split-Hopkinson-Bar experiment, time between images $100 \mu\text{s}$

For the M-Shape experiments with Inco 304L a steel striker bar (500 mm), a steel input bar (2007 mm) and an aluminum output bar (1400 mm) have been used. Due to the small cross-section of the specimen's tension part, the amplitude of the transmitted wave is small compared with the incident wave, so the measurement of the transmitted wave occurs to be difficult. By using an aluminum output bar where the Young's modulus is about $\frac{1}{3}$ smaller compared to steel, the strains are about factor 3 bigger and thus are easier to measure. Fig. 6.20 gives an example of the waves

reported by the strain gauges during the M-Shape experiment with Inox 304L. The dispersion of the bar can be clearly noted as well as the difference in amplitude between the input and output bar. Furthermore, it can be clearly seen that the specimen fractured during the influence of the first wave. Also the amplitude of the reflected wave is almost as big as the incident wave, i.e. only a small part is transmitted through the specimen and the wave is reflected several times within the input bar which causes the major inelastic deformations of the specimen in the subsequent wave transmissions, Fig. 6.18_c. Hence the wave transmission behavior of the proposed M-Shape specimen appears to be different to that of the disc specimen (Fig. 6.5), especially the amplitude of the transmitted wave has a different magnitude. In addition it can be mentioned that for experiments with the aluminum alloy an aluminum striker bar (300 mm), an aluminum input bar (1400 mm) and an aluminum output bar (1400 mm) have been used.

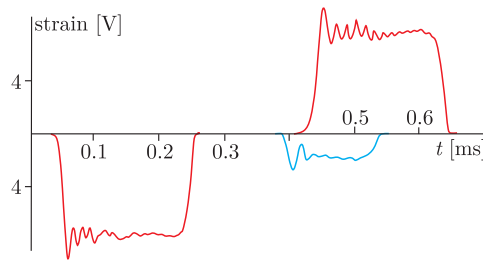


Figure 6.20: Signal of M-Shape experiment (Inox 304L) in Split-Hopkinson-Bar, red input (steel) and blue output bar (aluminum), ordinate in V which can be seen as a measure of strain; data processed for more legible diagram

Figs. 6.21 and 6.22 show finally fractured specimens. While the fracture of the aluminum specimens of 6.35 mm thickness has an inclined development from the outside and at the center it is perpendicular to the edge, the fracture of the Inox 304L specimens of 3.0 mm thickness is completely perpendicular to the edge with small kinks. In both cases the crack is inclined to the main crack direction which can be a result of the high strain rates as reported by [139]. Here it is important to notice that the location of the final fracture in length direction varies but that the shape of the fracture surface is stable.

For the numerical simulation of the experiment not only the striker but also input and output bar and the specimen as well as the spacers and the cap have to be modeled. Fig. 6.23 displays the mesh of half of a M-Shape

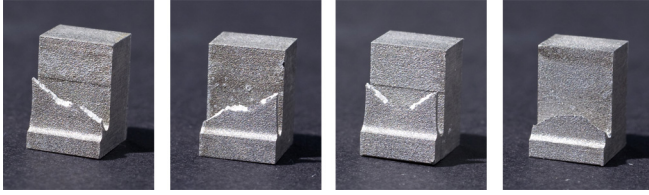


Figure 6.21: Fractured aluminum M-Shape specimens, thickness 6.35 mm

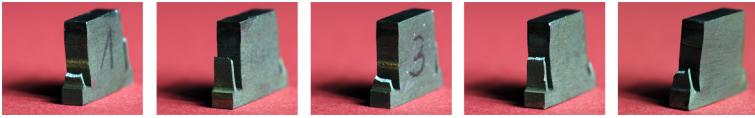


Figure 6.22: Fractured Inco 304L M-Shape specimens

specimen including the spacer for Inco 304L. The central tension part has 8 elements in width direction and 36 elements in thickness direction, i.e. elements have a minimum edge length of approximately 0.0625 mm. For the aluminum alloy a similar mesh has been used with 72 elements in thickness direction. The applied technique of mesh refinement results into an element size of 0.75 mm in the contact zones with the bars, i.e. the proportion of element sizes between bars and specimen is about 1:3.

As shown in Fig. 6.23, the corners of the spacer have been slightly ablated to avoid contact problems with sharp edges while the zone is of no further interest for the analysis of the experiments. Furthermore, the mesh size has been adapted to the corresponding mesh size of the specimen in that region. The cap is modeled in a simple way as shown in Fig. 6.24, but considering the mesh of the bars to avoid initial penetration problems. The material behavior of the spacers as well as of the cap is assumed to be linear-elastic with parameters corresponding to steel. In addition, all contacts have been realized by surface to surface definitions while the friction coefficient was set to 0.01.

For the aluminum alloy, numerical simulations including the complete experimental setup have been performed while rate and temperature dependence as well as the proposed fracture criterion are considered. Fig. 6.25 displays the damage evolution at the center of the tension part before first fracture occurrence, i.e. before the first element erosion took place. Comparing these results with those obtained at the studies of the reduced M-Shape, Fig. 6.10, a similar behavior can be observed. Major damage

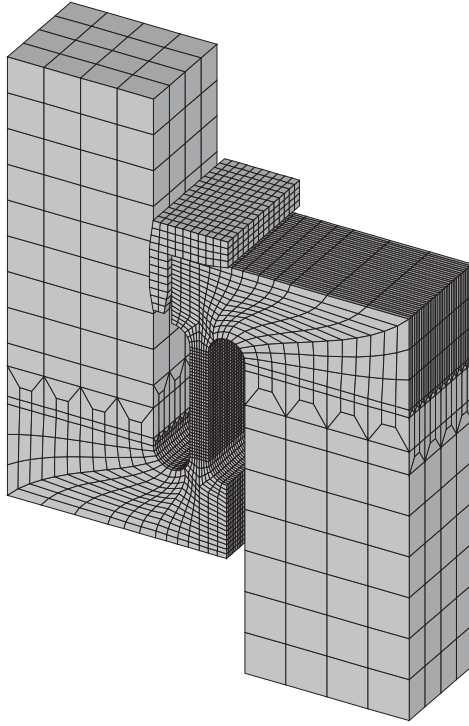


Figure 6.23: Mesh of M-Shape specimen, for illustration purposes only half displayed with corresponding spacer

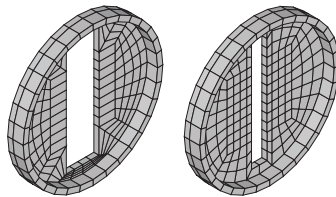


Figure 6.24: Mesh of cap; left for aluminum M-Shape, right for steel M-Shape

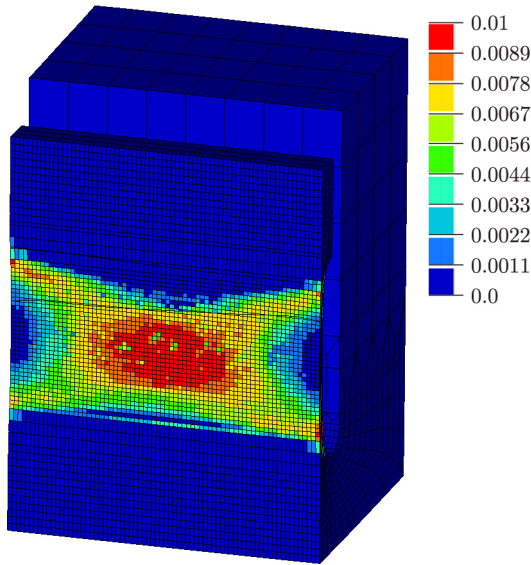


Figure 6.25: Damage evolution of aluminum M-Shape specimen

evolution occurs at the center of the specimen and on the edge closer to the thicker part which appears to be in an x-shape. The resulting fracture surface (Fig. 6.26) has also a shape similar to the one predicted by the numerical simulations of the reduced M-Shape. The crack evolves at the central region as well as from the outside. These results show good agreement with the experimentally achieved results displayed in Fig. 6.21, especially with the last picture in this figure.

Different simulations have been performed with the M-Shape specimen made of Inox 304L: elastic-plastic without rate and temperature dependence and without fracture, elastic-plastic-damage with fracture but without rate and temperature dependence as well as elastic-plastic-damage with rate and temperature dependence and with fracture. Furthermore, these simulations have been used to identify the material parameters of the damage softening law as well as of the fracture criterion. Firstly the simulations with elastic-plastic-damage material behavior and fracture but without rate and temperature dependence have been realized. With these simulations the parameters which are given in Chap. 5 have been calibrated. In continuation, rate and temperature dependence has been also taken into account and the respective results are compared.

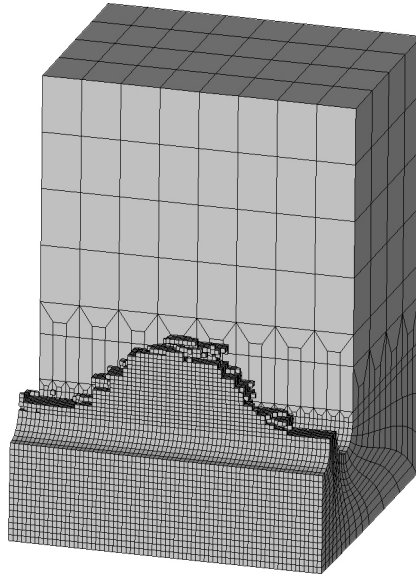


Figure 6.26: Predicted fracture of aluminum M-Shape specimen

In Fig. 6.27, the reported strains at the center of the input and output bar are plotted for a simulation with elastic-plastic material behavior and for a simulation with elastic-plastic-damaged material behavior considering rate and temperature dependence and fracture for a striker velocity of 10.0 m/s . Comparing both transmitted waves, it can be observed that the amplitude of the transmitted wave of the simulation with elastic-plastic material behavior is remarkably lower than the one considering rate and temperature dependence and thus the stiffer material response due to strain rate hardening is nicely reflected. Furthermore, the fracture of the specimen is clearly indicated by the dropout of the transmitted wave. Comparing the qualitative characteristics of the numerically predicted curve with the one obtained experimentally (Fig. 6.20), good correlation is achieved with respect to the development as well as to the fracture time, but the experimentally obtained curve initially shows a higher amplitude.

To gain insights into the general behavior of the M-Shape specimen during the deformation process, the contact forces between input bar and M-Shape specimen and between M-Shape specimen and output bar as well as the summed forces of both thin tension parts on the incoming and

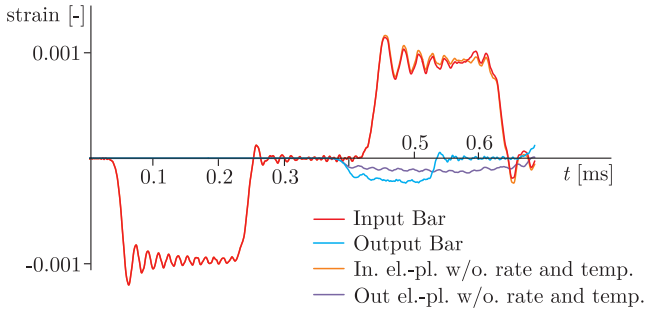


Figure 6.27: Strains in input and output bar of simulation with M-Shape specimen (Inox 304L)

outgoing side are monitored, Fig 6.28. Here the pulsative distribution of the contact forces between the input bar and the specimen are conspicuous while the thin tension part is almost instantaneously in static equilibrium. The contact forces between the specimen and the output bar show a pulsative distribution at a similar frequency but with remarkably smaller amplitude. The frequency of these contact forces is neither comparable to the magnitude of the frequency of the bar dispersion nor to the frequency of the incoming compression part of the specimen. This behavior might result directly from the general soft response of the specimen as indicated by the transmitted wave or from the elevated and complex wave propagation through the specimen. At this point it is important to notice that the overall static equilibrium needed for the extraction of material curves is not reached - only in an integrated sense.

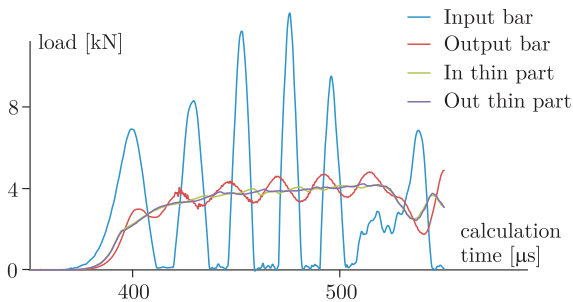


Figure 6.28: Forces during deformation process of M-Shape specimen

These considerations lead to a closer look at the plasticized zones of the specimen. Fig. 6.29 displays the internal plastic variable γ after final fracture, while the legend is restricted to 9%, allowing to observe values above 1%. Major plastic deformation with values of above 30% are restricted to the central tension part with relatively small transmission zones and hence the expected behavior is achieved.

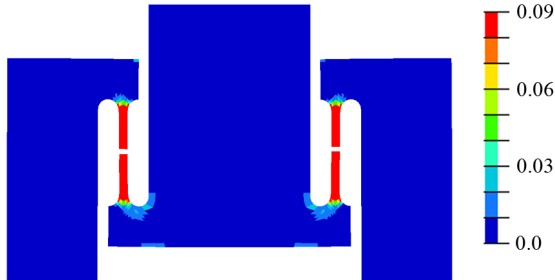


Figure 6.29: Plasticized region of M-Shape specimen (Inox 304L) after final fracture, internal plastic variable γ

The stress state, i.e. the triaxiality has a remarkable influence on the damage behavior of the material. Fig. 6.30_a indicates the triaxiality at the center of the tension part before first damage occurrence while a rather homogeneous state around the expected value of $1/3$ is reached. Furthermore, it is important to notice that the evolution of damage, i.e. the softening of the material has an important influence on the stress state; the material eludes the load [33]. The three pictures at the right hand side of Fig. 6.30 demonstrate the damage evolution at the center of the tension part for material behavior neglecting the rate and temperature dependence. Damage evolution takes place over a rather long time starting from the center towards the outside forming one central damaged zone as known from static tension tests [112]. Finally fracture, i.e. element erosion, starts as well at the center and the crack propagates perpendicular to the loading direction.

In contrast, Fig. 6.31 displays the damage evolution for rate and temperature dependent material behavior. In this case, damage occurs at various locations spread over the complete thin tension part of the specimen. In continuation, several clusters perpendicular to the tension direction are forming over a rather short period of time with first fracture occurring close to the thicker part while the crack evolves perpendicular to the tension direction. The finally fractured specimens (Fig. 6.22) are characterized by fracture surfaces perpendicular to the tension direction which

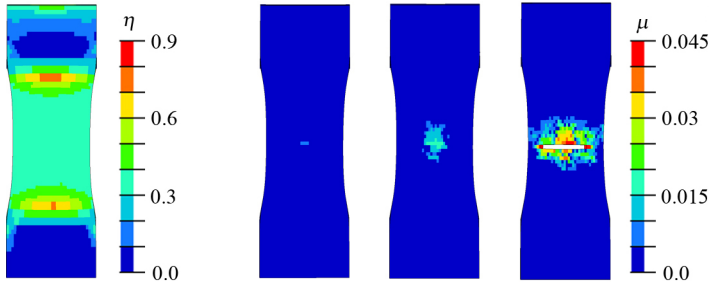


Figure 6.30: Triaxiality before first damage occurrence and damage evolution of M-Shape specimen (tension part, Inco 304L) without temperature and strain rate dependence, internal damage variable μ ; time between images $6.0 \mu\text{s}$

can occur at various locations of the tension part. That might be seen as an indication that damage also takes place at almost the complete central region and that final fracture is initiated at some weak point of the specimen. Furthermore, the behavior is remarkably different to the one predicted without rate and temperature dependence (Fig 6.30); damage does not evolve in a central region but in clusters perpendicular to the loading direction. Also, the contour of the central region is more elongated, i.e. less necking is predicted which also reflects better the real behavior of the specimen.

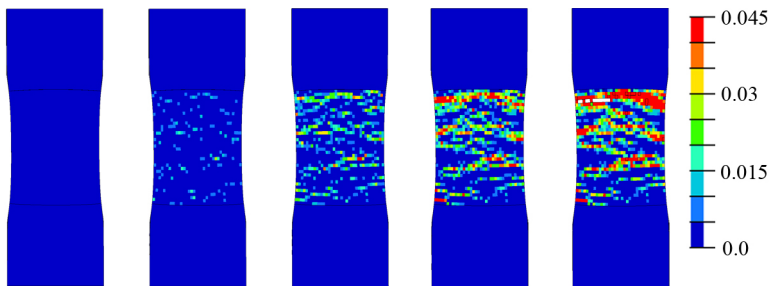


Figure 6.31: Damage evolution of M-Shape specimen (tension part, Inco 304L) with temperature and strain rate dependence, internal damage variable μ ; time between images $1.0 \mu\text{s}$

In addition, the temperature evolution of the central part is given in

Fig. 6.32 which is directly related to the plastic deformation. The temperature increase is rather homogeneous distributed over the central region with its maxima at the center. The maximum value before damage occurrence is at 81°C within the temperature region studied experimentally but already leading to remarkable material softening.

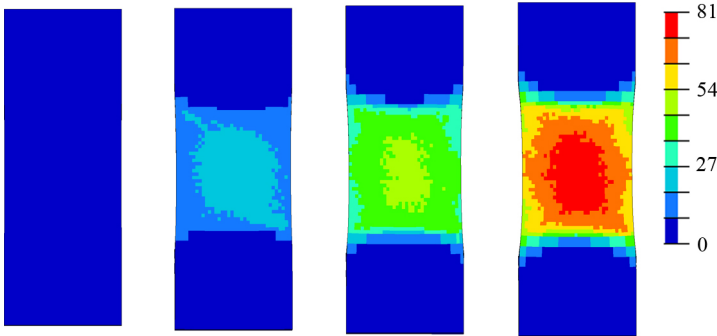


Figure 6.32: Temperature evolution of M-Shape specimen (tension part, Inox 304L) before damage occurrence, time between images $20.0 \mu\text{s}$ - change float

All in all, the numerical results of the Split-Hopkinson-Bar experiments with M-Shaped specimens modeled with the presented material behavior including plastic, damage and fracture lead to a good correlation with the experimentally achieved results. During the experimental and numerical work with specimen presented by Mohr and Gary [117, 118] in its adopted form a good insight was gained. This leads to several positive aspects, such as:

- It can be used in a standard Split-Hopkinson-Pressure-Bar without any modification to the experimental setup.
- The specimen can be designed in such a way that important inelastic deformations take place only in the designated central part and final fracture takes place in the first wave propagation.

As well as to some negative aspects, such as:

- High cost of manufacture due to the rather complex geometry in combination with required precise production.
- Difficult to handle in the experimental setup due to the spacers and the cap which have to be located with extra care.
- The amplitude of the transmitted wave is rather small.
- During the experiment, the specimen is not in static equilibrium,

i.e. it is questionable if it can be used for the extraction of material curves.

6.5 Split-Hopkinson-Bar tests: Shear specimen

All specimens discussed until this point show damage and fracture behavior in compression or tension dominated range and consequently the need of a specimen geometry leading to failure in a shear-like mode is evident. In this context Singh et al. [146] proposed two geometries which lead to shear-like damage and fracture. These geometries have been adopted for the use with the stainless steel Inco 304L in simulations of corresponding Split-Hopkinson-Bar experiments. With these first numerical results it seemed likely that a notch in thickness direction could improve the behavior of the specimen significantly and thus additional simulations with different notched specimens have been performed and the results are presented in correlation. All these simulations have been realized without consideration of strain and temperature dependence.

The adopted geometries are presented in Figs. 6.33 (shape 1) and 6.34 (shape 2). The pulse of the input bar is induced in the central elevated part while the opposite side is in contact with the output bar. Shape 1 is characterized by sharp edges and a relatively small offset of 0.1 mm between the width of the central part and the central hole while shape 2 is characterized through a rounded-out transmission part between the central inducing part and the body of the specimen and a bigger offset of 1.0 mm. The notch in thickness direction has the shape of a quadratic function whereas its pass is at the center of the offset. For shape 1 the depth amounts 0.5 mm, its width is 1.1 mm and on both sides it blends also in the shape of a quadratic function, Fig. 6.36. For shape 2, two different notches are considered, one of depth 0.5 mm and width 1.0 mm and one of depth 1.0 mm and width 2.0 mm, Fig. 6.37.

The mesh for shape 1 (Fig. 6.35) contains a total of 91,081 elements while in the shear region 36 elements in thickness direction have been used. This mesh has been used as base to create the mesh of the notched specimen by simply moving the existing nodes to the desired shape, Fig. 6.36. The mesh for shape 2 contains a total of 64,056 elements while the mesh of the notched specimen has been created in the same way as for shape 1, Fig. 6.37.

For these simulations a steel striker (300 mm), a steel input bar (2007 mm) and an aluminum output bar (1400 mm) have been used while the striker velocity was set to 25.0 m/s. The higher striker velocity, compared to the simulation with Inco 304L M-Shape specimens, leads to significantly

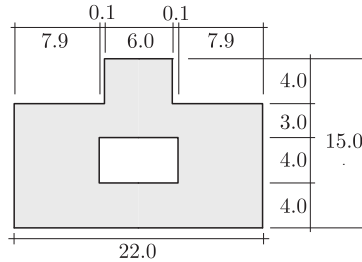


Figure 6.33: Geometry of shear specimen, shape 1; all measures in [mm]

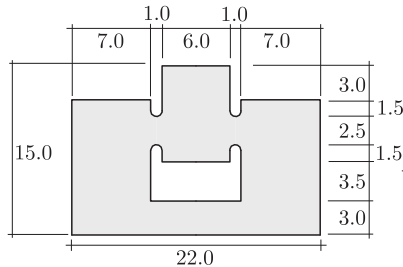


Figure 6.34: Geometry of shear specimen, shape 2; all measures in [mm]

higher amplitudes of the incoming wave while the shorter striker causes a shorter wave. As first study, Fig. 6.38 displays the incoming wave, the reflected wave as well as the transmitted wave of a series of simulations with un-notched and notched shear specimens of shape 2. For all three simulations the incoming wave has the same distribution while the reflected waves show differences. The transmitted wave of the un-notched specimen is remarkably longer than the one of the notched specimens which both show almost the same length while the maximum amplitude of the transmitted wave reflects the remaining cross section of the shear zone.

In addition, the contact forces during the deformation process have been monitored. Both specimen shapes show similar behavior while the un-notched specimens are more likely to reach the state of static equilibrium, Figs. 6.39 and 6.40 and the time of the deformation process until fracture of the un-notched specimen is about twice as long as the time needed by the notched specimen. Furthermore, it can be noted that the contact time for shape 1 is shorter before fracture occurs, i.e. a more brittle specimen behavior is given. In contrast to the M-Shape specimen (Fig. 6.28), the

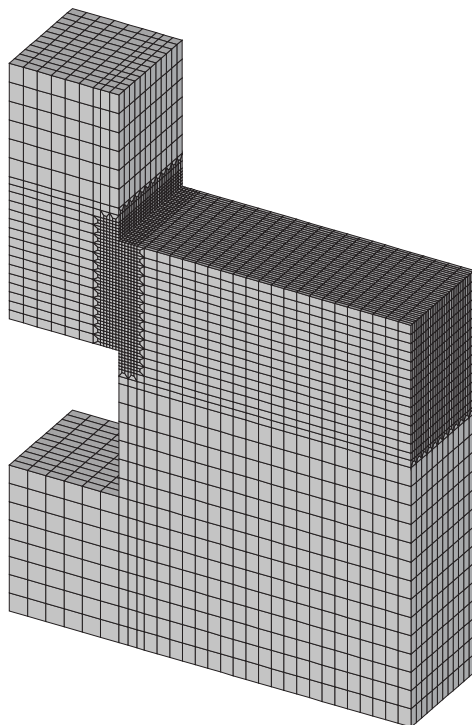


Figure 6.35: Mesh of shear specimen, for illustration purposes only half displayed

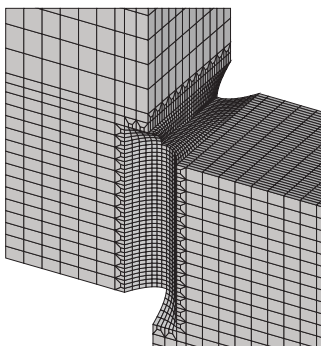


Figure 6.36: Detail of notched, meshed shear specimen

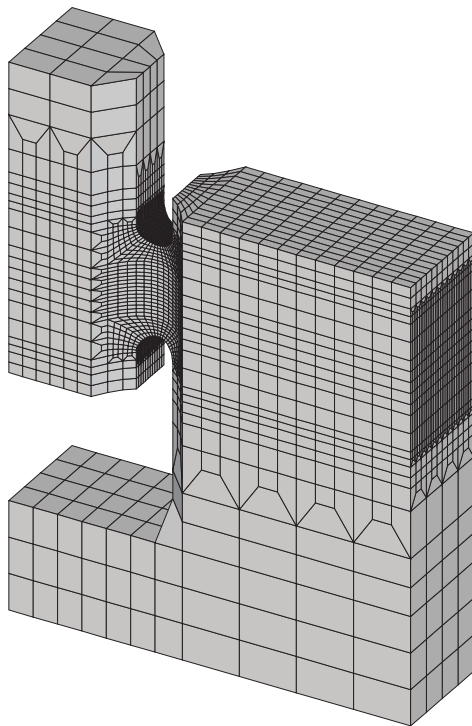


Figure 6.37: Mesh of shear specimen, shape 2 with 1.0 mm notch, for illustration purposes only half displayed

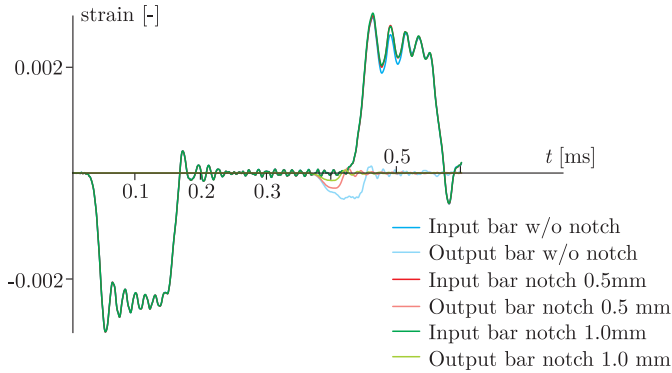


Figure 6.38: Strains in input and output bar of simulation with shear specimen, shape 2, Inox 304L

contact forces between the input bar and specimen do not oscillate which can be seen as a major advantage.

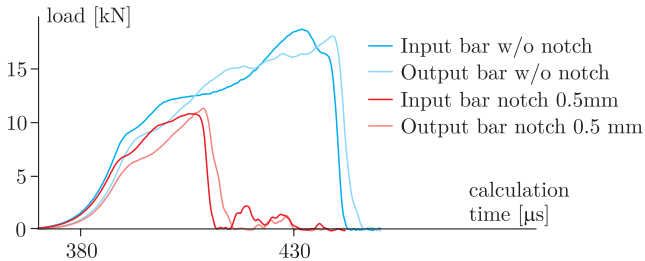


Figure 6.39: Contact forces during deformation process of shear specimen, shape 1, Inox 304L

To explain the remarkable longer time of the deformation process of the un-notched specimens, the plasticized zones of the different geometries are compared after final fracture, see Figs. 6.41 and 6.42 where the internal plastic variable γ at the center plane of the specimen is displayed while the legend is scaled to a maximum value of 0.9 although more elevated values occur. The un-notched specimen of shape 1 (Fig.6.41_a) is characterized through elevated plastic deformations in an extensive region around the shear part while major regions of the inducing part are still plastically deformed. The notched specimen of shape 1 (Fig.6.41_b) reacts differently,

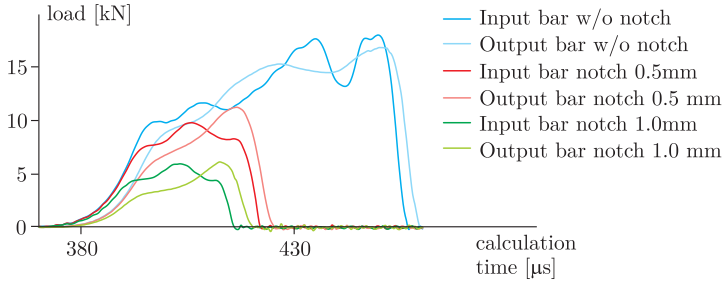


Figure 6.40: Contact forces during deformation process of shear specimen, shape 2, Inox 304L

here plastic deformations are restricted to a very limited region of the shear zone and the inducing part does not show plastic deformation above $\gamma = 0.01$.

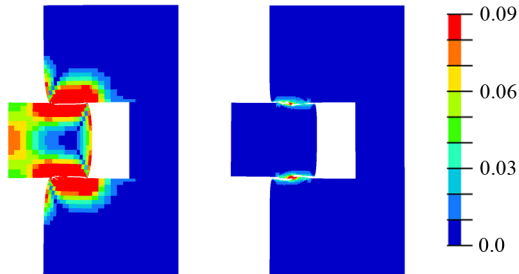


Figure 6.41: Plasticized region of shear specimen shape 1 after final fracture, internal plastic variable γ , left to right: un-notched and notch 0.5 mm

The shear specimen shape 2 shows similar behavior to shape 1. The behavior of the un-notched specimen (Fig.6.42_a) is characterized through significant zones of plastic deformation while even the transmitting part to the output bar is included which leads to remarkable bending of the lateral supports. The specimens with 0.5 mm and 1.0 mm deep notch of shape 2 (Fig.6.42_{b,c}) show very similar behavior while the plasticized zone of the specimen with 0.5 mm deep notch is slightly larger. Overall, it can be noticed that weakening the shear region with a notch does remarkably change the behavior of the specimen leading to a more concentrated zone of elevated deformation.

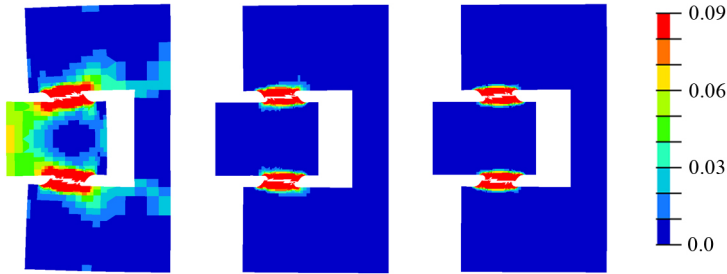


Figure 6.42: Plasticized region of shear specimen shape 2 after final fracture, internal plastic variable γ , left to right: un-notched, notch 0.5 mm and notch 1.0 mm

Furthermore, the stress state and the damage evolution of the different specimen shapes are of interest. Fig. 6.43 displays results of the shear specimen shape 1 without notch. The triaxiality η of the shear zone is distributed rather homogeneous in thickness direction with values in the low negative range and the corresponding internal plastic variable γ is distributed as well homogenous. First damage occurrence is predicted on the outside of the specimen, but not in its direct shear zone. The damage evolution, characterized through the internal damage variable μ , takes place over a rather long period and is first characterized through elevated values close to the sharp edges of the shear zone where also the final crack, i.e. element erosion, starts. Damage then evolves towards the center of the specimen which leads to final fracture.

Fig. 6.44 displays the corresponding results of the notched shear specimen shape 1. The triaxiality η shows considerable differences over the thickness direction while close to the notch surface negative values close to 0 occur, the values at the center are already close to -0.25 . Thus this specimen leads to non-constant values of triaxiality, but covering the region of special interest from 0.0 to $-1/3$. The corresponding internal plastic variable γ is characterized through higher values close to the notch and remarkably lower values at the center of the specimen. Consequently, the corresponding damage μ evolves first on its outside at the center of the notch close to the sharp geometry edge and then propagates towards the center while the evolving crack follows this direction. In comparison with the un-notched specimen besides the differences in triaxiality it is noteworthy that the damage evolution takes place over a shorter time period.

In continuation the triaxiality and the damage evolution of the shear spec-

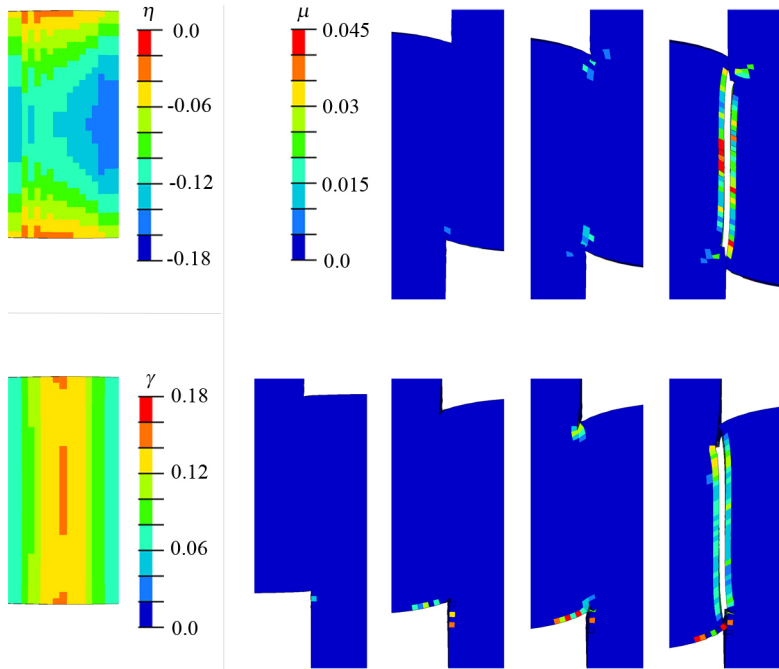


Figure 6.43: Triaxiality η and internal plastic variable γ before damage of shear zone over thickness direction; damage μ evolution at center of specimen (top row) and corresponding at surface of shear specimen shape 1, time between images $14.0 \mu\text{s}$

imens shape 2 without notch and with 1.0 mm notch are presented in the central plane of the specimen while cut outs of the shear zone are taken, Figs. 6.45 and 6.46. The triaxiality of the un-notched specimen shows values of approximately -0.1 in the damage zone which are similar to the values of the un-notched shear specimen shape 1. The damage evolution occurs over a rather long time period leading to a damage zone covering the complete shear region before macro-cracking occurs. The triaxiality of the notched specimen reaches values of approximately -0.05 at the presented central region which is remarkably higher than the triaxiality of the notched shear specimen shape 1 where values of -0.25 are predicted. Furthermore, the damage evolution takes place rather concentrated at the center of the notch and it evolves over a rather short period of time.

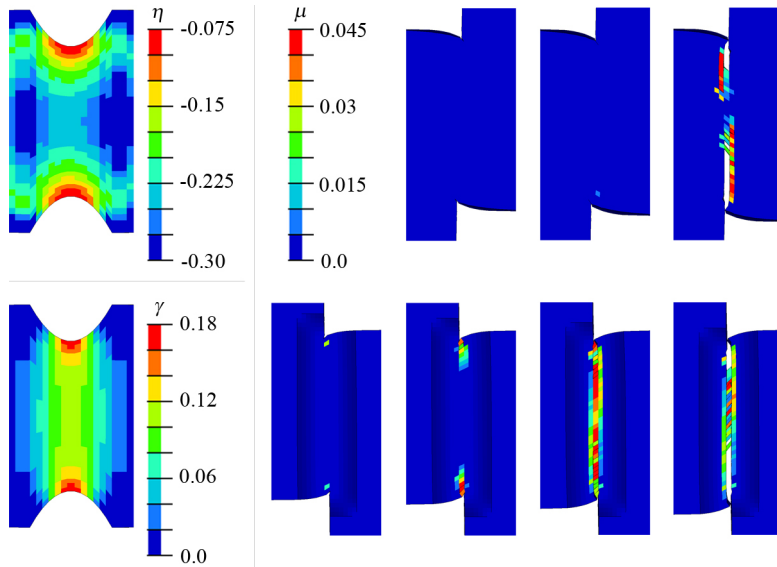


Figure 6.44: Triaxiality η and internal plastic variable γ before damage of shear zone over thickness direction; damage μ evolution at center of specimen (top row) and corresponding at surface of notched shear specimen shape 1, notch 0.5 mm, time between images $3.0 \mu\text{s}$

The results of these first numerical studies lead to a number of observations and conclusions, namely:

- The presented shear specimens lead to damage and fracture at negative triaxialities.
- By the introduction of additional notches in thickness direction, major inelastic deformations can be restricted to the shear zone of the specimen and thus the shear behavior can be monitored experimentally.
- The specimens can be used in a regular Split-Hopkinson-Pressure-Bar setup without any modification. Furthermore, this type of specimen can be used without any additional parts, such as spacers and cap as for M-Shape specimen, which facilitates the handling.
- The magnitude of the transmitted wave is in a range where it can be experimentally measured.

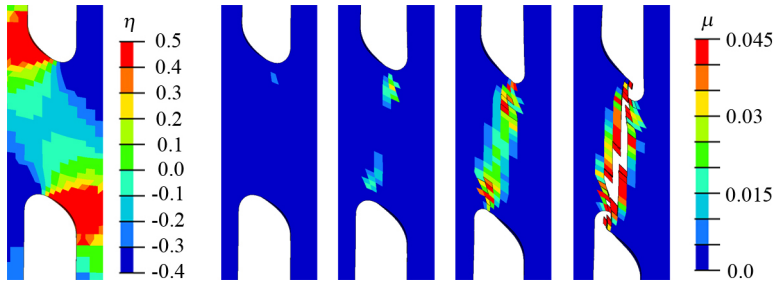


Figure 6.45: Triaxiality before first occurrence of damage and damage evolution of shear specimen (Inox 304L) without temperature and strain rate dependence, internal damage variable μ ; time between images $13.0 \mu\text{s}$

In addition, it is interesting to notice that the presented shear geometries are symmetric, i.e. two shear zones are located on both sides of a central region which is pressed into a rather compact body. This minimizes the rotations of the designated shear regions. It is likely that this observation can be transferred to the design of shear specimens for static tests which might also lead to a major reduction of rotations in the shear zone while the combination with additional notches in thickness direction is possible.

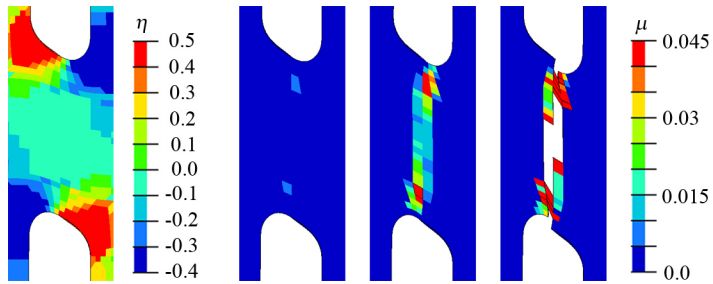


Figure 6.46: Triaxiality before first occurrence of damage and damage evolution of shear specimen (Inox 304L) with notch of 1.0 mm, without temperature and strain rate dependence, internal damage variable μ ; time between images $3.0 \mu\text{s}$

7 Closure

7.1 Summary and conclusions

This thesis covers damage and fracture behavior of ductile metals under special consideration of the stress state, the effects of strain rate hardening and softening due to temperature increase. In this connection, a phenomenological continuum damage and fracture model is introduced which is implemented into a commercial simulation software. To identify the material parameters of the model, several different experiments have been performed and the procedure of parameter identification has been discussed in detail for a stainless steel. To demonstrate the applicability of the model, several different simulations of executed experiments including deformations with high strain rates have been performed. In addition, the numerical modeling of the experimental setup as well as the specimen shape have been reviewed in detail, resulting in several new insights on both subjects.

Overall, the achieved results improve significantly the understanding of the deformation and fracture behavior of ductile metals. This new knowledge can be used in several applications such as the design of light weight structures and the simulation of car crashes or high speed machining processes, allowing a maximum utilization of the material which results into a more responsible and cost-efficient handling of resources.

The presented continuum damage model is based upon the work presented by Brünig [26, 27, 28]. One of the main characteristics of the model is the fact that damage tensors are directly introduced within the kinematic framework and thus no stress or strain equivalence is needed, as frequently used in other damage models. Furthermore, a consistent thermodynamic framework is developed which leads by the introduction of corresponding potential functions to the definition of an effective stress tensor on the undamaged configuration and a stress tensor on the damaged configuration. Different damage mechanisms which appear at different stress states are considered by a triaxiality dependent damage criterion as well as by a triaxiality dependent damage law. In addition, temperature and strain rate effects are considered by a multiplicative decomposition of the plastic hardening as well as the damage softening function.

In the context of this thesis, the continuum damage model has been modified and extended: Firstly the triaxiality-dependence of the damage con-

dition and of the damage process has been studied in detail. Secondly, a new quadratic damage softening function has been proposed which provides a smooth damage initiation and leads to reasonable damage evolution. Thirdly, a new triaxiality dependent fracture criterion based on the internal damage variable has been proposed which allows the description of the complete deformation process up to final fracture and leads to a good estimation of the experimentally achieved fracture surface.

To make the continuum damage and fracture model accessible to numerical simulations, the commercial Finite Element software LsDyna has been augmented by a user material subroutine. Partially, this coding has been realized within the framework of this thesis and thus the developed theory has been transferred to computer code. In this context, the main thoughts of the Finite Element Method have been presented and it has been commented on the explicit time integration scheme. To complete the picture, a detailed description of the LsDyna user interface is given.

To characterize the behavior of ductile metals at different strain rates, temperatures and stress states, several different experiments can be used and in this context an overview has been presented within this thesis. To identify the material parameters of the materials reviewed in this thesis - which are aluminum and the stainless steel Inox 304L - several experiments have been performed in collaboration with the GMSIE lab at the University of São Paulo (USP), Brazil. For the stainless steel Inox 304L, the procedure of material parameter identification has been discussed in detail, also pointing out the need of additional experiments. Furthermore, a new inverse technique to identify the parameters of the damage softening law and of the fracture criterion has been proposed which can be used even if no further information from experiments or micromechanical numerical studies is available. In addition, Split-Hopkinson-Bar experiments have been realized which use rings and special, recently presented M-Shape specimens.

Split-Hopkinson-Bar experiments are commonly used to study the material behavior under high strain rates while the setup is characterized through relatively big bars which clamp relatively small specimens. Before this thesis, the numerical study of the complete experimental setup is not commonly realized, specially not with an volume model. Therefore, firstly, several aspects such as mesh size of the bars or how to extract the strains of the bars have had to be studied in detail. Following, a numerical model could be presented which achieves sufficiently precise results with acceptable computational costs.

After creation of this numerical model, simulations of the executed Split-Hopkinson-Bar experiments have been realized while the specimen was modeled with the presented continuum damage and fracture model, us-

ing the identified material parameters. With these simulations, a good correlation between experiments and numerical results could be achieved, which demonstrates the applicability of the model. In this connection an interesting observation has been made: For material which is not rate- and temperature-dependent, damage evolves in a central region while for material that is rate- and temperature-dependent, damage occurs in clusters over the complete tension part. Another important insight has been that the used M-Shape specimen has to be evaluated critically, indicating that the static equilibrium, i.e. the equilibrium of the forces between input bar and specimen as well as between specimen and output bar, is not fulfilled. Therefore, it is questionable if the experimental results can be used to identify material parameters.

Furthermore, numerical studies with two specimen shapes which fracture in a shear like mode have been realized. Overall, these specimens demonstrate a more stable behavior compared with the previously studied M-Shape specimen. To overcome the deficit of plastic deformations of major specimen parts, a notch in thickness direction has been introduced which causes a focussed plastic region within the shear part of the specimen which leads to final fracture of this part. This geometry implies the use of symmetric specimen geometries with two shear regions also for static tests where notches in thickness direction can concentrate the region of inelastic deformations.

7.2 Perspective

The presented continuum damage and fracture model facilitates the detailed description of the behavior of ductile metals reflecting its triaxiality, strain rate and temperature dependence. To be able to apply these abilities in a correct way, the identification of the corresponding material parameter is crucial. The following points can be seen as special focus for future research:

- Developing new specimen geometries which lead under controlled conditions to major inelastic deformations and final fracture at different stress states. Especially the testing of the proposed shear specimens within a Split-Hopkinson-Bar experiment is of interest.
- Performing further micro-mechanical studies including one pore models as well as pore clusters to develop an inverse method to study damage evolution and fracture behavior and extract results for the phenomenological model. These studies could be extended to dynamic cases, i.e. three-dimensional models with wave propagation phenomena.

- These insights might result in the need to review the proposed damage and fracture model. Especially the influence of the Lode parameter will have to be studied in detail. The further developments should be sufficiently accurate to reflect the important phenomena but also as simple as possible to be easily manageable and to reduce the effort to identify the corresponding material parameters.

However, this scientific work can be seen as an important step on the way to substitute cost-worthy and complicated prototyping by elaborated numerical simulations. Scientists as well as engineers should be able to use the results in order facilitate the design of specimens as well as of complete structures. Overall, this thesis should be helpful for saving development costs and to find out more precise how materials will react in damage processes.

Bibliography

- [1] AISI Type 304 stainless steel. Technical report, ASM Aerospace Specification Metals Inc., Pompano Beach, USA, 2012.
- [2] Product information 304/304L. Technical report, Rolled Alloys, Temperance, USA, 2012.
- [3] Stainless steel AISI type 304L. Technical report, efunda, Sunnyvale, USA, 2012.
- [4] H. Altenbach and J. J. Skrzypek, editors. *Creep and Damage in Materials and Structures*. Springer, Wien, 1999.
- [5] M. Alves and N. Jones. Impact failure of beams using damage mechanics: Part ii - application. *International Journal of Impact Engineering*, 27:863–890, 2002.
- [6] M. Alves, D. Karagiozova, G. Micheli, and M. Calle. Limiting the influence of friction on the split hopkinson pressure bar tests by using a ring specimen. *International Journal of Impact Engineering*, 49:130–141, 2012.
- [7] F. M. Andrade Pires, J. M. A. César de Sá, L. Costa Sousa, and R. M. Natal Jorge. Numerical modelling of ductile plastic damage in bulk metal forming. *International Journal of Mechanical Sciences*, 45:273–294, 2003.
- [8] M. Arcan, Z. Hashin, and A. Voloshin. A method to produce uniform plane-stress states with applications to fiber-reinforced materials. *Experimental Mechanics*, 18:141–146, 1978.
- [9] Y. Bai and T. Wierzbicki. A new model of metal plasticity and fracture with pressure and lode dependence. *International Journal of Plasticity*, 24:1071–1096, 2008.
- [10] Y. Bao and T. Wierzbicki. On the fracture locus in the equivalent strain and stress triaxiality space. *International Journal of Mechanical Sciences*, 46:81–98, 2004.
- [11] Y. Bao and T. Wierzbicki. On the cut-off value of negative triaxiality for fracture. *Engineering Fracture Mechanics*, 72:1049–1069, 2005.
- [12] R. Becker, A. Needleman, O. Richmond, and V. Tvergaard. Void growth and failure in notched bars. *Journal of the Mechanics and Physics of Solids*, 36:317–351, 1988.

- [13] T. Belytschko, W. K. Liu, and B. Moran. *Nonlinear Finite Elements for Continua and Structures*. Wiley, Chichester, 2001.
- [14] A. Benzerga, Y. Bréchet, A. Needleman, and E. Van der Giessen. The stored energy of cold work: Predictions from discrete dislocation plasticity. *Acta Materialia*, 53:4765–4779, 2005.
- [15] A. Benzerga and J.-B. Leblond. Ductile fracture by void growth to coalescence. *Advances in Applied Mechanics*, 44:169–305, 2010.
- [16] L. Berkovic, A. Chabotier, F. Coghe, and L. Rabet. Measuring and modeling of low temperature Hopkinson tests. *Procedia Engineering*, 10:1645–1650, 2011.
- [17] J. Betten. Net-stress analyses in creep mechanics. *Ingenieur-Archiv*, 52:405–419, 1982.
- [18] J. Betten. Damage tensors in continuum mechanics. *Journal de Mécanique Théorique et Appliquée*, 2:13–32, 1983.
- [19] M. Bever, D. Holt, and A. Titchener. The stored energy of cold work. *Progress in Materials Science*, 17:5–177, 1973.
- [20] N. Bonora. A nonlinear CDM model for ductile failure. *Engineering Fracture Mechanics*, 58:11–28, 1997.
- [21] N. Bonora, D. Gentile, A. Pirondi, and G. Newaz. Ductile damage evolution under triaxial state of stress: theory and experiments. *International Journal of Plasticity*, 21:981–1007, 2005.
- [22] T. Børvik, O. S. Hopperstad, and T. Berstad. On the influence of stress triaxiality and strain rate on the behaviour of a structural steel. part ii. numerical study. *European Journal of Mechanics A/Solids*, 22:15–32, 2003.
- [23] M. Brünig. Large strain elastic-plastic theory and nonlinear finite element analysis based on metric transformation tensors. *Computational Mechanics*, 24:187–196, 1999.
- [24] M. Brünig. Numerical simulation of the large elastic-plastic deformation behavior of hydrostatic stress-sensitive solids. *International Journal of Plasticity*, 15:1237–1264, 1999.
- [25] M. Brünig. A framework for large strain elastic-plastic damage mechanics based on metric transformations. *International Journal of Engineering Science*, 39:1033–1056, 2001.
- [26] M. Brünig. An anisotropic ductile damage model based on irreversible thermodynamics. *International Journal of Plasticity*, 19:1679–1713, 2003.
- [27] M. Brünig. Numerical analysis of anisotropic ductile continuum damage. *Computer Methods in Applied Mechanics and Engineering*, 192:2949–2976, 2003.

- [28] M. Brünig. Continuum framework for rate-dependent behavior of anisotropic damaged ductile metals. *Acta Mechanica*, 186:37–53, 2006.
- [29] M. Brünig, D. Albrecht, and S. Gerke. Modelling of ductile damage and fracture behavior based on different micromechanisms. *International Journal of Damage Mechanics*, 20:558–577, 2011.
- [30] M. Brünig, D. Albrecht, and S. Gerke. Numerical analyses of stress-triaxiality-dependent inelastic deformation behavior of aluminium alloys. *International Journal of Damage Mechanics*, 20:299–317, 2011.
- [31] M. Brünig, O. Chyra, D. Albrecht, L. Driemeier, and M. Alves. A ductile damage criterion at various stress triaxialities. *International Journal of Plasticity*, 24:1731–1755, 2008.
- [32] M. Brünig and L. Driemeier. Numerical simulation of Taylor impact tests. *International Journal of Plasticity*, 23:1979–2003, 2007.
- [33] M. Brünig and S. Gerke. Simulation of damage evolution in ductile metals undergoing dynamic loading conditions. *International Journal of Plasticity*, 27:1598–1617, 2011.
- [34] M. Brünig, S. Gerke, and V. Hagenbrock. Micro-mechanical numerical studies on the stress state dependence of ductile damage. In H. Altenbach and S. Kruch, editors, *Advanced Materials Modelling for Structures (Advanced Structured Materials)*, 19:87–96, 2013.
- [35] M. Brünig, S. Gerke, and V. Hagenbrock. Micro-mechanical studies on the effect of the stress triaxiality and the Lode parameter on ductile damage. *International Journal of Plasticity*, doi: 10.1016/j.ijplas.2013.03.012, 2013.
- [36] O. Bruhns and P. Schiesse. A continuum model of elastic-plastic materials with anisotropic damage by oriented microvoids. *European Journal of Mechanics A/Solids*, 15:367–396, 1996.
- [37] T. Byun, N. Hashimoto, and K. Farrell. Temperature dependence of strain hardening and plastic instability behaviors in austenitic stainless steels. *Acta Materialia*, 52:3889–3899, 2004.
- [38] J.-L. Chaboche. Continuous damage mechanics – a tool to describe phenomena before crack initiation. *Nuclear Engineering and Design*, 64:233–247, 1981.
- [39] J. L. Chaboche. Anisotropic creep damage in the framework of continuum damage mechanics. *Nuclear Engineering and Design*, 79:309–319, 1984.
- [40] J. L. Chaboche. Continuum damage mechanics: Present state and future trends. *Nuclear Engineering and Design*, 105:19–33, 1987.

- [41] J. L. Chaboche. Continuum damage mechanics: Part I - general concepts. *Journal of Applied Mechanics*, 55:59–64, 1988.
- [42] J. L. Chaboche. Continuum damage mechanics: Part II – damage growth, crack initiation and crack growth. *Journal of Applied Mechanics*, 55:65–72, 1988.
- [43] S. Chandrakanth and P. C. Pandey. A new ductile damage evolution model. *International Journal of Fracture*, 60:R73–R76, 1993.
- [44] W. W. Chen and B. Song. *Split Hopkinson (Kolsky) bar; design, testing and applications*. Springer, New York, 2011.
- [45] C. L. . Chow and J. Wang. An anisotropic theory of continuum damage for ductile fracture. *Engineering Fracture Mechanics*, 27:547–558, 1987.
- [46] J. Cordebois and F. Sidoroff. Anisotropic damage in elasticity and plasticity. *Journal de Mécanique Théorique et Appliquée*, Numéro spécial:45–60, 1982.
- [47] E. de Souza Neto and D. Peric. A computational framework for a class of fully coupled models for elastoplastic damage at finite strains with reference to the linearization aspects. *Computer Methods in Applied Mechanics and Engineering*, 130:179–193, 1996.
- [48] R. Desmorat and S. Cantournet. Modeling microdefects closure effects with isotropic/anisotropic damage. *International Journal of Damage Mechanics*, 17:65–96, 2008.
- [49] P. Dondeti, D. Paquet, and S. Ghosh. A rate-dependent homogenization based continuum plasticity-damage (HCPD) model for dendritic cast aluminum alloys. *Engineering Fracture Mechanics*, 89:75–97, 2012.
- [50] D. C. Drucker and W. Prager. Soil mechanics and plastic analysis or limit design. *Quarterly of Applied Mathematics*, 10, 2:157–165, 1952.
- [51] L. Engel and H. Klingele. *An Atlas of Metal Damage, Surface Examination by Scanning Electron Microscope*. Wolfe Science, Munich, 1981.
- [52] A. L. Eterovic and K.-J. Bathe. A hyperelastic-based large strain elasto-plastic constitutive formulation with combined isotropic-kinematic hardening using the logarithmic stress and strain measures. *International Journal for Numerical Methods in Engineering*, 30:1099–1114, 1990.
- [53] M. Fourmeau, T. Børvik, A. Benallal, and O. Hopperstad. Anisotropic failure modes of high-strength aluminium alloy un-

- der various stress states. *International Journal of Plasticity*, doi: 10.1016/j.ijplas.2013.02.004, 2013.
- [54] X. Gao, T. Zhang, M. Hayden, and C. Roe. Effects of the stress state on plasticity and ductile failure of an aluminum 5083 alloy. *International Journal of Plasticity*, 25:2366–2382, 2009.
- [55] W. M. Garrison and N. R. Moody. Ductile fracture. *Journal of Physics and Chemistry of Solids*, 48:1035–1074, 1987.
- [56] S. Gerke and M. Brünig. Modelling and numerical simulations of rate and temperature-dependent damage and fracture in aluminium alloys. *Proceedings in Applied Mathematics and Mechanics*, 10:113–114, 2010.
- [57] S. Gerke and M. Brünig. Damage and fracture behavior in dynamic tension tests: Modelling and numerical simulations. *Proceedings in Applied Mathematics and Mechanics*, 11:147–148, 2011.
- [58] S. Gerke, M. Brünig, and L. Driemeier. Numerical simulation of damage and fracture in split hopkinson bar tests. In A. S. Kahn and B. Farrokh, editors, *Finite Plasticity and Visco-Plasticity of Conventional and Emerging Materials, 16th International Symposium on Plasticity and its Current Applications*. Neat Inc., Saint Kitts, 2010.
- [59] C. G’Sell, J. M. Hiver, A. Dahoun, and A. Souahi. Video-controlled tensile testing of polymers and metals beyond the necking point. *Journal of Materials Science*, 27:5031–5039, 1992.
- [60] W.-G. Guo and S. Nemat-Nasser. Flow stress of nitronic-50 stainless steel over a wide range of strain rates and temperatures. *Mechanics of Materials*, 38:1090–1103, 2006.
- [61] A. L. Gurson. Continuum theory of ductile rupture by void nucleation and growth: Part I – yield criteria and flow rules for porous ductile media. *Journal of Engineering Materials and Technology*, 99:2–15, 1977.
- [62] J. Hallquist. *LS-Dyna Theory Manual*. Livermore Software Technology Corporation, 2006.
- [63] R. Harsoor and L. Ramachandra. Influence of notch on the elastic-plastic response of clamped beams subjected to low velocity impact. *International Journal of Impact Engineering*, 36:1058–1069, 2009.
- [64] G. Haugou, E. Markiewicz, and J. Fabis. On the use of the non direct tensile loading on a classical split hopkinson bar apparatus dedicated to sheet metal specimen characterisation. *International Journal of Impact Engineering*, 32:778–798, 2006.

- [65] K. Hayakawa, S. Murakami, and Y. Liu. An irreversible thermodynamics theory for elastic-plastic-damage materials. *European Journal of Mechanics A/Solids*, 17:13–32, 1998.
- [66] S. Hecker, M. Stout, K. Staudhammer, and J. Smith. Effects of strain state and strain rate on deformation-induced transformation in 304 stainless steel: Part I. magnetic measurements and mechanical behavior. *Metallurgical and Materials Transactions A*, 13:619–626, 1982.
- [67] J. Henry. On the mode of testing building materials, and an account of the marble used in the extension of the United States capitol. *Proceedings of the American Association for the Advancement of Science*, 9:102–116, 1855.
- [68] S. Hiermaier. *Structures under crash and impact: continuum mechanics, discretization and experimental characterization*. Springer, New York, 2008.
- [69] O. S. Hopperstad, T. Børvik, M. Langseth, K. Labibes, and C. Albertini. On the influence of stress triaxiality and strain rate on the behaviour of structural steel. part I. experiments. *European Journal of Mechanics A/Solids*, 22:1–13, 2003.
- [70] G. Hütter, L. Zybell, U. Mühlich, and M. Kuna. Ductile crack propagation by plastic collapse of the intervold ligaments. *International Journal of Fracture*, 176:81–96, 2012.
- [71] K. Ishikawa and S. Tanimura. Strain rate sensitivity of flow stress at low temperatures in 304n stainless steel. *International Journal of Plasticity*, 8:947–958, 1992.
- [72] G. R. Johnson and W. H. Cook. A constitutive model and data for metals subjected to large strains, high strain rates and high temperatures. In *Proceedings of the Seventh International Symposium on Ballistics, Hague, Netherlands*. American Defense Preparedness Association; Koninklijk Instituut van Ingenieurs (Netherlands), 541–547, 1983.
- [73] G. R. Johnson and W. H. Cook. Fracture characteristics of three metals subjected to various strains, strain rates, temperatures and pressures. *Engineering Fracture Mechanics*, 21:31–48, 1985.
- [74] G. R. Johnson and T. J. Holmquist. Evaluation of cylinder-impact test data for constitutive model constants. *Journal of Applied Physics*, 64:3901–3910, 1988.
- [75] L. M. Kachanov. Rupture time under creep conditions. *Izvestia Akademii Nauk SSSR, Otdelenie Tekhnicheskich Nauk*, 8:26–31, 1958.

- [76] L. M. Kachanov. Continuum model of medium with cracks. *Journal of the Engineering Mechanics Division*, 106:1039–1051, 1980.
- [77] L. M. Kachanov. *Introduction to continuum damage mechanics*. Martinus Nijhoff Publishers, Dordrecht, 1986.
- [78] L. M. Kachanov. Rupture time under creep conditions. *International Journal of Fracture*, 97:11–18, 1999.
- [79] A. Kaiser. Advancements in the Split Hopkinson bar test. Master's thesis, Virginia Polytechnic Institute and State University, 1998.
- [80] J. Kajberg and K.-G. Sundin. Material characterisation using high-temperature Split Hopkinson pressure bar. *Journal of Materials Processing Technology*, 213:522–531, 2013.
- [81] M. A. Kariem, J. H. Beynon, and D. Ruan. Misalignment effect in the Split Hopkinson pressure bar technique. *International Journal of Impact Engineering*, 47:60–70, 2012.
- [82] H. Kolsky. An investigation of the mechanical properties of materials at very high rates of loading. *Proceedings of the Physical Society; Section B*, 62:676–700, 1949.
- [83] H. E. Konokman, M. M. Çoruh, and A. Kayran. Computational and experimental study of high-speed impact of metallic Taylor cylinders. *Acta Mechanica*, 220:61–85, 2011.
- [84] D. Krajcinovic. Constitutive equations for damaging materials. *Journal of Applied Mechanics*, 50:355–360, 1983.
- [85] D. Krajcinovic. Continuum damage mechanics. *Applied Mechanics Reviews*, 37:1–6, 1984.
- [86] D. Krajcinovic. Damage mechanics. *Mechanics of Materials*, 8:117–197, 1989.
- [87] D. Krajcinovic. *Damage Mechanics*. Elsevier, North-Holland series, Amsterdam, 1996.
- [88] D. Krajcinovic and G. Fonseka. The continuous damage theory of brittle materials, part I: General theory. *Journal of Applied Mechanics*, 48:809–815, 1981.
- [89] D. Krajcinovic and G. Fonseka. The continuous damage theory of brittle materials, part II: Uniaxial and plane response modes. *Journal of Applied Mechanics*, 48:816–824, 1981.
- [90] H. Kuhn and D. Medlin, editors. *ASM handbook, Volume 8: Mechanical Testing and Evaluation*. ASM international, Materials Park, OH, 2000.
- [91] C. Landron, E. Maire, O. Bouaziz, J. Adrien, L. Lecarme, and A. Bareggi. Validation of void growth models using X-ray microto-

- mography characterization of damage in dual phase steels. *Acta Materialia*, 59:7564–7573, 2011.
- [92] E. Lee. Elastic-plastic deformation at finite strains. *Journal of Applied Mechanics*, 1:1–6, 1969.
- [93] W.-S. Lee and C.-F. Lin. High-temperature deformation behaviour of ti6al4v alloy evaluated by high strain-rate compression tests. *Journal of Materials Processing Technology*, 75:127–136, 1998.
- [94] T. Lehmann. Some remarks on the decomposition of deformations and mechanical work. *International Journal of Engineering Science*, 20:281–288, 1982.
- [95] T. Lehmann. Some theoretical considerations and experimental results concerning elastic-plastic stress-strain relations. *Ingenieur-Archiv*, 52:391–403, 1982.
- [96] T. Lehmann. Some thermodynamical considerations on inelastic deformations including damage processes. *Acta Mechanica*, 79:1–24, 1989.
- [97] T. Lehmann. Thermodynamical foundations of large inelastic deformations of solid bodies including damage. *International Journal of Plasticity*, 7:79–98, 1991.
- [98] J. Lemaitre. A continuous damage mechanics model for ductile fracture. *Journal of Engineering Materials and Technology*, 107:83–89, 1985.
- [99] J. Lemaitre. Coupled elasto-plasticity and damage constitutive equations. *Computer Methods in Applied Mechanics and Engineering*, 51:31–49, 1985.
- [100] J. Lemaitre. *A Course on Damage Mechanics*. Springer, Berlin, 1996.
- [101] J. Lemaitre and R. Desmorat. *Engineering Damage Mechanics; Ductile, Creep, Fatigue and Brittle Failures*. Springer, Berlin, 2005.
- [102] J. Lemaitre, R. Desmorat, and M. Sauzay. Anisotropic damage law of evolution. *European Journal of Mechanics A/Solids*, 19:187–208, 2000.
- [103] J. Lemaitre and J. Dufailly. Damage measurements. *Engineering Fracture Mechanics*, 28:643–661, 1987.
- [104] A. Lennon and K. Ramesh. A technique for measuring the dynamic behavior of materials at high temperatures. *International Journal of Plasticity*, 14:1279–1292, 1998.
- [105] J. R. Lewis. *Handbook of Stainless Steels*. McGraw-Hill, New York, 1977.

- [106] H. Li, M. Fu, J. Lu, and H. Yang. Ductile fracture: Experiments and computations. *International Journal of Plasticity*, 27:147–180, 2011.
- [107] J. Liu and N. Jones. Experimental investigation of clamped beams struck transversely by a mass. *International Journal of Impact Engineering*, 6:303–335, 1987.
- [108] Livermore Software Technology Corporation (LSTC), Livermore, CA. *Ls-Dyna Keyword User’s Manual; Volume I*, 971 edition, 2007.
- [109] T. J. Lu and C. L. Chow. On constitutive equations of inelastic solids with anisotropic damage. *Theoretical and Applied Fracture Mechanics*, 14:187–218, 1990.
- [110] P. Ludwik. Die Bedeutung des Gleit- und Reißwiderstandes für die Werkstoffprüfung. *Zeitschrift des Vereins deutscher Ingenieure*, 71:1532–1538, 1927.
- [111] M. Luo, M. Dunand, and D. Mohr. Experiments and modeling of anisotropic aluminum extrusions under multi-axial loading - part II: Ductile fracture. *International Journal of Plasticity*, 32-33:36–58, 2012.
- [112] E. Maire, O. Bouaziz, M. D. Michiel, and C. Verdu. Initiation and growth of damage in dual-phase steel observed by X-ray microtomography. *Acta Materialia*, 56:4954–4964, 2008.
- [113] E. Maire, S. Zhou, J. Adrien, and M. Dimichiel. Damage quantification in aluminum alloys using in situ tensile tests in X-ray tomography. *Engineering Fracture Mechanics*, 78:2679–2690, 2011.
- [114] L. Malcher, F. A. Pires, and J. C. de Sá. An assessment of isotropic constitutive models for ductile fracture under high and low stress triaxiality. *International Journal of Plasticity*, 30-31:81–115, 2012.
- [115] F. McClintock. A criterion for ductile fracture by the growth of holes. *Journal of Applied Mechanics*, 35:363–371, 1968.
- [116] M. Mićunović, C. Albertini, and C. Montagnani. High strain rate thermo-inelasticity of damaged AISI 316H. *International Journal of Damage Mechanics*, 12:267–303, 2003.
- [117] D. Mohr and G. Gary. High strain rate tensile testing using a Split Hopkinson pressure bar apparatus. *Journal of Physics IV France*, 134:617–622, 2006.
- [118] D. Mohr and G. Gary. M-shaped specimen for high-strain rate tensile testing using a Split Hopkinson pressure bar apparatus. *Experimental Mechanics*, 47:681–692, 2007.
- [119] D. Mohr and S. Henn. Calibration of stress-triaxiality dependent

- crack formation criteria: A new hybrid experimental–numerical method. *Experimental Mechanics*, 47:805–820, 2007.
- [120] S. Murakami. Anisotropic damage in metals. In Boehler, editor, *Failure Criteria of Structured Media: Proceedings of the CNRS international colloquium No 351*. Villard-de-Lans, 99–119, 1983.
- [121] S. Murakami. Mechanical modeling of material damage. *Journal of Applied Mechanics*, 55:280–286, 1988.
- [122] S. Murakami. *Continuum Damage Mechanics: A Continuum Mechanics Approach to the Analysis of Damage and Fracture*. Springer, Dordrecht, 2012.
- [123] S. Murakami, K. Hayakawa, and Y. Liu. Damage evolution and damage surface of elastic-plastic-damage materials under multiaxial loading. *International Journal of Damage Mechanics*, 7:103–128, 1998.
- [124] S. Murakami and N. Ohno. A continuum theory of creep and creep damage. In A. R. S. Ponter and D. R. Hayhurst, editors, *Creep in Structures*. Springer Verlag, Berlin, 442–443, 1981.
- [125] K. Nahshon and J. Hutchinson. Modification of the Gurson model for shear failure. *European Journal of Mechanics A/Solids*, 27:1–17, 2008.
- [126] A. Needleman. Void growth in an elastic-plastic medium. *Journal of Applied Mechanics*, 4:964–970, 1972.
- [127] S. Nemat-Nasser. Rate-independent finite-deformation elastoplasticity: a new explicit constitutive algorithm. *Mechanics of Materials*, 11:235–249, 1991.
- [128] S. Nemat-Nasser, W.-G. Guo, and D. P. Kihl. Thermomechanical response of AL-6XN stainless steel over a wide range of strain rates and temperatures. *Journal of the Mechanics and Physics of Solids*, 49:1823–1846, 2001.
- [129] S. Nemat-Nasser, J. B. Isaacs, and J. E. Starrett. Hopkinson techniques for dynamic recovery experiments. *Proceedings of the Royal Society of London - Series A*, 435:371–391, 1991.
- [130] M. Niazi, H. Wisselink, T. Meinders, and J. Huétink. Failure predictions for DP steel cross-die test using anisotropic damage. *International Journal of Damage Mechanics*, 21:713–754, 2012.
- [131] M. Nurse. *Stainless Steel, an International Survey and Directory*. Metal Bulletin, Worcester Park, 1982.
- [132] W. S. Park, M. S. Chun, M. S. Han, M. H. Kim, and J. M. Lee. Comparative study on mechanical behavior of low temperature ap-

- plication materials for ships and offshore structures: Part I – experimental investigations. *Materials Science and Engineering: A*, 528:5790–5803, 2011.
- [133] W. S. Park, S. W. Yoo, M. H. Kim, and J. M. Lee. Strain-rate effects on the mechanical behavior of the aisi 300 series of austenitic stainless steel under cryogenic environments. *Materials & Design*, 31:3630–3640, 2010.
- [134] D. Perić, D. Owen, and M. Honnor. A model for finite strain elasto-plasticity based on logarithmic strains: Computational issues. *Computer Methods in Applied Mechanics and Engineering*, 94:35–61, 1992.
- [135] M. Peroni. *Experimental Methods for Material Characterization at High Strain-Rate: Analytical and Numerical Improvements*. PhD thesis, Politecnico di Torino, Italy, 2011.
- [136] Y. N. Rabotnov. On the equation of state for creep. *Progress in Applied Mechanics*, The Prager Anniversary Volume:307–315, 1963.
- [137] S. Ricci. *Nichtlokale Modellierung des Versagens- und Schädigungsverhaltens von elastisch-plastischen Materialien*. PhD thesis, Universität Dortmund, 2004.
- [138] J. R. Rice and D. M. Tracey. On the ductile enlargement of voids in triaxial stress fields. *Journal of the Mechanics and the Physics of Solids*, 17:201–217, 1969.
- [139] F. Rivalin, A. Pineau, M. DiÂ Fant, and J. Besson. Ductile tearing of pipeline-steel wide plates: I. dynamic and quasi-static experiments. *Engineering Fracture Mechanics*, 68:329–345, 2000.
- [140] P. Rosakis, A. J. Rosakis, G. Ravichandran, and J. Hodowany. A thermodynamic internal variable model for the partition of plastic work into heat and stored energy in metals. *Journal of the Mechanics and Physics of Solids*, 48:581–607, 2000.
- [141] K. Saanouni. *Damage Mechanics in Metal Forming*. Wiley, London, 2012.
- [142] S. Semiatin and J. Holbrook. Failure behavior of 304l stainless steel in torsion. *Metallurgical and Materials Transactions A*, 14:2091–2099, 1983.
- [143] S. Semiatin and J. Holbrook. Plastic flow phenomenology of 304l stainless steel. *Metallurgical and Materials Transactions A*, 14:1681–1695, 1983.
- [144] J. Simo and J. Ju. Strain- and stress-based continuum damage models – I. formulation. *International Journal of Solids and Structures*, 23:821–840, 1987.

- [145] J. Simo and J. Ju. Strain- and stress-based continuum damage models – II. computational aspects. *International Journal of Solids and Structures*, 23:841–869, 1987.
- [146] K. N. Singh, R. Clos, U. Schreppel, P. Veit, A. Hamann, D. Klingbeil, R. Sievert, and G. Künecke. Versagenssimulation dynamisch belasteter Proben mit unterschiedlichen Mehrachsigekeitszuständen unter Verwendung des Johnson-Cook-Versagensmodells für eine Nickelbasislegierung. *Technische Mechanik*, 23:205–215, 2003.
- [147] W. A. Spitzig and O. Richmond. The effect of pressure on the flow stress of metals. *Acta Metallurgica*, 32:457–463, 1984.
- [148] W. A. Spitzig, R. J. Smelser, and O. Richmond. The evolution of damage and fracture in iron compacts with various initial porosities. *Acta Metallurgica*, 36:1201–1211, 1988.
- [149] W. A. Spitzig, R. J. Sober, and O. Richmond. Pressure dependence of yielding and associated volume expansion in tempered martensite. *Acta Materialia*, 23:885–893, 1975.
- [150] W. A. Spitzig, R. J. Sober, and O. Richmond. The effect of hydrostatic pressure on the deformation behavior of maraging and HY-80 steels and its implications for plasticity theory. *Metallurgical Transactions A*, 7A:1703–1710, 1976.
- [151] E. Stein and F.-J. Barthold. Grundwissen: Werkstoffe, elastizitätstheorie. In G. Mehlhorn, editor, *Der Ingenieurbau*. Ernst & Sohn, Berlin, 1996.
- [152] P. Steinmann and I. Carol. A framework for geometrically nonlinear continuum damage mechanics. *International Journal of Engineering Science*, 36:1793–1814, 1998.
- [153] M. G. Stout and P. S. Follansbee. Strain rate sensitivity, strain hardening, and yield behavior of 304L stainless steel. *Journal of Engineering Materials and Technology*, 108:344–353, 1986.
- [154] W. H. Tai and B. X. Yang. A new microvoid-damage model for ductile fracture. *Engineering Fracture Mechanics*, 25:377–384, 1986.
- [155] G. Taylor. The use of flat-ended projectiles for determining dynamic yield stress. I: Theoretical considerations. *Proceedings of the Royal Society of London - Series A*, 194:289–299, 1948.
- [156] H. Toda, E. Maire, S. Yamauchi, H. Tsuruta, T. Hiramatsu, and M. Kobayashi. In situ observation of ductile fracture using X-ray tomography technique. *Acta Materialia*, 59:1995–2008, 2011.
- [157] H. Toda, I. Sinclair, J.-Y. Buffière, E. Maire, K. Khor, P. Gregson, and T. Kobayashi. A 3D measurement procedure for internal local

- crack driving forces via synchrotron X-ray microtomography. *Acta Materialia*, 52:1305–1317, 2004.
- [158] V. Tvergaard. Material failure by void coalescence in localized shear bands. *International Journal of Solids and Structures*, 18:659–672, 1982.
- [159] V. Tvergaard. Material failure by void growth to coalescence. *Advances in Applied Mechanics*, 27:83–151, 1990.
- [160] V. Tvergaard. Effect of stress-state and spacing on voids in a shear-field. *International Journal of Solids and Structures*, 49:3047–3054, 2012.
- [161] V. Tvergaard and A. Needleman. Analysis of the cup-cone fracture in a round tensile bar. *Acta Materialia*, 32,1:157–169, 1984.
- [162] R. Vignjevic, N. Djordjevic, J. Campbell, and V. Panov. Modelling of dynamic damage and failure in aluminium alloys. *International Journal of Impact Engineering*, 49:61–76, 2012.
- [163] R. Vignjevic, N. Djordjevic, and V. Panov. Modelling of dynamic behaviour of orthotropic metals including damage and failure. *International Journal of Plasticity*, 38:47–85, 2012.
- [164] G. Z. Voyiadjis and P. I. Kattan. A plasticity-damage theory for large deformation of solids - i. theoretical formulation. *International Journal of Engineering Science*, 9:1089–1108, 1992.
- [165] G. Z. Voyiadjis and T. Park. The kinematics of damage for finite-strain elasto-plastic solids. *International Journal of Engineering Science*, 37:803–830, 1999.
- [166] G. Weber and L. Anand. Finite deformation constitutive equations and a time integration procedure for isotropic, hyperelastic-viscoplastic solids. *Computer Methods in Applied Mechanics and Engineering*, 79:173–202, 1990.
- [167] C. Wegst and M. Wegst. *Nachschlagewerk Stahlschlüssel*. Verlag Stahlschlüssel Wegst GmbH, Marbach, 2004.
- [168] K. Weimar. *Ls-Dyna Introductory Course Nodes*. DYNAmore GmbH, Stuttgart, 2006.
- [169] P. Wriggers. *Nichtlineare Finite-Element-Methoden*. Springer, Berlin, 2001.
- [170] L. Xue. Constitutive modeling of void shearing effect in ductile fracture of porous materials. *Engineering Fracture Mechanics*, 75:3343–3366, 2008.
- [171] W. Zhang and Y. Cai. *Continuum Damage Mechanics and Numerical Applications*. Zhejiang university press and Springer, Hangzhou, 2010.

-
- [172] Y. Zhou and Y. Xia. Experimental study of the rate-sensitivity of SiC_p/Al composites and the establishment of a dynamic constitutive equation. *Composites Science and Technology*, 60:403–410, 2000.